

---

Theses and Dissertations

---

Fall 2013

# Modeling of the human larynx with application to the influence of false vocal folds on the glottal flow

Mehrdad Hosnieh Farahani  
*University of Iowa*

Copyright 2013 Mehrdad Hosnieh Farahani

This dissertation is available at Iowa Research Online: <http://ir.uiowa.edu/etd/4992>

---

## Recommended Citation

Hosnieh Farahani, Mehrdad. "Modeling of the human larynx with application to the influence of false vocal folds on the glottal flow." PhD (Doctor of Philosophy) thesis, University of Iowa, 2013. <http://ir.uiowa.edu/etd/4992>.

---

Follow this and additional works at: <http://ir.uiowa.edu/etd>



Part of the [Biomedical Engineering and Bioengineering Commons](#)

MODELING OF THE HUMAN LARYNX WITH APPLICATION TO THE  
INFLUENCE OF FALSE VOCAL FOLDS ON THE GLOTTAL FLOW

by

Mehrdad Hosnieh Farahani

A thesis submitted in partial fulfillment  
of the requirements for the Doctor of  
Philosophy degree in Biomedical Engineering  
in the Graduate College of  
The University of Iowa

December 2013

Thesis Supervisor: Assistant Professor Sarah Vigmostad

Graduate College  
The University of Iowa  
Iowa City, Iowa

CERTIFICATE OF APPROVAL

---

PH.D. THESIS

---

This is to certify that the Ph.D. thesis of

Mehrdad Hosnieh Farahani

has been approved by the Examining Committee  
for the thesis requirement for the Doctor of Philosophy  
degree in Biomedical Engineering at the December 2013 graduation.

Thesis Committee: \_\_\_\_\_  
Sarah Vigmostad, Thesis Supervisor

\_\_\_\_\_  
Joseph M. Reinhardt

\_\_\_\_\_  
Fariborz Alipour

\_\_\_\_\_  
Madhavan L. Raghavan

\_\_\_\_\_  
James H.J. Buchholz

To my parents

## ACKNOWLEDGMENTS

I would like to thank my adviser Dr. Sarah Vigmostad for introducing me to this interesting research project. I am also grateful for her guidance and support. In addition, I am thankful to my committee members for their suggestions. Especially, I am sincerely thankful of Dr. Fariborz Alipour for his kind suggestions and advice in the course of this journey. He generously allowed me to use his laboratory for the experimental investigations. I would also like to express my gratitude to Dr. Udaykumar for his suggestions and advice for the computational part of my dissertation. My greatest appreciation goes to my colleague John Mousel for his friendship, patience, support, valuable comments, and constructive suggestions. Sitting next to me in our lab with his immense computational knowledge, he was always willing to help. I am thankful to Seth Dillard for image segmentation of medical images. I would also like to acknowledge my other colleagues Ehsan, Liza, Keshav, Anil, Nirmal, Oishik and Piyusha for providing a friendly and fun atmosphere. Last but not least, I am grateful of my family for their continued love and support.

## ABSTRACT

Human phonation is a complex phenomenon produced by multiphysics interaction of the fluid, tissue and acoustics fields. Despite recent advancement, little is known about the effect of false vocal folds on the fluid dynamics of the glottal flow. Recent investigations have hypothesized that this pair of tissue can affect the laryngeal flow during phonation. This hypothesis is tested both computationally and experimentally in this dissertation. The computations were performed using an incompressible solver developed on fixed Cartesian grid with a second order sharp immersed-boundary formulation while the experiments were carried out in a low-speed wind tunnel with physiologic speeds and dimensions. A parametric study was performed to understand the effect of false vocal folds geometry on the glottal flow dynamics and the flow structures in the laryngeal ventricle. The investigation focused on three geometric features: the size of the false vocal fold gap, the height between the true and false vocal folds, and the width of the laryngeal ventricle. It was found that the size of the false vocal fold gap has a significant effect on glottal flow aerodynamics; whereas the height between the true and false vocal folds and the width of the laryngeal ventricle were of lesser importance.

A framework was introduced to extract the laryngeal geometry from the CT scan images. The image segmentation technique was utilized to extract the laryngeal geometries of a canine and a 45 years old female human larynx. Fully resolved three dimensional simulations of the laryngeal flow were conducted for physiological Reynolds numbers in these realistic geometries to gain insight into the evolution of vortical structures in the larynx. It was shown that the glottal jet flow is highly three dimensional.

The two and three dimensional computational investigations revealed the presence of the rarely reported secondary vortices in the laryngeal ventricle known as rebound vortical structures. It was found that these vortical structures are formed due to the interaction between the starting vortex ring and the false vocal folds. Therefore, the

small size of the false vocal folds gap was identified as an important factor in increasing the intensity of these vortical structures.

Finally, a novel high order Cartesian based moving least square finite volume solver was developed in this dissertation to model acoustic wave scattering at low Mach numbers flows. The computational aeroacoustic approach is based on incompressible viscous/acoustic splitting technique. In this solver, linearized perturbed compressible equations are solved on Cartesian grids and the boundaries are treated sharply using ghost fluid approach. The Cartesian grid framework is compatible with the incompressible solver and provides the flexibility of handling complex geometries. The acoustic solver was validated against several benchmark problems for which analytical solution is available.

## TABLE OF CONTENTS

LIST OF TABLES .....	viii
LIST OF FIGURES .....	ix
CHAPTER 1 INTRODUCTION .....	1
1.1 Motivation.....	1
1.2 Physiology of the Larynx.....	3
1.3 Literature Review .....	4
1.3.1 Experimental Investigations on Flow Structures of the Glottal Flow .....	4
1.3.2 The Effects of the FVFs on Laryngeal Flow .....	6
1.3.3 Three Dimensional Computational Simulations of the Larynx.....	8
1.4 Objectives .....	10
CHAPTER 2 EXPERIMENTAL APPARATUS .....	14
2.1 Introduction.....	14
2.2 Experimental Models.....	14
2.3 Experimental Apparatus and Data Collection .....	16
CHAPTER 3 INCOMPRESSIBLE SOLVER.....	23
3.1 Introduction.....	23
3.2 Governing Equations .....	23
3.3 Fractional Step Algorithm .....	24
3.4 Interface Treatment.....	25
3.5 Level Set Fields .....	28
3.6 Adaptive Local Mesh Refinement.....	29
3.7 Two-Mass Model of the Vocal Folds .....	29
3.8 Validation of the Incompressible Flow Solver for a Laryngeal Geometry .....	31
CHAPTER 4 ACOUSTIC SOLVER.....	37
4.1 Introduction.....	37
4.2 Governing Equations and Computational Approach.....	38
4.3 Moving Least Square Method .....	40
4.4 Finite Volume Formulation .....	43
4.4.1 General Finite Volume Formulation of LPCE .....	43
4.4.2. Standard Flux Vector Splitting Technique .....	45
4.5 Time Integration .....	48
4.6 Boundary Condition Treatment.....	48
4.6.1 Non-Reflective (Absorbing) Boundary Conditions.....	48
4.6.2 Perfectly Reflective Boundary Conditions .....	50
4.7 Filtering.....	51
4.8 Validation of the FVMLS Solver .....	53
4.8.1 Propagation of a Gaussian Pressure Pulse.....	53
4.8.2 Radiation of a Pulsatile Monopole in a Uniform Mean Flow .....	54

4.8.3 Propagation of a Wall-Bounded Acoustic Pulse in a Uniform Mean Flow .....	55
4.8.4 Acoustic Wave Propagation from a Circular Cylinder.....	56
CHAPTER 5 THE EFFECT OF FALSE VOCAL FOLDS GEOMETRY ON GLOTTAL FLOW.....	71
5.1 Introduction.....	71
5.2 Classification of the Laryngeal Models.....	71
5.3 Grid Independent Study.....	72
5.4 Comparison with previous investigation of the glottal flow .....	74
5.5 The effect of the FVF gap on the glottal flow aerodynamics .....	76
5.6 The Effect of the Height between TVF and FVF. ....	82
5.7 The Effect of the Width of the Laryngeal Ventricle.....	83
5.8 Oscillation of the Vocal Folds .....	85
5.9 Conclusion .....	86
CHAPTER 6 TOWARD PATIENT SPECIFIC SIMULATION OF THE AIR FLOW IN THE LARYNX .....	102
6.1 Introduction.....	102
6.2 Image Segmentation of the Larynx.....	103
6.3 Fully Resolved Simulation of the Glottal Flow in the Human and Canine Larynges with an Steady Inlet Flow .....	106
6.4 A Fully Resolved Simulation of the Glottal Flow in a Human Larynx with a Pulsatile Inlet Flow.....	108
6.5 Conclusion .....	109
CHAPTER 7 CONCLUSION AND FUTURE WORK.....	124
7.1 Contribution of the Current Thesis .....	124
7.2 Suggestions for Future Work.....	125
References.....	127

## LIST OF TABLES

### Table

2-1	Summary of geometrical parameters used to design the laryngeal models for the experimental study. ....	18
3-1	The value of the parameters of the two-mass model of the vocal folds. ....	33
4-1	Spatial compact filter coefficients for the interior cells. ....	58
4-2	Spatial compact filter coefficients for boundary cells. ....	58
5-1	Summary of geometrical parameters used to design the laryngeal models. ....	88
5-2	Non-dimensional differential pressures collected in the experiments on the surface of the models with different FVF gap. ....	88
5.3	Non-dimensional differential pressures on the surface of the larynx in the computational simulations. ....	88

## LIST OF FIGURES

Figure	
1-1	A cross section of the larynx.....12
1-2	Top view of the larynx during inspiration (left) and adducted posture (right). .....12
1-3	A schematic view of a single cycle of phonation. ....13
2-1	Schematic view of the laryngeal models, $W_{sub}$ = width of subglottal region, $W_{sup}$ = width of supraglottal region, $W_{VL}$ = width of ventricle of the larynx, $H_{fvf}$ = height between FVFs and TVFs, $G_{tvf}$ = TVF gap, $G_{fvf}$ = FVF gap. $G_{tvf} = 1mm$ , and $W_{sub} = W_{sup} = 20 mm$ are constant for all models. The location of the pressure taps on the surface of the experimental models is shown in the lower side of the larynx. ....19
2-2	Schematic view of the CAD design for the bottom side of the C1 model designed by Pro/Engineer software. ....20
2-3	A schematic view of the CAD design for the top side of the C1 model designed by Pro/Engineer software .....21
2-4	A schematic view of the wind tunnel and experimental set up .....22
2-5	A close-up of the experimental model connected to the pressure taps .....22
3-1	A representation of GFM and least square cloud for an arbitrary ghost cell used in the Cartesian Incompressible solver.....34
3-2	Schematic view of one side of the laryngeal model and the two-mass model configuration.....34
3-3	Vorticity contour of the air flow in a semi-laryngeal structure of the current Cartesian solver (left) and the direct numerical simulation of Chisari et al. (right) at (a) 3.5 ms, (b) 5.8 ms, (c) 7.2 ms (d) 7.8 ms, and (e) 9.5 ms. The size of first and second constriction gap was 0.04 and 0.08 cm respectively.....35
3-4	A comparison between the current computational solver (solid lines) with the result of Chisari et al. (scattered symbols). (a) pressure and (b) streamwise velocity profiles along the line that connect the starting vortex centroids at times of 3.73ms (circles), 4.43ms (squares), 4,78ms (diamonds), and 5.83 (deltas). ....36
4-1	A schematic view of the MLS cloud for non-uniform data points. ....59
4-2	A finite-volume Cartesian cell and the cell face fluxes. ....60
4.3	A schematic view of the boundary conditions in an acoustic problem. Non-reflective boundaries absorb and damp the outgoing waves and reflective boundaries reflect the acoustic waves back into the solution domain. ....60

4-4	A representation of GFM and MLS cloud for an arbitrary ghost cell used in the FVMLS acoustic solver on the Cartesian grids. ....	61
4.5	Notation of a one-dimensional spatial filter .....	61
4.6	Contours of non-dimensional perturbed pressure at $t = 25, 50, 75,$ and $100$ . The contours have 10 levels between $-0.1$ and $0.1$ . The sponge layer is located outside of the circle. The black circle shows the beginning of the sponge zone.....	62
4-7	Contours of non-dimensional perturbed velocities at $t = 25,$ and $50$ . The contours have 10 levels between $-0.1$ and $0.1$ .The sponge layer is located outside of the circular zone. The black circle shows the beginning of the sponge zone.....	63
4-8	Comparison between the non-dimensional computational perturbed pressure using the current FVMLS solver and analytical solutions of the Gaussian pressure pulse on the line $y = 100$ at (a) $t = 25$ and (b) $t = 50$ . ....	64
4-9	Contours of the perturbed pressure of a pulsatile monopole at $t = 90, 150, 210,$ and $270$ . The sponge layer is located outside of the circular zone. The black circle shows the beginning of the sponge zone. ....	65
4-10	Comparison between the non-dimensional computational perturbed pressure calculated using the current FVMLS solver and the analytical solutions of the pulsatile monopole ( $M=0.5$ ) on the line $y = 120$ and $t = 270$ . ....	66
4-11	Contours of the non-dimensional perturbed pressure of a wall-bounded Gaussian pressure pulse in a uniform mean flow ( $M=0.5$ ). MLSFV solver right), 6 <sup>th</sup> order finite difference compact method (left) The black circle shows the beginning of the sponge zone. ....	67
4-12	A schematic view of the test case problem: acoustic wave propagation from a circular cylinder. ....	68
4-13	Contours on non-dimensional perturbed pressure at $t = 2, 4, 6,$ and $8$ . The contours have 10 levels between $-0.1$ and $0.1$ . The black circle shows the beginning of the sponge zone. ....	69
4-14	Comparison between the time history of the dimensionless computational perturbed pressure calculated using the current FVMLS solver and the analytical solutions of acoustic wave propagation from a circular cylinder at points a, b, c, and d. ....	70
5-1	Grid refinement study: Comparison between the fine (a) and coarse (b) mesh. The Cartesian mesh interior to the solid that is not required for the ghost fluid treatment is pruned during the simulation for improved memory performance.....	89
5-2	Comparison between the vorticity contours of the coarse and fine grid at $t^* = 0.064, 0.104, 0.128, 0.152, 0.176, 0.208, 0.24, 0.272,$ and $0.304$ respectively. ....	90

5-3	Non-dimensional vorticity contours for the laryngeal models with different size of the $G_{fvf}$ at non-dimensional time ( $t^*$ ) of (a) 0.128, (b) 0.176, (c) 0.24, and (d) 0.304. The interaction between the starting vortex and the FVFs increases as the $G_{fvf}$ decreases; hence, rebound vortices in the laryngeal ventricle of the models with narrow $G_{fvf}$ are stronger .....	91
5.4	Streamline contour of the glottal flow for the G4 laryngeal model at at non-dimensional time ( $t^*$ ) of (a) 0.128, (b) 0.176, (c) 0.24, and (d) 0.3. ....	92
5-5	Non-dimensional differential pressure ( $\Delta P^*$ ) history on the surface of the TVFs (a), laryngeal ventricle (b), and FVFs (c) for models with different size of FVF gap. $t^*$ is the non-dimensional time. The pressure initially drops as the starting vortex is created and convected in the laryngeal ventricle, and then recovers partially for the rest of the simulation. Moreover, pressure data on the surface of the FVF fluctuate for the models with narrow $G_{fvf}$ . ....	93
5-6	Plots of non-dimensional differential pressure ( $\Delta P^*$ ) for (a) G2 model, (b) C1, and (c) G4 laryngeal models. ....	94
5-7	Non-dimensional vorticity contours for the laryngeal models with different size of $H_{fvf}$ at non-dimensional time ( $t^*$ ) of (a) 0.128, and (b) 0.304 respectively. ....	95
5-8	Non-dimensional differential pressure ( $\Delta P^*$ ) history on the surface of (a) TVFs, and (b) laryngeal ventricle, and (c) FVFs for models with different size of $H_{fvf}$ . $t^*$ is the non-dimensional time. ....	96
5-9	Plots of non-dimensional differential pressure ( $\Delta P^*$ ) for (a) H1 model, (b) H2, laryngeal models. ....	97
5-10	Non-dimensional vorticity contours for the laryngeal models with different size of at non-dimensional time ( $t^*$ ) of (a) 0.128, and (b) 0.304. ....	98
5-11	Non-dimensional differential pressure history on the surface of TVFs, laryngeal ventricle, and FVFs for models with different size of $W_{lv}$ . ....	99
5-12	Plots of non-dimensional differential pressure ( $\Delta P^*$ ) for (a) L1 model, (b) L2, laryngeal models. ....	100
5-13	Vorticity contours during the self-sustained oscillation of the vocal fold, (a) $t * T = 0.01$ , (b) $t * T = 0.25$ , (c) $t * T = 0.5$ , (d) $t * T = 0.75$ . $T$ is the time period of the oscillation. The orientation of TVFs surfaces is shown at the bottom of each figure to provide better clarity. ....	101
6-1	The cropped image of the human larynx obtained from CT scan images. ....	110
6-2	A top view of the interpolated boundaries after thresholding the voxels. The figure shows an outer boundary, the larynx at the middle, another boundary from some extra tissue on the right of the larynx, and some small closed boundaries. ....	111

6-3	Illustration of object-labeling scheme. Initially a null tag is assigned to all the voxels. The scanning process start in the natural numbering order of the voxels until the first voxel in the object 1 is found (a). All the neighbors of the tagged voxels that are in the object are tagged (b). The scanning resumes till a voxel in the second object is found (c). The all the neighbors in the object 2 are tagged. This process is continued until all the voxels in the objects are assigned are tagged (d). .....	112
6-4	The segmented image after object numbering. Three identified are labeled with numbers 1, 2, and 3.....	113
6-5	The source level set field planes are located on the top and bottom of the segmented image (solid blue box) and their target fields are positioned above the top and below the bottom slices, respectively (a). The morphing process is shown in a close-up figure on the left (b). .....	114
6-6	The final geometry of the (a) human larynx, (b) canine larynx.....	115
6-7	The x-vorticity contour of the glottal flow in a canine larynx geometry on a lateral slice (Re=500).....	116
6-8	The glottal flow in a canine larynx geometry indicated with iso-surface of $\lambda$ -2 colored by vorticity magnitude (Re=500). The contours have 20 levels between 0.0 and 150. ....	117
6-9	The y-vorticity contour of the glottal flow in a human larynx geometry on a lateral slice (Re=500).....	118
6-10	The glottal flow in a human larynx geometry indicated with iso-surface of $\lambda$ -2 colored by vorticity magnitude (Re=500). The contours have 20 levels between 0.0 and 100. ....	119
6-11	The x-vorticity contour of the glottal flow for a human larynx geometry on a lateral slice after 9 pulses of the input velocity. The pick Reynolds number is 1000 and T is the time period of each cycle of the pulse.....	120
6-12	The y-vorticity contour of the glottal flow for a human larynx geometry on a lateral slice after 9 pulses of the input velocity. The pick Reynolds number is 1000 and T is the time period of each cycle of the pulse.....	121
6-13	The z-vorticity contour of the glottal flow for a human larynx geometry on a lateral slice after 9 pulses of the input velocity. The pick Reynolds number is 1000 and T is the time period of each cycle of the pulse.....	122
6-14	The glottal flow in a human larynx geometry indicated with iso-surface of $\lambda$ -2 colored by non-dimensional pressure (Re=1000).....	123

## CHAPTER 1

### INTRODUCTION

#### 1.1 Motivation

Communication is the mechanism of expressing ideas and conveying information. It can be subcategorized into nonverbal, verbal (spoken), and written communication. The primary mode of communication is spoken communication or speech [1]. It is the ability to exchange information through sound production in the form of vowels and consonants. Sound generation in the larynx is a complex flow-tissue-acoustic interaction by rapid oscillation of the vocal folds. This complex mechanism can be impaired by vocal abuse (e.g. smoking), overuse (e.g. excessive use of voice at work), misuse, disease, and aging, etc. and lead to abnormal phonation. According to the National Institute on Deafness and Other Communication Disorders (NIDCD) about 7.5 million people in the United State suffer from voice disorders [2]. The incidence of voice disorders for school-age children range from 6% to 24% [3]. The statistics for adults strongly depend on age, gender, and occupation [3]. Pathological phonation can lead to many other emotional, social, educational, economic and occupational concerns. For instance, the annual cost of treatment and absence from work among US teachers was approximately \$2.5 billion in 2001 [4]. A more recent study shows that more than 50% of teachers have dealt with voice disorders at a period of their occupation and the prevalence of voice disorders is significantly higher among female teachers [5]. Large incidence of voice disorders has also been reported for other occupational groups including salespersons, singers, telemarketers, and, lawyers.

Despite the continued effort to understand the physical mechanism of voiced speech, our current knowledge about the process of phonation is still lacking. The main challenge is the inherent non-linearity of the phenomenon and the complicated coupling of multi-physics. Therefore, the overarching goal of the current dissertation is to provide

a better understanding about human speech. Most notably, due to higher incidence of the false vocal folds (FVFs) activities in the pathological phonation [6], a major focus of the current research study is to identify the role of the false vocal folds (FVF) on the aerodynamics of the larynx.

Experimental investigations have shown that glottal flow is inherently three dimensional. Recently, literatures have been published that attempted to computationally capture the three dimensional flow structures of the laryngeal flow. However, these studies have been conducted in idealized geometries of the larynx. This issue has also been highlighted in a very recent review on the fluid dynamics of speech as a shortcoming of the available computational simulations [1]. Hence one of the goals of the current study is to simulate laryngeal flow in realistic three-dimensional geometry of the human larynx extracted from CT scan images.

The current three dimensional computational simulations of laryngeal flow in literature are under-resolved or their Reynolds number is higher or lower than the normal physiological range. A fully-resolved simulation provides an in-depth insight into the fluid dynamics of the glottal flow and leads to a better understanding about the vortical structures near the glottis. This aim can be fulfilled by performing a direct numerical simulation (DNS). However, the requirements of conducting a DNS including massive computational resources and efficient parallel solvers have been major deterrents. This dissertation aims to conduct the first fully-resolved simulation of glottal flow for physiological Reynolds number and geometry of the human larynx.

Acoustics are the final product of the larynx. It is known that the monopole, dipole and quadruple sources of sound with different levels of contribution are created during the voiced speech. Acoustic wave propagation in the larynx is traditionally modeled using acoustic analogies. These methods are established based on a series of assumptions to capture these known acoustic sources. Therefore, it is desirable to develop an acoustic solver which is capable of capturing all the existing acoustic sources with

minimum assumptions. In addition, this solver must be able to perform high order simulations in complex biological geometries. This motivated us to develop a high order finite volume acoustic solver that is capable of directly capturing all the existing acoustic sources in a low Mach number flow regime. The complex geometries are represented using level-set fields in Cartesian grids.

### 1.2 Physiology of the Larynx

The upper airway consists of the oral cavity and the pharynx. The pharynx is branched into esophagus, which connects the mouth to the gastrointestinal tract, and the larynx (or voice box) where the sound is produced. The larynx also plays a protective role for the respiratory system.

Anatomically, the larynx is composed of the laryngeal cartilage, joints, muscles, nerves and blood vessels. This structure includes a pair of tissues known as (true) vocal folds (TVFs). The gap between the vocal folds is called the glottis. Other structures that lie above the TVFs are generally called supraglottic laryngeal structures and mainly consist of the arytenoids, thyroid, epiglottis, and the FVFs (or ventricular folds) (Figure 1-1).

The FVFs are located above the glottis and the sinuous space between the TVFs and FVFs is called the laryngeal ventricle. The TVFs and FVFs are both composed of three layers namely: epithelium, lamina propria and muscle tissue [7]. The TVFs are attached to a pair of pyramidal cartilages known as arytenoids. The thyroid is the largest cartilage of the larynx. The epiglottis is a soft piece of cartilage attached to the thyroid. This cartilage folds down during swallowing and blocks the laryngeal iterance [7].

The TVFs are separated during the inhalation and expiration and the air flow can easily move through the glottis (Figure 1-2). This pair of tissue is adducted and produces a closure at the beginning of phonation (Figure 1-2). The lung pressure at the subglottal region is increased until it overcomes the viscoelastic force of the TVF tissues and opens

the glottis. This minimum lung pressure is the “phonation threshold pressure” [8]. The glottis at the opening phase has a convergent shape (Figure 1-3(c)). A glottal jet flow with a high velocity is created in the intraglottal and supraglottal regions (Figure 1-3(c)) while the air pressure drops simultaneously at these regions. In order to hold the balance between the low air pressure at the intraglottal region and the restoring viscoelastic force of the deformed tissue the configuration of the glottis changes during the cycle of phonation from convergent to parallel, and subsequently to divergent. Finally the glottal gap is closed (Figure 1-3(e)). This cycle, which occurs due to fluid-tissue-acoustic interaction in a fraction of a second, is repeated and produces an oscillatory pattern which is often known as the “self-sustained oscillation” of the vocal folds [9].

The glottal jet and acoustic waves are modified by supraglottal structures, and nasal pharynx, and also in the oral cavity by tongue, lips and jaw position to produce different vowels and consonants [6].

### 1.3 Literature Review

#### 1.3.1 Experimental Investigations on Flow Structures of the Glottal Flow

The glottal flow is a complex unsteady and highly three-dimensional jet flow [1, 10-15]. The coherent structures of the glottal flow were studied in detail by Neubauer et al. [11] using a silicon model of the TVFs and a digital particle image velocimetry (DPIV). This jet flow was initially laminar in their experiments but transitioned to turbulence downstream of the glottal exit. In the region that glottal flow was transitioning to turbulence large scale vortices were formed due to the growth of Kelvin-Helmholtz instabilities in the shear layer around the laminar core of the jet flow. Staggered movement of these vortical structures gave rise to the flapping of the glottal jet flow. Besides, they reported axis switching of the laminar core of the glottal jet during each

cycle of phonation. They discussed that these phenomena is affected by the downstream disturbances. Additionally, they show that the flow separation location moves with time.

Drechsel et al. [16] studied the effect of supraglottic structures using a silicone model of the vocal folds and PIV measurement. They also reported the formation of the starting vortex, presence of axis switching of the jet flow, and slight glottal jet skewing. The latter occurred especially for the setup with unconfined downstream. Since the shutter speed of their PIV setup was not enough, they were not able to capture Kelvin-Helmholtz instabilities on the shear layer of the glottal jet.

Similarly, Erath et al. [12] observed the axis switching of the glottal flow in their experiments using a scaled up mechanically-driven divergent rigid TVFs using PIV measurements. They reported that the vortex shedding from the trailing edge of the jet flow after the flow separation give rise to the shear layer instability; a mechanism that can serve to create large oscillation of the glottal jet flow. In addition, they measured the translaryngeal pressure to investigate their previous hypotheses about possible effect of glottal jet deflection on unsteady force exerted by the TVF oscillation on the air flow (dipole source of sound) [17]. They found that the effect of jet deflection on translaryngeal pressure was minimal and thus their contribution on acoustic output of the larynx was insignificant. The axis switching and shear layer stabilities were also reported in the experimental investigation of Triep et al. [13]. However, asymmetric jet skewing was not considerable in their experiments. Krebs et al. [14] show that the location of axis switching differed at the downstream of the glottis.

Formation of the starting vortex has also been reported in the experiments of Chisari et al. [18]. They also reported formation of secondary vortex structures in the laryngeal ventricles (rebound vortices form the surface of the FVFs). Schwarze et al. [15] show that the starting vortex is a three dimensional flow structure in the form of a vortex ring. Formation of vortex ring has also been investigated for other physiological phenomena [19].

### 1.3.2 The Effects of the FVFs on Laryngeal Flow

False vocal fold (FVF) activities exist in both normal and pathological phonations [6], yet, a complete understanding about the role FVFs even in normal phonation is lacking. A better understanding of the effect of this pair of tissues on the glottal flow will yield insight into human phonation and can aid speech pathologists with better assessment of normal and abnormal phonation which results in improved diagnosis and treatment for speech disorders.

The geometry, positioning, and viscoelastic properties of the FVFs are gender-dependent [20] where the stiffness of the FVF tissue for males is reported to be approximately twice that of female FVF tissue [21]. Moreover, the TVFs are stiffer than the FVFs, and have a smaller viscosity [22]. Therefore, the FVFs barely vibrate in normal phonation, although their vibration is employed in specific singing styles [23-25] and could also be involved in pathological phonation such as ventricular dysphonia [26-28]. Moreover, this pair of tissues is a part of the articulation during the pronunciation of /i/, glottal stops [29], and their adduction is employed to produce specific tones in the Northern Vietnamese language [30]. Clinical observations also indicate that the vibration of the supraglottic structures can be utilized as a compensatory mechanism to provide the source of sound in patients with glottal incompetence [6, 31, 32]. Vibration of the medial edge of the FVFs is hypothesized to provide better voice quality in children who suffer from voice disorders after airway reconstruction [31], although current knowledge in these regards is poor and further investigation is required.

Particle image velocimetry (PIV) measurements of the glottal flow using flexible and static models of TVFs demonstrate that the FVFs could affect the glottal jet [1, 18, 33]. Furthermore, the widely accepted understanding of the FVFs is that the normal positioning of the FVFs in the larynx reduces the transglottal resistance compared to the larynxes without this pair of tissue. This functionality is due to the fact that this pair of tissues could straighten or stabilize the glottal jet flow, and consequently delay the

transition of the laminar glottal jet flow to turbulence [1, 33-36]. However, available computational and experimental results about the role of the FVFs in the phonation have been mostly obtained using normal size and positioning of this pair of tissues. Hence, investigations about the influence of the shape and the size of the FVFs are limited. Kucinschi et al. [37] considered two sizes for the FVF gap ( $G_{\text{fvf}}$ ) and the height between the TVFs and FVFs ( $H_{\text{fvf}}$ ). They reported that the glottal jet for a narrow  $G_{\text{fvf}}$  was straighter and its Strouhal number was lower in comparison with the model with wide  $G_{\text{fvf}}$ . Moreover, the Strouhal number was independent of  $H_{\text{fvf}}$  for wide size of  $G_{\text{fvf}}$ , and its value dropped slightly as the size of  $H_{\text{fvf}}$  was decreased. Alipour et al. [38] showed that the medial compression of the FVFs of excised canine larynges resulted in higher differential glottal resistance. They also provided evidence that the absence of supraglottic structures could significantly affect the vibratory pattern of the TVFs and in extreme conditions result in unstable oscillation of the vocal folds. In a more recent study on canine larynges [39] it was found that the FVFs can vibrate in-phase or out-of-phase with the TVFs and the pressure in the laryngeal ventricle is considerably affected by the motion of the FVFs rather than the TVFs. Li et al. [35] used static models of the larynx to study the effect of  $G_{\text{fvf}}$  on the surface of the larynx with a divergent, parallel, and convergent glottis with a minimum TVF gap ( $G_{\text{tvf}}$ ) of  $0.06\text{cm}$  in a wind tunnel. The smallest flow resistance was found for the models for which the ratio of the  $G_{\text{fvf}}$  to  $G_{\text{tvf}}$  was 1.5-2. All these studies are limited to experimental investigations with focus on influence of  $G_{\text{fvf}}$  and/or  $H_{\text{fvf}}$  and the possible influences of the width of the laryngeal ventricle ( $W_{\text{lv}}$ ) on phonation remain uninvestigated.

The glottal flow past the laryngeal ventricle can be perceived as a type of open cavity flow, where the jet flow can be strong enough to bridge the distance between the TVFs and FVFs. It is known that impingement of the jet flow spanning over an open cavity with its trailing edge creates an acoustic source. If the flow persists for a sufficient time interval, the acoustic waves from this source can propagate and intensify the shear

layer instabilities in the leading edge of the cavity. The growth of these instabilities forms vortical structures in the shear layer of the jet flow and the impingement of these flow structures creates additional sources of sound [40]. Computational studies of Zhang et al. [41] showed that the reattachment of the glottal jet flow with the FVFs created dipole acoustic sources. Medial compression of the FVFs in excised larynx experiments of Alipour et al. [38] increased the sound intensity. Nevertheless, the theoretical investigation of McGowan et al. [42] suggested the presence of the FVFs had a small impact on acoustic output of the larynx. Available literature on flow structures in open cavities have been thoroughly studied at high Reynolds number, turbulent, and compressible cavity flows, but few studies exist for moderate Reynolds number incompressible cavity flows [43]. These studies have focused primarily on rectangular geometries of different aspect ratios, though a recent experimental study showed that the shape of the cavity can considerably affect the flow structures in an open cavity [44].

### 1.3.3 Three Dimensional Computational Simulations of the Larynx

The vast majority of computational simulations of air flow in the larynx have been performed using idealized two-dimensional laryngeal models [1]. However, experimental investigations have highlighted that glottal flow is highly three-dimensional in actuality (Section 1.3.1) [11, 13, 45].

Recent advances in computational techniques and resources have provided the ability to conduct fully three-dimensional simulations of the human larynx. In an early attempt in 2003, Rosa et al. [46] used a finite element solver to simulate the air flow and vocal fold tissue deformation in a three-dimensional tubular laryngeal geometry. Their geometry was created from a series of smoothly connected hyper-ellipses. Despite their success in capturing self-sustained oscillation of the vocal folds, the resolution of their simulation was extremely poor and the flow field was under-resolved. In 2007, Suh et al.

[47] solved the compressible Navier-Stokes equations to model glottal flow using a high order compact finite-difference scheme. Far field acoustic wave propagation and turbulence were modeled in their study using an acoustic analogy and a LES turbulence model, respectively. Their laryngeal geometries were designed using two simplified slit-like divergent and convergent representations of the glottis in a planar channel without FVFs. Their results provided evidence for the existence of complex turbulent flow structures, and possibility of glottal flow deflection (Coanda effect).

In 2010 and 2011, Zheng et al. [48, 49] conducted a series of three-dimensional laryngeal flow simulations using a sharp-interface IBM incompressible solver. TVF oscillation was modeled in their work using a partitioned fluid-structure-interaction coupling strategy. Their laryngeal geometry was extracted from a two-dimensional slice of a human larynx CT scan. After some simplifications the two-dimensional geometry was extended in the third dimension to create a planar channel. The flow structures were modeled in their simulations using DNS with approximately 2,000,000 grid points on a non-uniform Cartesian grid without adaptive refinement. They successfully modeled the self-sustained oscillation of the vocal folds. However, the Reynolds number of their simulations was one-fifth of the physiologic Reynolds number in the larynx ( $Re \cong 210$ ) to reduce the computational cost associated with conducting a high resolution DNS simulation.

Schwarze et al [15] in 2011 used the Open FOAM package to simulate laryngeal flow in a simplified static model of the larynx with a lens-like elliptic glottis in a channel. The Reynolds number of their simulations had a maximum pick value of 8800, which is at the upper limit of the physiological range. Owing to this high Reynolds number, they were able to exploit an implicit LES turbulent model for their flow simulations. They conducted the simulations using 5,000,000, 3,000,000, and 1,000,000 grid cells. Additionally, they validated their results against PIV visualizations of the experiments with the same geometry. Their results revealed creation of complex flow structures,

including a starting vortex ring and a trailing jet. They concluded that there is a strong interaction between the large vortical structures at the trailing jet and the starting vortex ring. In a subsequent study [50], they investigate the differences between two-dimensional and three-dimensional simulations in presence of forced oscillation of the TVFs. The three-dimensional simulations were performed in two geometries that were both extensions of two-dimensional geometries in the third dimension, but with different glottis shapes (slit-like and lens-like). The result revealed a dependency between the vortex dynamics and axis-switching of the jet flow.

In another attempt at three-dimensional simulation of the larynx, Švancara et al. [51] in 2012 extracted several coarse two-dimensional geometries of the vocal tract from MRI images representing Czech vowels. They extended the geometries in the third dimension and created a rectangular duct. Acoustic, fluid and tissue deformation was modeled using finite element models established in ANSYS 13.0. Although they were able to model the full coupling phenomenon, their computational elements were very coarse for providing promising glottal flow simulations.

Very recently, Šidlof et al. [52] performed a three-dimensional simulation of glottal flow using the Open FOAM package. The rigid TVFs in their simulations were designed based on the M5 model of the vocal folds with two angles of  $\pm 20^\circ$  in a rectangular duct. Forced oscillation of the TVFs was modeled based on a prescribed pattern. Their results with 2,100,000 finite volume cells and a RANS turbulent model suggested a complex three-dimensional flow far downstream of the glottis; however, they were not able to resolve flow structures near the glottis.

#### 1.4 Objectives

This work consists of both experimental and computational modeling of the larynx. The experiments would provide a framework to identify some basic, yet controversial topics about the role of this pair of tissue. They are also used to validate the

computational technique. The computational simulations would yield insight into aerodynamics of the larynx. This research will address the following objectives:

1. A parametric study will be conducted using rigid laryngeal models to better understand the effect of the FVFs shape and geometry on the glottal flow and pressure distribution on the surface of the larynx.
2. The flow solver will be modified to simulate oscillation of the TVFs using a reduced order model of vocal folds oscillation.
3. Physiologic geometries of the human and canine larynges will be extracted from CT scan images and fully-resolved simulations will be performed in the physiologic Reynolds numbers and laryngeal geometries.
4. A high order finite volume based moving least square solver compatible with the Cartesian flow solver will be developed and validated.

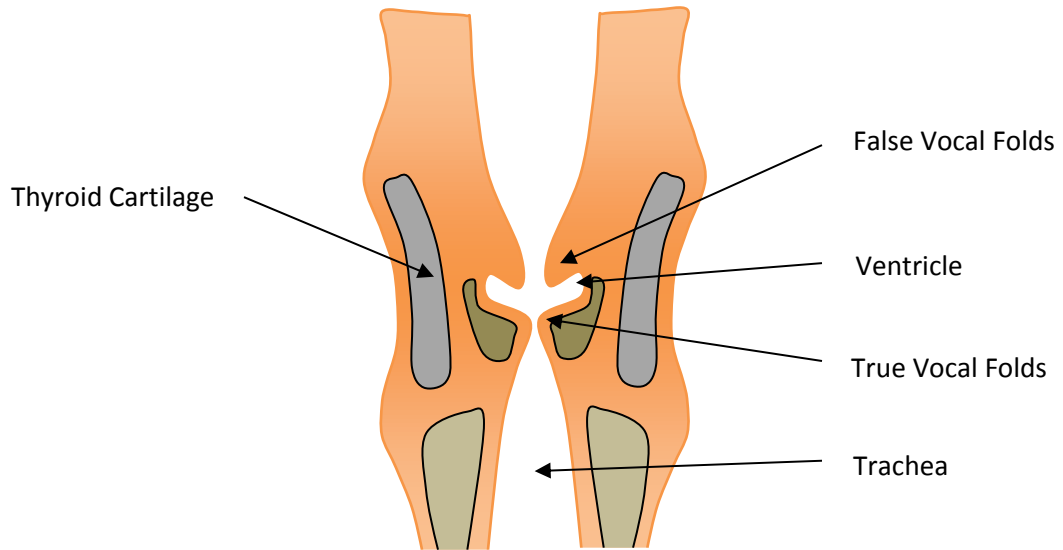


Figure 1-1 A cross section of the larynx.

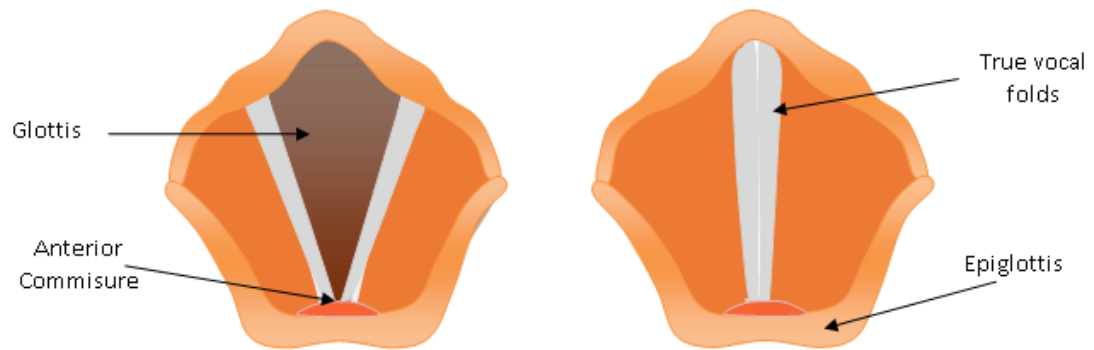


Figure 1-2 Top view of the larynx during inspiration (left) and adducted posture (right).

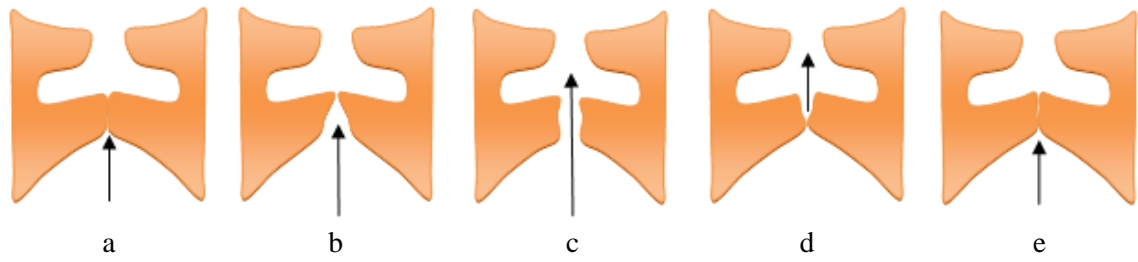


Figure 1-3 A schematic view of a single cycle of phonation.

## CHAPTER 2 EXPERIMENTAL APPARATUS

### 2.1 Introduction

Sound production in the human larynx occurs during the vibration of the TVFs. The balance between the viscoelastic force of the TVF tissues and the aerodynamic forces of the air flow creates this oscillatory phenomenon. The aerodynamic force is composed of pressure and viscous shear contributions. In the presence of the strong glottal jet in the larynx, pressure is the dominant aerodynamic force. Therefore, having knowledge about the pressure distribution on the surface of the TVFs, FVFs and LV can provide an insight about the phonation process. Unfortunately, accurate measurement of experimental pressure during the vibration of the TVFs is extremely challenging. Therefore, experimental pressure data on the surface of the larynx are usually reported for the static and rigid model of the larynx.

In order to investigate the effect of the FVFs shape and geometry on pressure distribution on the surface of the larynx, a series of experimental studies were performed in the current work using rigid laryngeal models. This chapter describes the experimental setup and measurement approaches. The models are tested in a low-speed real size wind tunnel. The pressure data are analyzed in chapter 5 to better understand the role of the FVFs shape and geometry on human phonation. Moreover, they are employed to validate the computational approach.

### 2.2 Experimental Models

The experimental models were designed based on the equations given by Nomura et al. [53] for their laryngeal models. The coefficients of these equations were slightly modified to better represent the geometry of the larynx. The equations are as follows:

$$w_L(x) = w_{L1}(x) + w_{L2}(x) \tag{1.1}$$

where

$$w_{L1}(x) = \frac{1}{2}(A_1 + A_2 + (A_1 - A_2) \tanh s(x)), \quad (1.2)$$

$$w_{L2}(x) = \begin{cases} 0, & x < H_{FVF} - \Delta H_{FVF1} \\ w_{L2a}(x), & H_{FVF} - \Delta H_{FVF1} < x < H_{FVF}, \\ w_{L2b}(x), & x > H_{FVF} \end{cases} \quad (1.3)$$

$$w_{L2a}(x) = \frac{1}{2}(G_{FVF} - W_{VL}) \left(1 + \cos\left(\pi \frac{x - H_{FVF}}{\Delta H_{FVF1}}\right)\right), \quad (1.4)$$

$$w_{L2b}(x) = W_{Sup} - W_{VL} + (G_{FVF} - W_{Sup}) \exp\left(-\frac{1}{2}\left(\frac{x - H_{FVF}}{\Delta H_{FVF2}}\right)^2\right), \quad (1.5)$$

and

$$\left. \begin{aligned} A_1 &= W_{sub}, \quad A_1 = G_{TVF} \\ s(x) &= a_- |x + c_-| - \frac{b_-}{|x + c_-|} \end{aligned} \right\} \quad \text{for } x \leq 0, \quad (1.6)$$

$$\left. \begin{aligned} A_1 &= W_{VL}, \quad A_1 = G_{TVF} \\ s(x) &= a_+ x - \frac{b_+}{x} \end{aligned} \right\} \quad \text{for } x > 0, \quad (1.7)$$

The parameters used in the above equations are defined in Figure 2-1. Moreover,  $\Delta H_{FVF1} = 3.8 \text{ mm}$ ,  $\Delta H_{FVF2} = 3 \text{ mm}$ ,  $a_- = 0.15 \text{ mm}$ ,  $b_- = 6 \text{ mm}$ ,  $c_- = 0.4 \text{ mm}$ ,  $a_+ = 2.4 \text{ mm}$ ,  $b_+ = 2 \text{ mm}$  are constant parameters. The TVFs in the models were parallel with a glottal gap of 1 mm.

Seven laryngeal models were created for the experimental study. The selected sizes of  $G_{fvf}$ ,  $H_{fvf}$ , and  $W_{lv}$  of these models fall in the overlap of the ranges that Agarwal et al. [20] reported for the measurements of the human larynx for two groups of normal people and trained singers. The model which was built based on the average value of the aforementioned parameters is named C1 or control model in this dissertation. The values of these geometrical parameters are reported in Table 2-1, and the corresponding location within the larynx can be seen in Figure 1-1.

The wind tunnel used for the experiments was originally designed for a scaled up TVF; therefore, its design was modified such that a two-sided laryngeal model can be mounted. Due to this modification, for each laryngeal model two separate parts were

designed using the CAD program Pro/Engineer for the bottom and the top side of the wind tunnel. The models were manufactured from acrylonitrile butadiene styrene plastic material using a 3D rapid prototype machine. The bottom and top side of the control model are shown in Figure 2-2 and Figure 2-3 respectively. Six pressure taps were created at the center of the model in the inferior–superior direction normal to the surface of the laryngeal models. The diameter of the pressure tap was 0.86 mm. The locations of these taps were at the subglottic region, TVFs, laryngeal ventricle, FVFs, and supraglottic region. These pressure taps and their corresponding numbering labels are shown in Figure 2-1.

### 2.3 Experimental Apparatus and Data Collection

A low speed real-size wind tunnel was employed for the experiments with a uniform rectangular cross-section of 20 mm high and 25 mm wide. The rectangular duct upstream of the models was 0.8 m long and the downstream duct was 0.6 m long. The tunnel was an open circuit and the air flow was pulled through the tunnel using a vacuum source with adjustable speed. A flow resistance was installed at the end of the tunnel for fine tuning of the gauge pressure. In each experiment, a pressure drop was created across the model by changing the flow rate in the wind tunnel. The pressure data was collected after a stable flow was established in the wind tunnel.

The downstream of the model was connected to a Dwyer flow meter (model VFC131) using a flexible tube. Moreover, a Rudolph 4700B pneumotach was placed at the entrance of the tunnel to measure the mean flow. This measurement instrument converts the air flow to the proportional differential pressure signals. The pressure signals were consequently converted to analog electrical signals using a Validyne pressure transducer (model DP45) and were sent to a computer. The computer recorded the mean flow after converting the signal according to the pressure-flow graph of the pneumotach.

The mean differential pressure drop across the model was measured using a Dwyer monometer. This monometer was connected to two pressure taps, 30 mm upstream and 23 mm downstream of the model and located at the lower wall of the tunnel. The pressure taps on the laryngeal model were connected to a Validyne pressure transducer (model DP45) through a wafer-type pressure switch. The pressure switch was controlled by a computer using a Matlab program. It switched sequentially between the pressure taps and collected the pressure data at predefined time intervals. A schematic of the wind tunnel and a close-up view of the model are depicted in Figure 2-4 and Figure 2-5.

Table 2-1 Summary of geometrical parameters used to design the laryngeal models for the experimental study.

	C1	G2	G4	H1	H2	L1	L2
$G_{fvf}$	5.1	3.3	7.5	5.1	5.1	5.1	5.1
$H_{fvf}$	6.2	6.2	6.2	5.3	7.5	6.2	6.2
$W_{lv}$	15.0	15.0	15.0	15.0	15.0	10.3	19.7

Note: C1 is the control model which is approximately designed based on average laryngeal geometries. All the parameters are defined in millimeters.

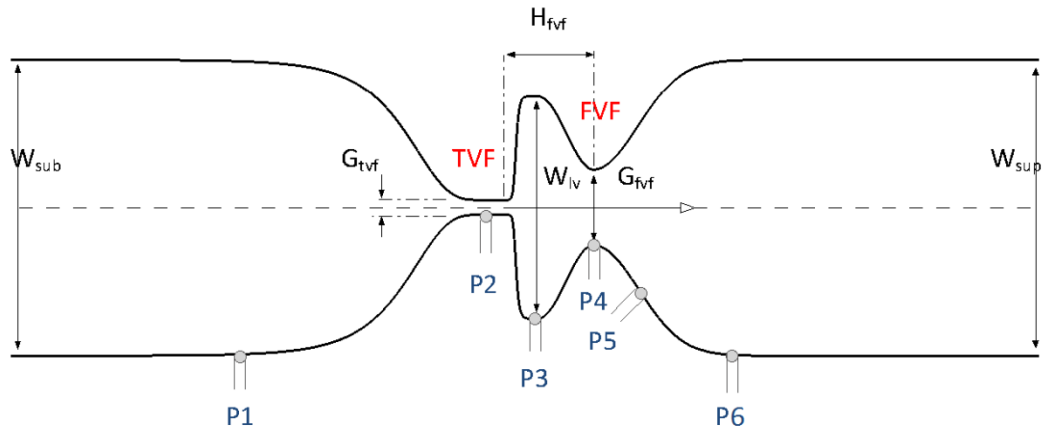


Figure 2-1 Schematic view of the laryngeal models,  $W_{sub}$  = width of subglottal region,  $W_{sup}$  = width of supraglottal region,  $W_{VL}$  = width of ventricle of the larynx,  $H_{fvf}$  = height between FVFs and TVFs,  $G_{tvf}$  = TVF gap,  $G_{fvf}$  = FVF gap.  $G_{tvf} = 1mm$ , and  $W_{sub} = W_{sup} = 20mm$  are constant for all models. The location of the pressure taps on the surface of the experimental models is shown in the lower side of the larynx.

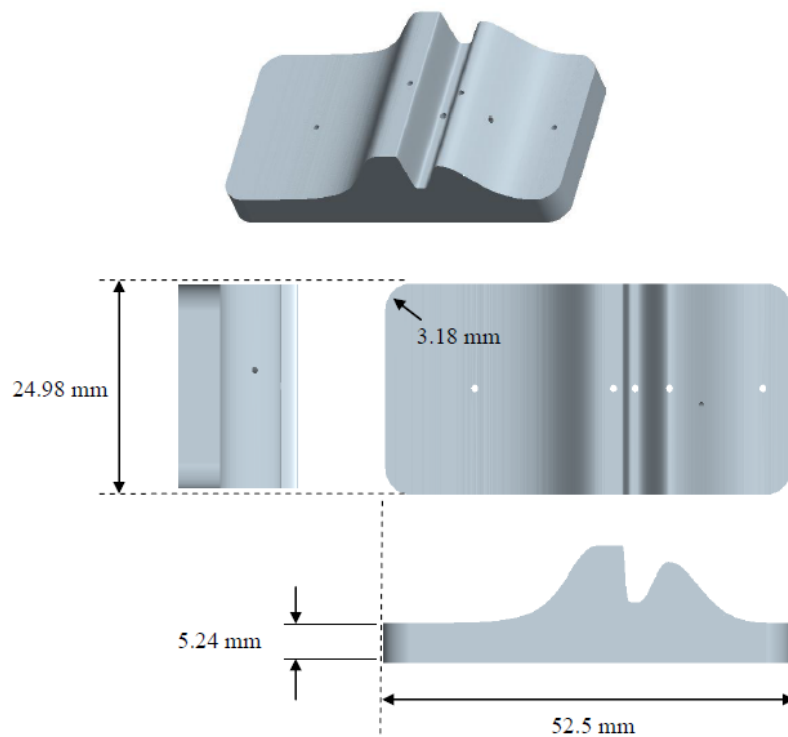


Figure 2-2 Schematic view of the CAD design for the bottom side of the C1 model designed by Pro/Engineer software.

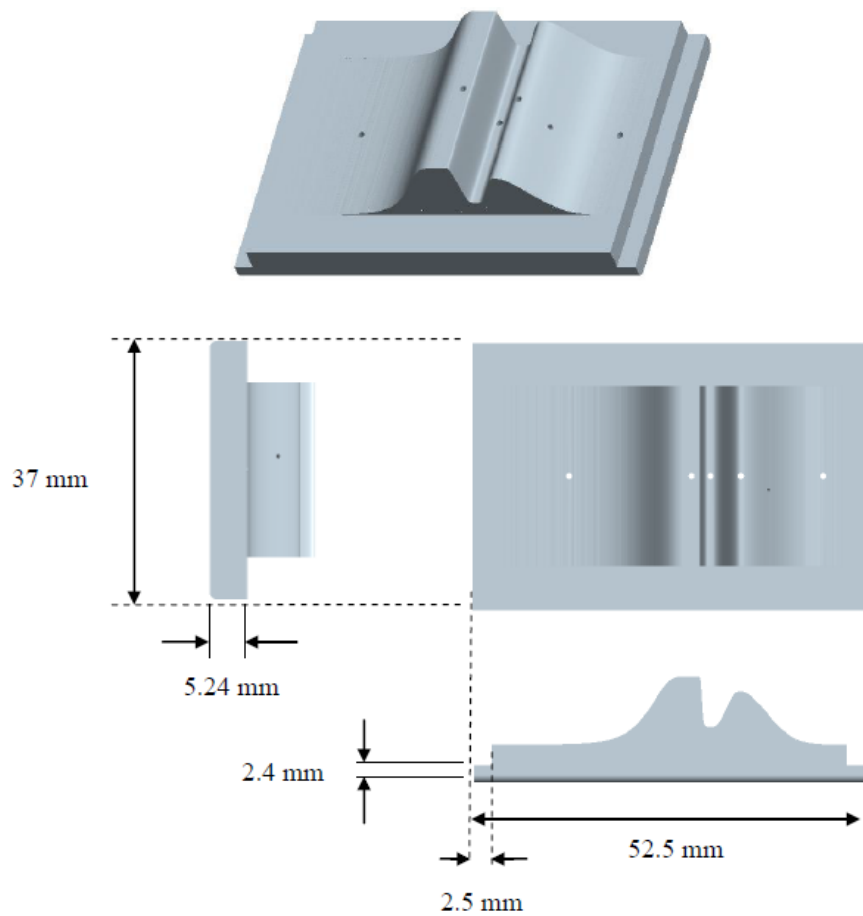


Figure 2-3 A schematic view of the CAD design for the top side of the C1 model designed by Pro/Engineer software

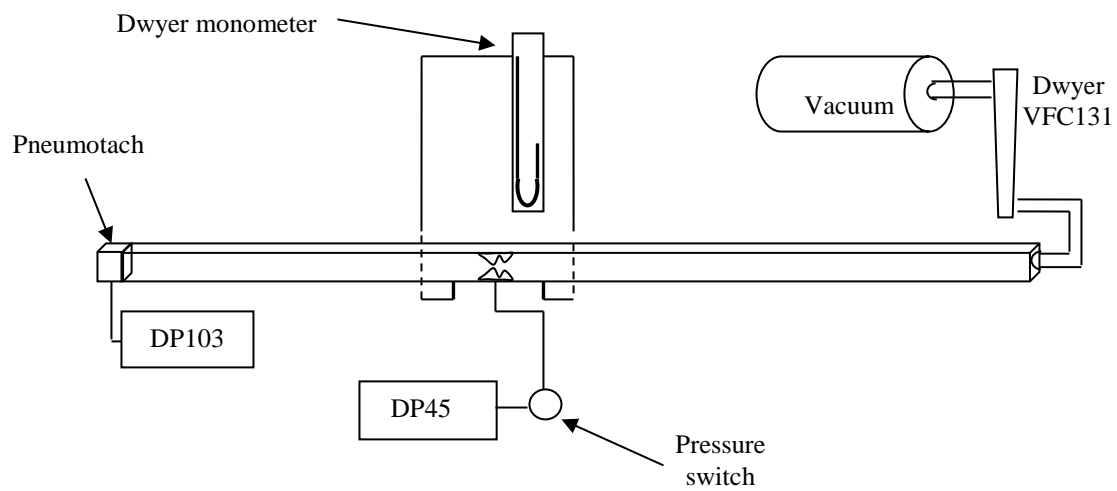


Figure 2-4 A schematic view of the wind tunnel and experimental set up

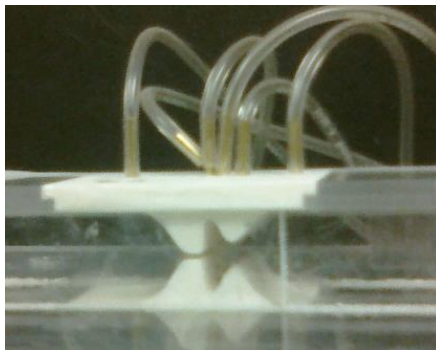


Figure 2-5 A close-up of the experimental model connected to the pressure taps

## CHAPTER 3 INCOMPRESSIBLE SOLVER

### 3.1 Introduction

One of the main elements of the voice speech is the generation of the glottal jet flow. Three dimensional dynamics of this glottal flow, its separation from TVFs, deflection of the jet toward one side of the vocal tract (Coanda effect), and its interaction with supraglottic structures have been active subjects of study in the past decade. In this chapter an incompressible solver is introduced and validated for the laryngeal flow simulations. This solver is employed for the simulation of the glottal jet flow in Chapter 5 and Chapter 6.

The physiologic geometry of the larynx is complex including small vocal folds gap and sharp curvatures. The vocal folds oscillate with high frequencies and collide with each other during the speech phonation. Owing to these features, simulation of the human larynx is extremely complicated or impossible for most available computational solvers. In the current incompressible solver, complex geometries are embedded in a fixed Cartesian grid and are represented using level-set fields [54]. Therefore, the complexity of the structure grid generation, high memory requirement of unstructured grids and cumbersome re-meshing procedure when the interfaces move is avoided. Boundaries are treated sharply using a ghost fluid method with high-order weighted least square extrapolations. The computational solver is massively parallel.

### 3.2 Governing Equations

The Mach number in the larynx is approximately 0.1, hence, the glottal flow can be assumed to be incompressible. The unsteady incompressible Navier-Stokes equations governing these flows are as follows:

$$\nabla \cdot \vec{u} = 0 \tag{3.1}$$

$$\frac{\partial \vec{u}}{\partial t} + \vec{u} \cdot \nabla \vec{u} = -\frac{1}{\rho} \nabla p + \nu \nabla^2 \vec{u} \quad (3.2)$$

where  $\vec{u}$ ,  $p$ ,  $\rho$ , and  $\nu$  are the fluid velocity, pressure, density, and kinematic viscosity respectively. The maximum inlet velocity,  $U$ , and the size of the inlet boundary,  $D$ , can be used to non-dimensionalize the Navier-Stokes equation:

$$x^* = \frac{x}{D}, u^* = \frac{u}{U}, t^* = \frac{tU}{D}, p^* = \frac{p}{\rho U^2}. \quad (3.3)$$

Here, the superscript \* refers to non-dimensional variables and the Reynolds number is defined as  $Re = (UD)/\nu$ .

### 3.3 Fractional Step Algorithm

In the current Cartesian grid method, spatial discretization is built based on a cell-centered collocated arrangement of the primitive variables. In order to increase the robustness of the flow solver, cell-face mass-conserving velocities are also calculated and stored. A four step fractional scheme is used to compute the primitive variables in the next time step [55]. This fractional method has the following sub-steps:

**First step:** This step provides the first provisional velocity field ( $\vec{u}^*$ ) by solving an unsteady advection-diffusion equation. For this purpose, a second-order accurate Adams-Bashforth method is applied to the convective term in an explicit fashion. The resulting advection-diffusion equation of this step is:

$$\vec{u}^* - \vec{u}^n = \Delta t \left[ \frac{1}{2} (H(\vec{u}^{n-1}) - 3H(\vec{u}^n)) + \frac{1}{2Re} (L(\vec{u}^*) + L(\vec{u}^n)) - G(P^{n-\frac{1}{2}}) \right]. \quad (3.6)$$

Here,  $H$ ,  $L$ , and  $G$  are numerical approximations of the non-linear term, the Laplacian, and the gradient operators.

**Second step:** In this step the pressure estimation used for calculation of  $\vec{u}^*$  will be removed to obtain the second intermediate velocity field:

$$\vec{u}^{**} = \vec{u}^* + \Delta t G(P^{n-\frac{1}{2}}) \quad (3.7)$$

**Third step:** In this step, the effect of incompressibility is enforced. Here, the Helmholtz-Hodge decomposition theorem is used to derive a Poisson equation for a

projection pressure field. The Helmholtz-Hodge decomposition theorem states that any vector field such as  $\vec{u}^{**}$  could be decomposed into the sum of a divergence free vector  $\vec{v}$  and the gradient of a scalar  $\varphi$ . This statement could be written as:

$$\vec{u}^{**} = \vec{u}^{n+1} + \Delta t \nabla \varphi \quad (3.8)$$

Taking the divergence of the above equation result in the following Poisson equation:

$$\nabla^2 \varphi = \frac{\nabla \cdot \vec{u}^{**}}{\Delta t} \quad (3.9)$$

The scalar  $\varphi$  could be related to pressure when discretization of the governing equation is taken into account. Considering a Neumann boundary condition, the following equations will be solved to obtain  $P^{n+\frac{1}{2}}$ .

$$L\left(P^{n+\frac{1}{2}}\right) = \frac{\nabla \cdot \vec{u}^{**}}{\Delta t} \quad (3.10)$$

$$G\left(P^{n+\frac{1}{2}}\right) \cdot \vec{n} \Big|_{\partial\Omega} = 0 \quad (3.11)$$

**Fourth step:** In this step the second provisional velocity is projected onto a divergence-free sub-space whereby final velocity will be determined as

$$\vec{u}^{n+1} = \vec{u}^{**} - G\left(P^{n+\frac{1}{2}}\right) \Delta t \quad (3.12)$$

### 3.4 Interface Treatment

The ghost fluid method (GFM) is used in the current solver to impose boundary conditions at the interfaces boundaries. The approach is similar in spirit to the GFM employed for the acoustic solver in Chapter 4. However, in the incompressible solver we are interested in enforcement of the boundary conditions in implicit treatments of operators.

The idea of GFM is to extend the solution into a series of ghost cells near the immersed boundary such that the boundary condition is satisfied on the interface. The extension will be done through the construction of an extrapolation function. The current

incompressible solver performs the extrapolations using a weighted least squares fit. The least squares extrapolations increase the robustness of the solver to apply boundary conditions on complex biomedical geometries.

Consider the Cartesian grid shown in Figure 3-1. The ghost cells are the solid cells that have at least one fluid cell as the neighbor. To assign an appropriate value to ghost cells, the projection of the ghost cell on the interface in the normal direction from the ghost cell to the interface is found. This point is named the interfacial interception point of the ghost cell. Since the boundary condition is known on the interfacial interception point, it is possible to construct a weighted least square fit to extrapolate the unknown value of an arbitrary field  $\varphi$  in the ghost cell. The weighted least square fit is created using multi-dimensional polynomial basis functions of order  $M$  and  $N$  cloud points around the interfacial interception point. A two dimensional quadratic polynomial basis is given in Equation (3-13).

$$\tilde{\varphi}(\mathbf{x}_{rel}) = \alpha_1 + \alpha_2 x_{rel} + \alpha_3 y_{rel} + \alpha_4 x_{rel} y_{rel} + \alpha_5 x_{rel}^2 + \alpha_6 y_{rel}^2 \quad (3-13)$$

$$\mathbf{x}_{rel} = \frac{\mathbf{x} - \mathbf{x}_{int}}{h} \quad (3-14)$$

$$h = 0.7 \sqrt{\sum_{i=1}^N (\mathbf{x}^i - \mathbf{x}_{int}) \cdot (\mathbf{x}^i - \mathbf{x}_{int})} \quad (3-15)$$

where  $\tilde{\varphi}$  is the extrapolation function,  $\mathbf{x}_{int}$  is the coordinate of interfacial interception point,  $\mathbf{x}^i$  is the coordinate of the  $i^{th}$  cloud point, and  $\alpha_i$  ( $i = 1, \dots, 6$ ) are the unknown coefficient of the least square fit. The  $N$  cloud points for each ghost cell include the ghost cell, interfacial interception point of the ghost cell, fluid cells, and the interfacial interception point of the other ghost cell in the cloud.

The boundary conditions of interest are of the Dirichlet and Neumann types. For Dirichlet boundary conditions, a system of linear equations can be constructed using equation (3-13) for  $N$  cloud points for which the value of  $\varphi$  is known. Additionally,

another system of linear equations can be written for  $N_{int}$  interfacial interception points in the cloud to enforce the Neumann boundary condition.

$$\frac{\partial \tilde{\varphi}(x_{rel})}{\partial \mathbf{n}} = \alpha_2 \frac{\partial(x_{rel})}{\partial \mathbf{n}} + \alpha_3 \frac{\partial(y_{rel})}{\partial \mathbf{n}} + \alpha_4 \frac{\partial(x_{rel}y_{rel})}{\partial \mathbf{n}} + \alpha_5 \frac{\partial(x_{rel}^2)}{\partial \mathbf{n}} + \alpha_6 \frac{\partial(y_{rel}^2)}{\partial \mathbf{n}} \quad (3-16)$$

where  $\mathbf{n}$  is vector of the normal at the interfacial interception point. The total  $N + N_{int}$  equations form the following system of linear equations:

$$\mathbf{A}\mathbf{a} = \boldsymbol{\varphi} \quad (3-17)$$

where  $\mathbf{A}$  is an  $(N + N_{int}) \times M$  matrix of the coordinates of the cloud points,  $\mathbf{a}$  is the vector of unknown coefficients, and  $\boldsymbol{\varphi}$  is the vector of known flow field. The least squares problem is well-posed only if the system of equations is over-determined i.e.  $N + N_{int} > M$ . The unknown coefficients can be obtained by minimizing the following weighted interpolation residual:

$$J(\mathbf{a}) = \sum_{j=1}^M w_j^2 (\mathbf{A}\mathbf{a} - \boldsymbol{\varphi}) \quad (3-18)$$

where  $w$  is a weighting function. The exact solution of the aforementioned minimization is given by:

$$\mathbf{a} = (\mathbf{W}\mathbf{A})^+ \mathbf{W}\boldsymbol{\varphi} \quad (3-19)$$

where  $(\mathbf{W}\mathbf{A})^+$  is the pseudo inverse of the rectangular matrix  $\mathbf{W}\mathbf{A}$ , and  $\mathbf{W}$  is a  $(N + N_{int}) \times (N + N_{int})$  diagonal matrix.

$$\mathbf{W} = \text{diag}[w(\mathbf{x}_{rel}^1), w(\mathbf{x}_{rel}^2), \dots, w(\mathbf{x}_{rel}^N), w(\mathbf{x}_{rel}^{1_{int}}), \dots, (\mathbf{x}_{rel}^{N_{int}})] \quad (3-20)$$

The current solver uses a Gaussian weighting function.

$$w = e^{-\left(\frac{d}{h}\right)^2} \quad (4.14)$$

where  $d$  is a measure of distance between the interfacial interception point and other in the compact support

The pseudo inverse in Equation (3-19) can be computed directly using singular value decomposition (SVD) or QR factorization. An alternative and less computationally expensive method to find the inverse of  $\mathbf{W}\mathbf{A}$  is pre-multiplication of both sides of

Equation (3-17) by transpose of  $\mathbf{A}$  which results in a square augmented coefficient matrix that can be inverted with standard numerical methods.

$$\mathbf{A}^+ = (\mathbf{A}^T \mathbf{A})^{-1} \mathbf{A}^T \quad (3-21)$$

which results in the following solution:

$$\mathbf{a} = \mathbf{A}^+ \mathbf{W} \boldsymbol{\varphi} \quad (3-22)$$

The values of  $\mathbf{a}$  only depend on the location of the cloud points. The appropriate value of the ghost cell for Dirichlet boundary condition is formulated for an arbitrary field  $\varphi$  in the following form:

$$\varphi_g = \frac{(\varphi_{int} - \sum_{i=1, i \neq ig}^n A^+(1,i) \varphi(x_{rel}^i))}{A^+(1,ig)} \quad (3-23)$$

and for the Neumann boundary condition the value of the ghost  $\varphi_g$  is:

$$\varphi_g = \frac{(\frac{\partial \varphi_{int}}{\partial n} - \sum_{i=1, i \neq ig}^n \mathbf{n} \cdot (A^+(2,i) \hat{i} + A^+(3,i) \hat{j}) \varphi(x_{rel}^i))}{\mathbf{n} \cdot (A^+(2,ig) \hat{i} + A^+(3,ig) \hat{j})} \quad (3-24)$$

where  $ig$  is the index number of the ghost cell, and  $\varphi_{int}$  and  $\partial \varphi_{int} / \partial n$  are Dirichlet and Neumann boundary condition at the interfacial interception point of the ghost cell.

### 3.5 Level Set Fields

In the current solver the immersed boundaries are represented using level set fields  $\psi$  in a narrow band. The idea of level set is to create a scalar field  $\psi(x, t)$  to identify the interface.  $\psi(x, t)$  is a signed distance scalar from  $x$  to the closest point on the interface [54]. Hence, the interface is represented with a zero level set field. In the current solver sign of the level set field inside the fluid domain is positive and solid domain is represented with negative level set field. If the normal velocity of the interface ( $V_n$ ) is known, the interface can be tracked by solving the advection Equation (3-25) [54, 56].

$$\frac{\partial \psi}{\partial t} + V_n \cdot \nabla \psi = 0 \quad (3-25)$$

The value of  $V_n$  is identified based on the physics of the problem. If the interface is stationary, the level set field is generated once during the solver initialization. For the

moving boundary problems in the current work the location of the boundary is known. Therefore, the level set field is generated in each time step for the known location of the interface.

### 3.6 Adaptive Local Mesh Refinement

The incompressible solver is implemented in an adaptive octree-based local mesh refinement (LMR) algorithm to resolve local regions with fine-scale flow structures. These regions are mainly the locations with large gradient of velocity and/or vorticity including the shear layers, regions near the boundaries where the boundary layer exist, and vortex structures. This feature allows the solver to adaptively refine the base grid or coarsen a previously refined grid based on user defined tolerances. If a grid cell satisfies the refinement criteria, it will be replaced by four cells of half the grid spacing in each coordinate direction (one level of refinement). Similarly, a refined grid is coarsened by merging four sub-grid cells [57]. The refinement and coarsening operation satisfies the 2:1 balancing criteria to provide a smooth variation of refinement levels. Since LMR changes computational balance of the parallel cores during the simulation, the computational grid is adaptively repartitioned after LMR operation using the partitioning package ParMETIS [58, 59].

### 3.7 Two-Mass Model of the Vocal Folds

Due to complexity of the simulation of the TVFs oscillation, reduced-order lumped-element models of the vocal folds have been received extensive attention in the speech community. These models are composed of a series of lumped masses, springs and, dampers. They are simple and computationally affordable. The early lumped element methods had only one mass [60]. The major problem of these models is the lack of phase difference between inferior and posterior sides of the TVFs; hence, they are not able to predict the flow separation point on the surface of the vocal folds [61]. Later, the models enhanced by adding more degrees of freedom. In two-mass models, the two

lumped masses oscillate with a phase difference and are able to successfully model the self-sustained oscillation of the vocal folds [62]. This model is widely used for simulation of the vocal folds. In the current work the vocal folds oscillation is modeled using a two-mass model. A comprehensive review of different other lumped element models can be found in [63, 64].

The two-mass model used in the current work is shown in Figure 3-2. The governing equations for the movement of the TVFs are [65]:

$$m_1 \ddot{x}_1 - P_1 L d_1 + c_1 \dot{x}_1 + k_1 x_1 + k_3 (x_1 - x_2) = 0 \quad (3-26)$$

$$m_2 \ddot{x}_2 - P_2 L d_2 + c_2 \dot{x}_2 + k_2 x_2 + k_3 (x_2 - x_1) = 0 \quad (3-27)$$

where  $m$ ,  $k$  and  $c$  are the mass, spring, and damper constants respectively. The values of these parameters are provided in Table 3-1.  $L$  is the length of the TVFs,  $x_1$  and  $x_2$  are the coordinates of the masses and  $P_1$ , and  $P_2$ , are the average air pressure on each mass.

$$P_1 = \int_{\Gamma_{d_1}} p(\mathbf{x}) d\Gamma_{d_1} \quad (3-28)$$

$$P_2 = \int_{\Gamma_{d_2}} p(\mathbf{x}) d\Gamma_{d_2} \quad (3-29)$$

where  $\Gamma_{d_1}$  and  $\Gamma_{d_2}$  are the surface of the TVFs on  $m_1$  and  $m_2$ .

The ratio of the density of the TVF tissue to the density air flow is approximately 1000; therefore, the fluid-tissue interaction is weak and a staggered coupling can be effectively employed to couple the fluid and the laryngeal tissue [66]. In each time step the incompressible solver provides new pressure and velocity fields. The pressure field is integrated on the surface of masses using Equations (3-28) and (3-29). The average pressures  $P_1$ , and  $P_2$  are utilized to integrate the two-mass model using a standard fourth-order Runge Kutta method. Finally, the TVF boundaries are moved based on the new location and velocities of the lumped masses. Once the new location of the interface is known a level-set field is generated.

### 3.8 Validation of the Incompressible Flow Solver for a Laryngeal Geometry

In order to showcase the validity of the computational method for the laryngeal flow simulations, the experiment by Chisari et al. [18] was reproduced using the current computational solver. The test case was composed of two consecutive static constrictions which approximate the TVF and FVF gaps. A uniform base grid ( $dx = 1 \text{ mm}$ ) was used for domain discretization with up to six levels of grid refinement. The simulation was performed in parallel for  $Re = 900$  using 80 cores of the Helium high performance computing cluster at the University of Iowa. The time-step size was adaptive and satisfied  $CFL \leq 0.1$ . The initial number of grid points was 186,856 after the startup refinement and the simulation terminated with 695,895 grid points due to adaptive refinement in regions with high gradients of the velocity and vorticity.

Figure 3-3 compares the vorticity contours of the current solver and the results of Chisari et al. [18] after 3.5, 5.8, 7.2, 7.8, and 9.5 *ms*. A starting vortex (vortex ring) was created and detached from the surface of the first constriction. This vortex structure moved toward the second constriction while it was followed by a trailing jet flow. A second starting vortex simultaneously formed at the location of the second constriction and convected to the outlet boundary. The first vortex moved axially between the constrictions and squeezed into the second slit. The strong interaction between this vortex structure and the walls of the second constriction created a set of secondary vortices which moved backward toward the first slit. Formation of these secondary vortex structures has also been reported in other fundamental fluid dynamics experiments when a vortex ring impinges an interface [67, 68]. These vortices that detach the surface of the interface and move away from the interface in the opposite direction of the initial vortex ring are known as the “rebound vortices.” The described flow dynamics agree well with the flow visualizations and numerical simulation of Chisari et al. [18]. The centers of the two counter rotating vortices of the first starting vortex were tracked as they moved

axially between the two constrictions. The pressure and velocity profiles on the line passing through centroids of these vortices were extracted at 3.73ms 4.43ms 4,78ms, and 5.83. A quantitative comparison with the direct numerical simulation of Chisari et al. [18] in Figure 3-4 shows good agreement.

Table 3-1 The value of the parameters of the two-mass model of the vocal folds.

$m_1$	$m_2$	$k_1$	$k_2$	$k_3$	$c_1$	$c_2$
0.125	0.025	0.08	0.008	0.025	20	20

Note: The units are given in centimeters, grams, and seconds [65].

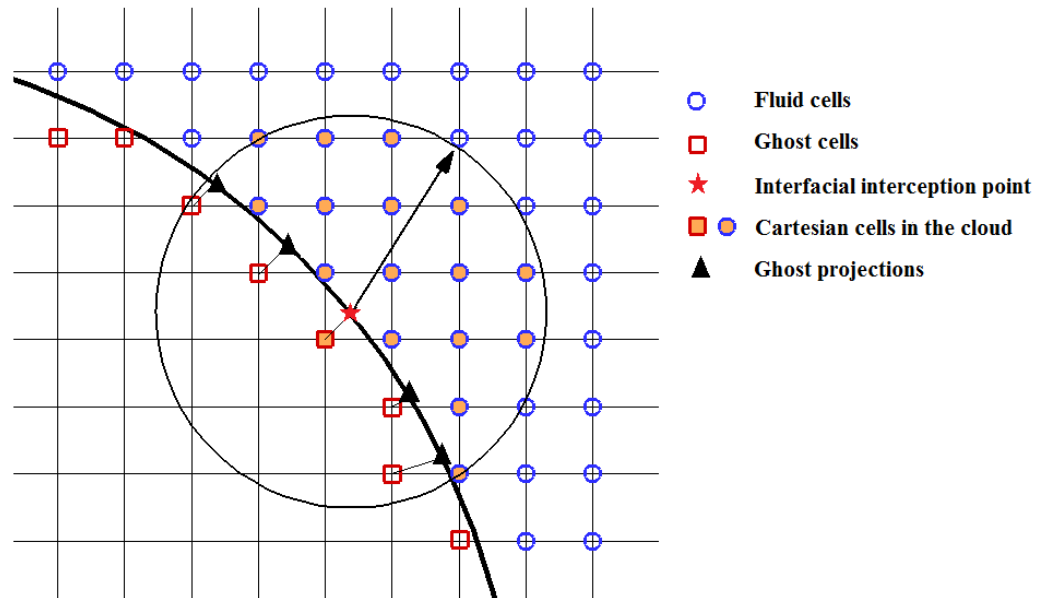


Figure 3-1 A representation of GFM and least square cloud for an arbitrary ghost cell used in the Cartesian Incompressible solver.

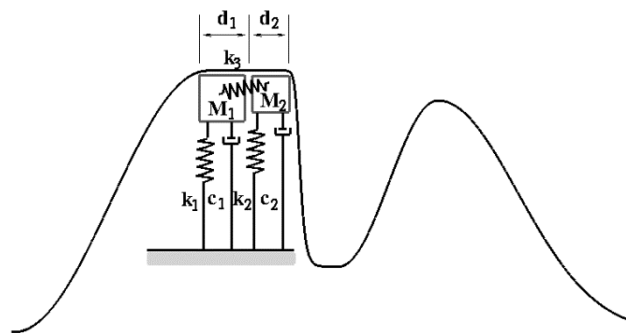


Figure 3-2 Schematic view of one side of the laryngeal model and the two-mass model configuration.

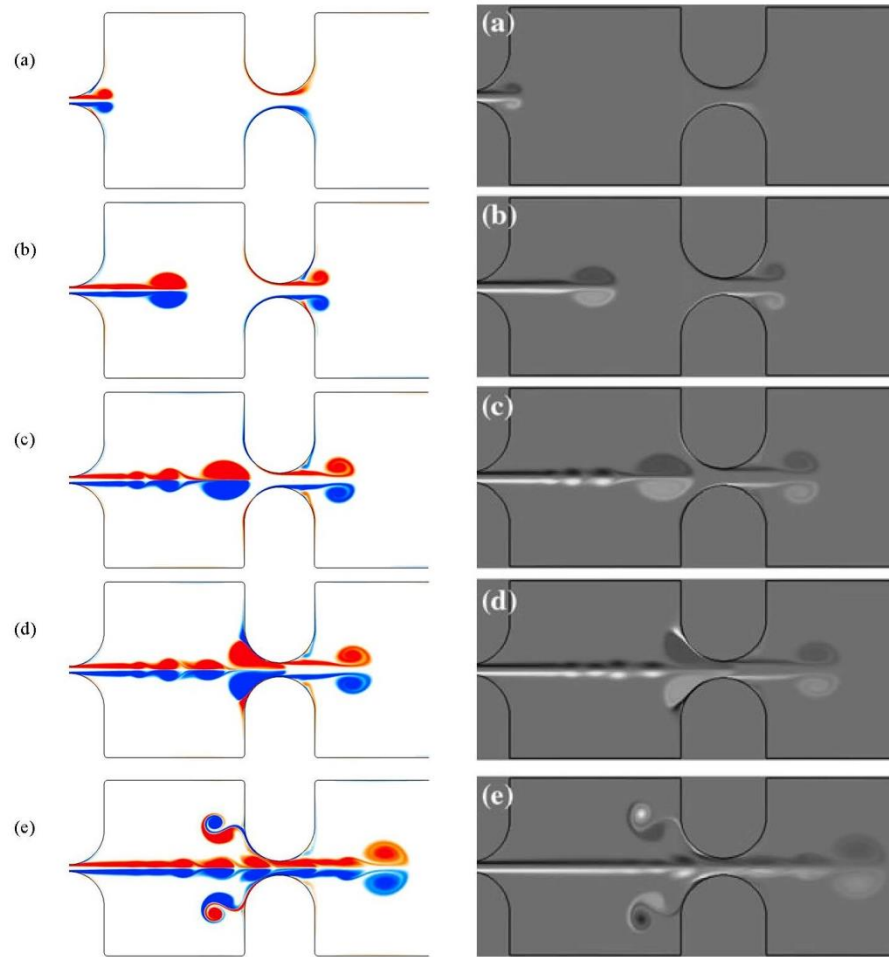


Figure 3-3 Vorticity contour of the air flow in a semi-laryngeal structure of the current Cartesian solver (left) and the direct numerical simulation of Chisari et al. [18] (right) at (a) 3.5 ms, (b) 5.8 ms, (c) 7.2 ms (d) 7.8 ms, and (e) 9.5 ms. The size of first and second constriction gap was 0.04 and 0.08 cm respectively.

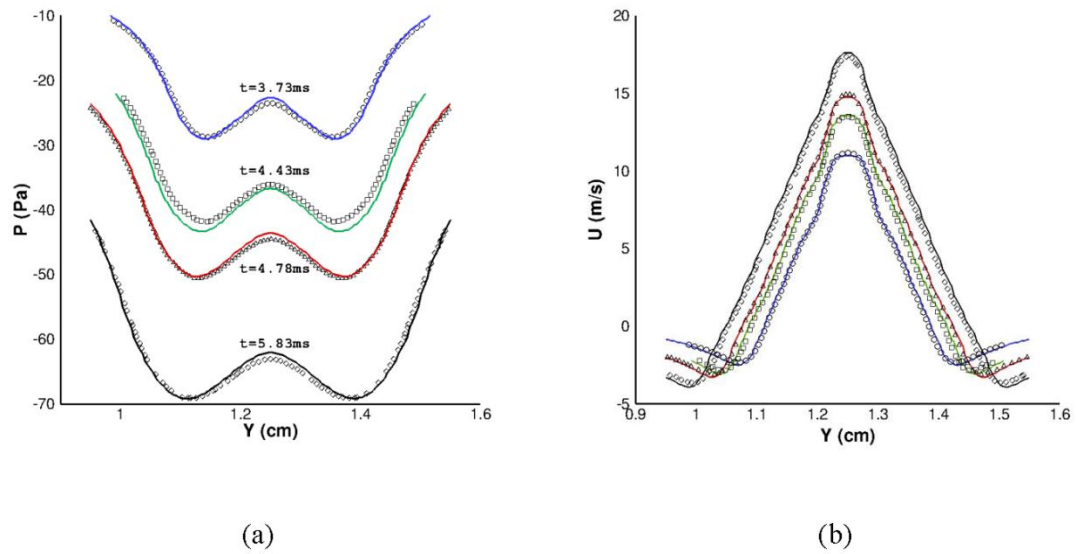


Figure 3-4 A comparison between the current computational solver (solid lines) with the result of Chisari et al. [18] (scattered symbols). (a) pressure and (b) streamwise velocity profiles along the line that connect the starting vortex centroids at times of 3.73ms (circles), 4.43ms (squares), 4.78ms (diamonds), and 5.83 (deltas).

## CHAPTER 4

### ACOUSTIC SOLVER

#### 4.1 Introduction

Accurate aeroacoustic simulations require high-order computational schemes. This chapter describes a high-order acoustic solver developed for computational aeroacoustics with complex geometries. Since we are interested in modeling low Mach number acoustic fields (i.e.  $Ma < 0.3$  [69]), the current solver is developed based on incompressible viscous/acoustic splitting methodology. In this approach, computations are split into viscous incompressible (source model) and inviscid compressible (acoustic propagation) parts. The incompressible solver described in chapter 3 provides the incompressible solution. The acoustic prediction is obtained by solving linearized perturbed compressible equations (LPCE) [70].

The majority of high-order aeroacoustic solvers are developed using high-order finite difference methods on structured grids [71]. The high-order central difference compact method [72] and dispersion-relation-preserving scheme (DPR) [73] are the popular choices. As discussed in Chapter 3, the incompressible solver solves the governing equations of the fluid flow on an unstructured Cartesian grid. Therefore, the ideal choice for an incompressible viscous/acoustic splitting scheme in the current framework is to develop an acoustic solver that is able to perform the computations on the same grid. Recent advances in high-order finite volume methods have introduced powerful computational schemes based on a moving least square (MLS) technique for unstructured grids [74, 75]. These methods were originally developed for body fitted grids [74, 76, 77]. In the current work a high-order finite volume method based on moving least square technique (FVMLS) is developed for acoustic simulations. However, complex geometries are immersed in a Cartesian grid and represented using level set approach. Furthermore, interface boundaries are treated sharply and boundary conditions

on these boundaries are imposed based on ghost-fluid method (GFM) and MLS approximation [78]. Several bench-mark problems are simulated and the solver is validated against existing analytical and computational results.

#### 4.2 Governing Equations and Computational Approach

Low Mach number fluid flow regime ( $Ma < 0.3$ ) encompasses a broad range of engineering and real life phenomena including the laryngeal flow aerodynamics. In general, the compressible Navier-Stokes equations can be solved directly to simulate the fluid flow and acoustic propagation simultaneously [71]. However, in the low Mach number regime, the fluid flow is nearly incompressible. The zero Mach number is a singular limit of the compressible Navier-Stokes equations. In this asymptotical state, the speed of sound becomes infinity and the type of the governing equations of the fluid flow changes. The fluid flow can be assumed divergent free and the equation of state disappears in the pressure computations. Instead, pressure is computed using an elliptic coupling with the flow velocity. Moreover, there is a large discrepancy between the acoustic and convective eigenvalues in the low Mach number flow regime. Therefore, direct numerical simulation of aeroacoustic fields become inefficient and special treatments are required at this flow regime [79].

Hybrid methods have received considerable attention for computational prediction of the flow-generated sound at low Mach number limit. These approaches enable a decoupled computation of the incompressible flow field and sound. In these approaches, incompressible flow simulation is performed using an incompressible solver and far-field sound is obtained by solving an acoustic analogy or numerical simulation of aeroacoustic equations [80]. This treatment is based on the assumption of one-way coupling between the incompressible flow field and the generated sound [80]. Since acoustic waves carry a small portion of the flow energy in low Mach number regime [71], neglecting the

backscattering effects of acoustic field into incompressible flow is considered a legitimate assumption for the one-way coupling at low Mach number simulations.

Hardin and Pope [81] suggested a hybrid method for prediction of the flow-generated sound. In this approach the incompressible flow is simulated to obtain unsteady noise-generating flow regions and acoustic sound is predicted by solving a perturbed Euler equation. The perturbed Euler equation (PEE) is derived by splitting the flow variables into an incompressible part and compressible perturbations around the incompressible state.

$$\rho = \rho' + \rho_0 \quad (4.1)$$

$$u_i = u'_i + u_{0i} \quad (4.2)$$

$$p = p' + p_0 \quad (4.3)$$

where  $\rho_0$ ,  $u_{0i}$ , and  $p_0$  are incompressible density, velocity, and pressure and  $\rho'$ ,  $u'_i$ ,  $p'$  are acoustic perturbations.  $i = 1,2,3$  is the index of the tensor notation. The advantage of this method over other hybrid methods that employ acoustic analogies for sound prediction is direct generation of an acoustic field from the governing equation of the compressible flow. Therefore, acoustic computations are not affected by the assumptions of the acoustic analogies.

The incompressible viscous/acoustic splitting method was extended by Shen [82, 83], Slimon et al. [84], and Seo et al. [69]. Seo et al. [69] derived a set of perturbed compressible equations through the analysis of the perturbed vorticity transport equations to address false generation of the perturbed vorticity in PEE. Subsequently, they linearized the perturbed compressible equations and excluded dominant source terms of the perturbed vorticity transport that were not responsible for sound generation [70]. The linearized perturbed compressible equations (LPCE) are:

$$\frac{\partial \rho'}{\partial t} + u_{0j} \frac{\partial \rho'}{\partial x_j} + \rho_0 \frac{\partial u'_j}{\partial x_j} = 0 \quad (4.4)$$

$$\rho_0 \frac{\partial \dot{u}_j}{\partial t} + \rho_0 \frac{\partial(\dot{u}_i u_{0i})}{\partial x_j} + \frac{\partial \dot{p}}{\partial x_j} = 0 \quad (4.5)$$

$$\frac{\partial \dot{p}}{\partial t} + u_{0j} \frac{\partial \dot{p}}{\partial x_j} + \gamma p_0 \frac{\partial \dot{u}_j}{\partial x_j} + \dot{u}_j \frac{\partial p_0}{\partial x_j} = - \left( \frac{\partial p_0}{\partial t} + u_{0j} \frac{\partial p_0}{\partial x_j} \right) + \dot{s} \quad (4.6)$$

where  $\gamma$  is the ratio of the specific heats and  $\dot{s}$  is any additional prescribed acoustic sources [70]. LPCE is computationally stable and accurate at low Mach number regime and are used in the current acoustic solver for the prediction of flow-induced sound.

### 4.3 Moving Least Square Method

The basic premise of MLS derives from the Stone-Weierstrass theorem. The Stone-Weierstrass theorem states that a smooth function  $u(\mathbf{x})$  on  $\Omega \in \mathbb{R}^n$  can be locally approximated at a given point  $\bar{\mathbf{x}}$  in a compact support  $\Omega_x$  by a polynomial function  $\mathbf{p}_i$  (

Figure 4-1).

$$u(\bar{\mathbf{x}}) \cong \hat{u}(\bar{\mathbf{x}}) = \sum_{i=1}^m p_i(\mathbf{x}_{rel}) \alpha_i(\bar{\mathbf{x}}) = \mathbf{p}^T(\mathbf{x}_{rel}) \boldsymbol{\alpha}(\bar{\mathbf{x}}) \quad (4.7)$$

where  $m$  is the number of polynomial basis  $\mathbf{p}_i$ ,  $\alpha_i$  is its unknown coefficients. In Equation (4.7)  $\mathbf{x}_{rel} = (\mathbf{x} - \bar{\mathbf{x}})/h$  is used instead of the Cartesian coordinates to improve the conditioning of the matrices. Moreover,  $h$  is a measure of the compact support  $\Omega_x$  and  $\mathbf{p}^T(\mathbf{x}_{rel})$ , and  $\boldsymbol{\alpha}(\bar{\mathbf{x}})$  are:

$$\mathbf{p}^T(\mathbf{x}_{rel}) = [p_1(\mathbf{x}_{rel}) \quad p_2(\mathbf{x}_{rel}) \quad \dots \quad p_m(\mathbf{x}_{rel})]_{1 \times m}, \quad (4.8)$$

$$\boldsymbol{\alpha}(\bar{\mathbf{x}}) = \begin{bmatrix} \alpha_1(\bar{\mathbf{x}}) \\ \alpha_2(\bar{\mathbf{x}}) \\ \vdots \\ \alpha_m(\bar{\mathbf{x}}) \end{bmatrix}_{m \times 1}. \quad (4.9)$$

Examples of linear, quadratic, and cubic 2D polynomial basis functions are:

$$\mathbf{p}(\vec{x}) = (1 \quad x \quad y)^T \quad (4.10)$$

$$\mathbf{p}(\vec{x}) = (1 \quad x \quad y \quad xy \quad x^2 \quad y^2)^T \quad (4.11)$$

$$\mathbf{p}(\vec{x}) = (1 \quad x \quad y \quad xy \quad x^2 \quad y^2 \quad x^2y \quad xy^2 \quad x^3 \quad y^3)^T \quad (4.12)$$

The unknown  $\alpha(\bar{\mathbf{x}})$  can be determined from minimization of the following weighted error functional:

$$J(\alpha(\bar{\mathbf{x}})) = \int_{\mathbf{y} \in \Omega_{\mathbf{x}}} w^h(\mathbf{y} - \bar{\mathbf{x}}) \left[ u(\mathbf{y}) - \mathbf{p}^T \left( \frac{\mathbf{y} - \bar{\mathbf{x}}}{h} \right) \alpha(\bar{\mathbf{x}}) \right]^2 d\Omega_{\mathbf{x}} \quad (4.13)$$

where  $w^h$  is a weighting or kernel function. Various kernel functions have been suggested for MLS. Spline and Gaussian kernels are widely utilized for MLS calculations. The Gaussian function is as follows:

$$w^h = \lambda e^{-\left(\frac{d}{h}\right)^2} \quad (4.14)$$

where  $\lambda$  is a parameter which depends on the dimension of the problem, and  $d$  is a measure of distance between the desired point and its neighbor in the kernel support.  $\partial J / \partial \alpha = 0$  yields to:

$$\begin{aligned} \alpha(\bar{\mathbf{x}}) \int_{\mathbf{y} \in \Omega_{\mathbf{x}}} \mathbf{p} \left( \frac{\mathbf{y} - \bar{\mathbf{x}}}{h} \right) w^h(\mathbf{y} - \bar{\mathbf{x}}) \mathbf{p}^T \left( \frac{\mathbf{y} - \bar{\mathbf{x}}}{h} \right) d\Omega_{\mathbf{x}} \\ = \int_{\mathbf{y} \in \Omega_{\mathbf{x}}} \mathbf{p} \left( \frac{\mathbf{y} - \bar{\mathbf{x}}}{h} \right) w^h(\mathbf{y} - \bar{\mathbf{x}}) u(\mathbf{y}) d\Omega_{\mathbf{x}} \end{aligned} \quad (4.15)$$

Equation (4-15) can be solved using nodal integration. The quadrature points are  $n$  neighbor nodes in the kernel support. The series form of the integration is given by:

$$\begin{aligned} \alpha(\bar{\mathbf{x}}) \sum_{I=1}^n \mathbf{p} \left( \frac{\mathbf{x}_I - \bar{\mathbf{x}}}{h} \right) w^h(\mathbf{x}_I - \bar{\mathbf{x}}) \mathbf{p}^T \left( \frac{\mathbf{x}_I - \bar{\mathbf{x}}}{h} \right) \forall_I \\ = \sum_{I=1}^n \mathbf{p} \left( \frac{\mathbf{x}_I - \bar{\mathbf{x}}}{h} \right) w^h(\mathbf{x}_I - \bar{\mathbf{x}}) u(\mathbf{x}_I) \forall_I \end{aligned} \quad (4.16)$$

or

$$\alpha(\bar{\mathbf{x}}) = \mathbf{M}^{-1}(\bar{\mathbf{x}}) \mathbf{P}_{\Omega_{\bar{\mathbf{x}}}} \mathbf{W}_{\Omega_{\bar{\mathbf{x}}}} \mathbf{u}_{\Omega_{\bar{\mathbf{x}}}} \quad (4.17)$$

where the moment matrix  $\mathbf{M}(\mathbf{x})$  is:

$$\mathbf{M}(\mathbf{x}) = \sum_{I=1}^n \mathbf{p} \left( \frac{\mathbf{x}_I - \mathbf{x}}{h} \right) w^h(\mathbf{x}_I - \mathbf{x}) \mathbf{p}^T \left( \frac{\mathbf{x}_I - \mathbf{x}}{h} \right) \forall_I = \mathbf{P}_{\Omega_{\mathbf{x}}} \mathbf{W}_{\Omega_{\mathbf{x}}} \mathbf{P}_{\Omega_{\mathbf{x}}}^T \quad (4.18)$$

and  $\mathbf{W}_{\Omega_{\bar{\mathbf{x}}}} = \text{diag}\{w(\mathbf{x}_I - \bar{\mathbf{x}}) \forall_I\}$ , and  $\forall_I$  is the tributary volume which is used as the quadrature weight to formulate MLS reproducing kernel. The formulation without  $\forall_j$  reduces to classical MLS formulation. Defining  $\bar{\mathbf{x}}_{rel}^I = (\mathbf{x}_I - \bar{\mathbf{x}})/h$  as the normalized

relative distance between the nodal point  $I$  and  $\bar{\mathbf{x}}$  in the kernel support, the vectors and matrices in Equation (4-17) are given by:

$$P_{\Omega_{\bar{\mathbf{x}}}} = \begin{bmatrix} p_1(\bar{\mathbf{x}}_{rel}^1) & p_1(\bar{\mathbf{x}}_{rel}^2) & \cdots & p_1(\bar{\mathbf{x}}_{rel}^n) \\ p_2(\bar{\mathbf{x}}_{rel}^1) & p_2(\bar{\mathbf{x}}_{rel}^2) & \cdots & p_2(\bar{\mathbf{x}}_{rel}^n) \\ \vdots & \vdots & \ddots & \vdots \\ p_m(\bar{\mathbf{x}}_{rel}^1) & p_m(\bar{\mathbf{x}}_{rel}^2) & \cdots & p_m(\bar{\mathbf{x}}_{rel}^n) \end{bmatrix}_{m \times n} = \begin{bmatrix} \mathbf{p}(\bar{\mathbf{x}}_{rel}^1) & \mathbf{p}(\bar{\mathbf{x}}_{rel}^2) & \cdots & \mathbf{p}(\bar{\mathbf{x}}_{rel}^n) \end{bmatrix} \quad (4-19)$$

$$\mathbf{u}_{\Omega_{\bar{\mathbf{x}}}} = \begin{bmatrix} u(\mathbf{x}_1) \\ u(\mathbf{x}_2) \\ \vdots \\ u(\mathbf{x}_n) \end{bmatrix} \quad (4-20)$$

$$W_{\Omega_{\bar{\mathbf{x}}}} = \begin{bmatrix} w^h(\bar{\mathbf{x}} - \mathbf{x}_1)\forall_1 & & & 0 \\ & w^h(\bar{\mathbf{x}} - \mathbf{x}_2)\forall_2 & & \\ & & \ddots & \\ 0 & & & w^h(\bar{\mathbf{x}} - \mathbf{x}_n)\forall_n \end{bmatrix} \quad (4-21)$$

Using the basic definition of MLS and substituting  $\alpha_i(\bar{\mathbf{x}})$  we have:

$$\begin{aligned} u(\bar{\mathbf{x}}) &\cong \hat{u}(\bar{\mathbf{x}}) = \sum_{i=1}^m p_i(\mathbf{x}_{rel})\alpha_i(\bar{\mathbf{x}}) = \mathbf{p}^T(\mathbf{x}_{rel})\boldsymbol{\alpha}(\bar{\mathbf{x}}) \\ &= \mathbf{p}^T(\mathbf{x}_{rel})\mathbf{M}^{-1}(\bar{\mathbf{x}})P_{\Omega_{\bar{\mathbf{x}}}}W_{\Omega_{\bar{\mathbf{x}}}}\mathbf{u}_{\Omega_{\bar{\mathbf{x}}}} \end{aligned} \quad (4-22)$$

Analogous to finite element method, Equation (4-22) can be written using the MLS shape function  $N$ .

$$u(\bar{\mathbf{x}}) \cong \hat{u}(\bar{\mathbf{x}}) = \sum_{I=1}^n N_I(\bar{\mathbf{x}})u(\mathbf{x}_I) \quad (4-23)$$

where

$$N^T(\bar{\mathbf{x}}) = \mathbf{p}^T(\mathbf{x}_{rel})\mathbf{M}^{-1}(\bar{\mathbf{x}})P_{\Omega_{\bar{\mathbf{x}}}}W_{\Omega_{\bar{\mathbf{x}}}} \quad (4-24)$$

Equation (4-24) defines a local optimization in the compact support. A global optimization can be obtained by  $\bar{\mathbf{x}} \rightarrow \mathbf{x}$ .

$$u(\mathbf{x}) \cong \hat{u}(\mathbf{x}) = \sum_{I=1}^n N_I(\mathbf{x})u(\mathbf{x}_I) \quad (4-25)$$

where

$$N^T(\mathbf{x}) = \mathbf{p}^T(\mathbf{0})\mathbf{M}^{-1}(\mathbf{x})P_{\Omega_{\mathbf{x}}}W_{\Omega_{\mathbf{x}}} \quad (4-26)$$

and the moment matrix is:

$$\mathbf{M}(\mathbf{x}) = \sum_{l=1}^n \mathbf{p}(\mathbf{x}_{rel}^l) w^h(\mathbf{x}_l - \mathbf{x}) \mathbf{p}^T(\mathbf{x}_{rel}^l) \forall_l = \mathbf{P}_{\Omega_x} \mathbf{W}_{\Omega_x} \mathbf{P}_{\Omega_x}^T \quad (4.27)$$

The MLS problem is well-posed only if the system of equations is over-determined i.e.  $n > m$ . Therefore, the moment matrix  $\mathbf{M}(\mathbf{x})$  is a rectangular matrix. The pseudo-inverse of the moment matrix can be obtained using singular value decomposition (SVD), or QR factorization.

#### 4.4 Finite Volume Formulation

##### 4.4.1 General Finite Volume Formulation of LPCE

The two dimensional conservative form of LPCE (Equations (4-4) to (4-6)) can be written as:

$$\frac{\partial U}{\partial t} + \frac{\partial E}{\partial x} + \frac{\partial F}{\partial y} + H = S \quad (4.28)$$

where

$$E = \begin{bmatrix} \rho u_0 + \rho_0 \dot{u} \\ (\dot{u} u_0 + \dot{v} v_0) + \frac{\dot{p}}{\rho_0} \\ 0 \\ u_0 \dot{p} + \gamma p_0 \dot{u} \end{bmatrix}, \quad F = \begin{bmatrix} \rho v_0 + \rho_0 \dot{v} \\ 0 \\ (\dot{u} u_0 + \dot{v} v_0) + \frac{\dot{p}}{\rho_0} \\ v_0 \dot{p} + \gamma p_0 \dot{v} \end{bmatrix}, \quad (4.29)$$

$$U = \begin{bmatrix} \dot{\rho} \\ \dot{u} \\ \dot{v} \\ \dot{p} \end{bmatrix}, \quad H = \begin{bmatrix} 0 \\ 0 \\ 0 \\ \left( \frac{\partial}{\partial t} + (\dot{u} - u_0) \frac{\partial}{\partial x} + (\dot{v} - v_0) \frac{\partial}{\partial y} \right) p_0 \end{bmatrix}, \quad S = \begin{bmatrix} 0 \\ 0 \\ 0 \\ \dot{s} \end{bmatrix} \quad (4.30)$$

In finite volume method solution domain is subdivided into a finite number of computational cells and integral forms of the governing equation are solved over each cell. The integral form of the Equation (4.28) for control volume  $\Omega_l$  is:

$$\int_{\Omega_l} \left( \frac{\partial U}{\partial t} \right) d\Omega + \int_{\Gamma_l} (\mathcal{F} \cdot \mathbf{n}) d\Gamma_l = \int_{\Omega_l} (S - H) d\Omega \quad (4.31)$$

where  $\mathcal{F}$  is a flux vector and  $\mathbf{n}$  is the normal vector to the control volume face  $\Gamma_l$ . Direct computation of the flux vector using the cell-centered values for hyperbolic partial differential equations can result in unstable computations [77]. To overcome this problem flux vectors are computed using a broken reconstruction of the solution vector  $U^*$  on the

cell faces [74]. A high order reconstruction for a two dimensional cell  $I$  can be obtained using Taylor series expansion:

$$U_{(x-x_I)}^* = \tilde{U}_I + \frac{\partial \tilde{U}_I}{\partial x} \Delta x + \frac{\partial \tilde{U}_I}{\partial y} \Delta y + \frac{1}{2!} \frac{\partial^2 \tilde{U}_I}{\partial x^2} (\Delta x^2 - M_I^{x^2}) + \frac{1}{2!} \frac{\partial^2 \tilde{U}_I}{\partial y^2} (\Delta y^2 - M_I^{y^2}) + \frac{\partial^2 \tilde{U}_I}{\partial x \partial y} (\Delta x \Delta y - M_I^{xy}) + \dots \quad (4.32)$$

where  $\tilde{U}_I$  is the mean value of  $U$  in a two dimensional control volume  $I$ , and  $\Delta x = x - x_I$ ,  $\Delta y = y - y_I$  and  $M_I^{x^m y^n}$  are additional terms to enforce conservation of mean.

$$\tilde{U}_I = \frac{1}{\Delta \hat{A}_I} \int_{\Omega_I} U d\Omega \quad (4.33)$$

$$M_I^{x^m y^n} = \frac{1}{\hat{A}_I} \int_{\Omega_I} (x - x_I)^m (y - y_I)^n dx dy \quad (4.34)$$

where  $\hat{A}_I$  is the area of the cell  $I$ . Figure 4-2 shows the broken fluxes for an arbitrary two-dimensional Cartesian cell  $I$ .

The order of accuracy of the Taylor series expansion should match with the order of the accuracy of the finite volume solver. Derivatives of the field variables in Equation (4-32) are evaluated using MLS approximation. Therefore, we can write:

$$U_{(x-x_I)}^* = \tilde{U}_I + \sum_{i=1}^n \frac{\partial N_i}{\partial x} \tilde{U}_i \Delta x + \sum_{i=1}^n \frac{\partial N_i}{\partial y} \tilde{U}_i \Delta y + \frac{1}{2!} \sum_{i=1}^n \frac{\partial^2 N_i}{\partial x^2} \tilde{U}_i (\Delta x^2 - M_I^{x^2}) + \frac{1}{2!} \sum_{i=1}^n \frac{\partial^2 N_i}{\partial y^2} \tilde{U}_i (\Delta y^2 - M_I^{y^2}) + \sum_{i=1}^n \frac{\partial^2 N_i}{\partial x \partial y} \tilde{U}_i (\Delta x \Delta y - M_I^{xy}) + \dots \quad (4.35)$$

Derivatives of the shape functions are calculated in the current work using the diffuse method:

$$\frac{\partial^k N^T(\mathbf{x})}{\partial x^\alpha \partial y^{(k-\alpha)}} \approx \frac{\partial^k \mathbf{p}^T(\mathbf{0})}{\partial x^\alpha \partial y^{(k-\alpha)}} \mathbf{M}^{-1}(\mathbf{x}) \mathbf{P}_{\Omega_x} \mathbf{W}_{\Omega_x} \quad (4.36)$$

Shape function only depends on the grid topology of the cells inside the MLS cloud. Therefore, for the stationary Cartesian grid used in the current work for acoustic simulations, shape functions are only computed at the initialization step of the acoustic solver and stored for calculations in later time-steps. Additionally, interior acoustic cells away from the boundaries have identical clouds, and thus, they have the same shape

functions. Hence, only one shape function with its underlying neighboring pattern is required to be stored for all the interior cells. Therefore the amount of memory allocation for the shape function storage in the present solver is considerably smaller than the body-fitted solver introduced referenced in [85].

Equation (4-31) using the broken reconstruction is:

$$\frac{\partial \bar{U}_I}{\partial t} \Delta \hat{A}_I + \int_{\Gamma_I} \mathbf{H}(\mathbf{u}^*) \cdot \mathbf{n} d\Gamma_I = \int_{\Omega_I} (S - H) d\Omega \quad (4-37)$$

where  $\mathbf{H}(\mathbf{u}^*) \cdot \mathbf{n}$  is a numerical flux and can be obtained from a standard flux splitting technique. Numerical fluxes are integrated over the cell faces. Additionally,  $H$  and  $S$  are evaluated over the control volume using a midpoint integration.

#### 4.4.2. Standard Flux Vector Splitting Technique

The basic idea of the standard flux vector splitting technique is to upwind the fluxes based on the physical propagation of the acoustic perturbations associated with the characteristics of the LPCE. At the first glance, upwinding might be considered a drawback for a high order method since it increases the dissipation rate of the finite volume scheme. However, a recent comprehensive study on the dispersion and dissipation properties of the FVMLS method has revealed that the introduced dissipation acts mainly on the under-resolved wavenumbers [76]. This provides a desirable implicit low-pass filtering effect for the current solver. Equation (4.28) can be written using the flux Jacobian formulation as:

$$\frac{\partial U}{\partial t} + J_1 \frac{\partial U}{\partial x} + J_2 \frac{\partial U}{\partial y} + H = S \quad (4.38)$$

where the representation of  $U$ ,  $S$  and  $H$  are provided by Equation (4.30). Jacobian matrices in  $x$  and  $y$  directions are:

$$J_1 = \frac{\partial E}{\partial U} = \begin{bmatrix} u_0 & \rho_0 & 0 & 0 \\ 0 & u_0 & v_0 & 1/\rho_0 \\ 0 & 0 & 0 & 0 \\ 0 & \gamma p_0 & 0 & u_0 \end{bmatrix} = \begin{bmatrix} u_0 & \rho_0 & 0 & 0 \\ 0 & u_0 & v_0 & 1/\rho_0 \\ 0 & 0 & 0 & 0 \\ 0 & \rho_0 c^2 & 0 & u_0 \end{bmatrix} \quad (4.39)$$

$$J_2 = \frac{\partial F}{\partial U} = \begin{bmatrix} v_0 & 0 & \rho_0 & 0 \\ 0 & 0 & 0 & 0 \\ 0 & u_0 & v_0 & 1/\rho_0 \\ 0 & 0 & \gamma p_0 & v_0 \end{bmatrix} = \begin{bmatrix} v_0 & 0 & \rho_0 & 0 \\ 0 & 0 & 0 & 0 \\ 0 & u_0 & v_0 & 1/\rho_0 \\ 0 & 0 & \rho_0 c^2 & v_0 \end{bmatrix} \quad (4.40)$$

where  $c$  is the speed of sound. Additionally, Jacobian matrices of the Equation (4-38) can be reformulated based on their eigenvalue and eigenvector matrices in the following form:

$$J_1 = L_1 \Lambda_1 L_1^{-1}, \quad (4.41)$$

$$J_2 = L_2 \Lambda_2 L_2^{-1}, \quad (4.42)$$

where  $\Lambda$ ,  $L$ , and  $L^{-1}$  are the matrices of eigenvalues, left eigenvector, and right eigenvector respectively.

$$\Lambda_1 = \begin{bmatrix} u_0 & 0 & 0 & 0 \\ 0 & u_0 + c & 0 & 0 \\ 0 & 0 & 0 & 0 \\ 0 & 0 & 0 & u_0 - c \end{bmatrix} \quad (4.43)$$

$$L_1 = \begin{bmatrix} 1 & 0 & 0 & -\frac{1}{c^2} \\ 0 & \frac{\rho_0 c}{2} & \frac{\rho_0 v_0 c}{2(u_0 + c)} & \frac{1}{2} \\ 0 & 0 & \frac{\rho_0 v_0 c^2}{u_0^2 - c^2} & 0 \\ 0 & -\frac{\rho_0 c}{2} & \frac{\rho_0 v_0 c}{2(c - u_0)} & \frac{1}{2} \end{bmatrix} \quad (4.44)$$

$$L_1^{-1} = \begin{bmatrix} 1 & \frac{1}{c^2} & \frac{1}{c^2} & \frac{1}{c^2} \\ 0 & \frac{1}{\rho_0 c} & -\frac{u_0}{\rho_0 c^2} & -\frac{1}{\rho_0 c} \\ 0 & 0 & \frac{u_0^2 - c^2}{\rho_0 v_0 c^2} & 0 \\ 0 & 1 & 1 & 1 \end{bmatrix} \quad (4.45)$$

$$\Lambda_2 = \begin{bmatrix} v_0 & 0 & 0 & 0 \\ 0 & 0 & 0 & 0 \\ 0 & 0 & v_0 + c & 0 \\ 0 & 0 & 0 & v_0 - c \end{bmatrix} \quad (4.46)$$

$$L_2 = \begin{bmatrix} 1 & 0 & 0 & -\frac{1}{c^2} \\ 0 & \frac{\rho_0 u_0 c^2}{u_0^2 - c^2} & 0 & 0 \\ 0 & \frac{\rho_0 u_0 c}{2(v_0 + c)} & \frac{\rho_0 c}{2} & \frac{1}{2} \\ 0 & \frac{\rho_0 u_0 c}{2(c - v_0)} & -\frac{\rho_0 c}{2} & \frac{1}{2} \end{bmatrix} \quad (4-47)$$

$$L_2^{-1} = \begin{bmatrix} 1 & \frac{1}{c^2} & \frac{1}{c^2} & \frac{1}{c^2} \\ 0 & \frac{v_0^2 - c^2}{\rho_0 u_0 c^2} & 0 & 0 \\ 0 & -\frac{v_0}{\rho_0 c^2} & \frac{1}{\rho_0 c} & -\frac{1}{\rho_0 c} \\ 0 & 1 & 1 & 1 \end{bmatrix} \quad (4-48)$$

The eigenvalue matrices can be split into positive and negative matrices  $\Lambda^+$  and  $\Lambda^-$  based on the sign of their components. Their corresponding positive and negative Jacobians in each direction are as follows:

$$J_1^+ = L_1 \Lambda_1^+ L_1^{-1}, \quad (4-49)$$

$$J_1^- = L_1 \Lambda_1^- L_1^{-1}, \quad (4-50)$$

$$J_2^+ = L_2 \Lambda_2^+ L_2^{-1}, \quad (4-51)$$

$$J_2^- = L_2 \Lambda_2^- L_2^{-1}, \quad (4-52)$$

Similarly, flux vectors are split into positive and negative sub-vectors. Therefore, the flux vector formula is arranged as follows for broken reconstruction of the solution vector:

$$E^+ = J_1^+ U^*, \quad (4-53)$$

$$E^- = J_1^- U^*, \quad (4-54)$$

$$F^+ = J_2^+ U^*, \quad (4-55)$$

$$F^- = J_2^- U^*, \quad (4-56)$$

and Equation (4-28) is given by:

$$\frac{\partial U}{\partial t} + \frac{\partial E^+}{\partial x} + \frac{\partial E^-}{\partial x} + \frac{\partial F^+}{\partial y} + \frac{\partial F^-}{\partial y} + H = S \quad (4-57)$$

### 4.5 Time Integration

Following the special integration of the numerical fluxes and the source terms, Equation (4-37) can be rewritten in the following form for the  $I^{\text{th}}$  cell:

$$\frac{\partial \tilde{U}_I}{\partial t} = \mathfrak{R}(\tilde{U}_I) \quad (4-58)$$

where  $\mathfrak{R}$  is the residual of the cell  $I$ . The LPCE is a linearized system of equations; hence a fourth-order Runge-Kutta (RK4) method can be utilized to explicitly integrate the solution vector in time [86]:

$$\tilde{U}_I^1 = \tilde{U}_I^n + \left(\frac{\Delta t}{4}\right) \mathfrak{R}(\tilde{U}_I^n) \quad (4-59)$$

$$\tilde{U}_I^2 = \tilde{U}_I^n + \left(\frac{\Delta t}{3}\right) \mathfrak{R}(\tilde{U}_I^1) \quad (4-60)$$

$$\tilde{U}_I^3 = \tilde{U}_I^n + \left(\frac{\Delta t}{2}\right) \mathfrak{R}(\tilde{U}_I^2) \quad (4-61)$$

$$\tilde{U}_I^{n+1} = \tilde{U}_I^n + \Delta t \mathfrak{R}(\tilde{U}_I^3) \quad (4-62)$$

In Equations (4-59) to (4-62)  $\Delta t$  is a time step size that satisfies the Courant-Friedrichs-Lewy (CFL) criterion. The effect of the kernel type and the size of the radius of the kernel on stability of RK4 were studied by Nogueira et al. [86].

### 4.6 Boundary Condition Treatment

Figure 4.3 illustrate two types of boundary conditions that can occur in an acoustic simulation, namely non-reflective (or absorbing) boundary conditions, and perfectly reflective boundary conditions. This section describes the methods with which the aforementioned boundary conditions are implemented in the current acoustic solver.

#### 4.6.1 Non-Reflective (Absorbing) Boundary Conditions

Solution of a partial differential equation can be obtained when the boundary conditions are known. In numerical simulations of the external flows, solution domain consists of a region of interest and the far field. It is desirable to truncate the far field at a sufficiently far enough distance from the region of interest. However, the physical

boundary conditions on the truncated boundaries are usually unknown. High order numerical methods are designed with minimum dissipation. Therefore, the outgoing solutions are not damped at the truncated boundaries. Lack of suitable boundary condition can result in the reflection of spurious waves back into the solution domain and corruption of the computations in the region of interest [71]. Hence, development of non-reflective boundary conditions has been an active field of computational aeroacoustics. Some of the available methods are the characteristic based methods [87], radiation boundary condition [88], grid stretching and simultaneous filtering [89, 90], sponge layer [91, 92], and perfectly matched layers [93].

Sponge layers are simple to design and they can efficiently damp the acoustic variables into a known reference solution [92]. In the current acoustic solver, open physical domains are modeled using a sponge zone. Therefore, simulation domains with truncated boundaries are divided into two sub-domains (Figure 4.3) namely: the region of interest, and sponge zone (buffer). In the region of interest the acoustic solver solves the LPCE equation to model acoustic wave propagation. At the sponge zone the following modified LPCE is solved:

$$\frac{\partial \hat{\rho}}{\partial t} + u_{0j} \frac{\partial \hat{\rho}}{\partial x_j} + \rho_0 \frac{\partial \hat{u}_j}{\partial x_j} = \sigma(x_j)(\hat{\rho}_{ref} - \hat{\rho}) \quad (4.63)$$

$$\rho_0 \frac{\partial \hat{u}_j}{\partial t} + \rho_0 \frac{\partial(\hat{u}_i u_{0i})}{\partial x_j} + \frac{\partial \hat{p}}{\partial x_j} = \sigma(x_j)(\hat{u}_{ref} - \hat{u}) \quad (4.64)$$

$$\frac{\partial \hat{p}}{\partial t} + u_{0j} \frac{\partial \hat{p}}{\partial x_j} + \gamma p_0 \frac{\partial \hat{u}_j}{\partial x_j} + \hat{u}_j \frac{\partial p_0}{\partial x_j} = - \left( \frac{\partial p_0}{\partial t} + u_{0j} \frac{\partial p_0}{\partial x_j} \right) + \hat{s} + \sigma(x_j)(\hat{p}_{ref} - \hat{p}) \quad (4.65)$$

where  $\hat{\rho}_{ref}$ ,  $\hat{u}_{ref}$ ,  $\hat{p}_{ref}$ , and  $\sigma$  are the reference perturbed density, velocity, pressure and damping coefficient. The damping coefficient is designed such that the solution is damped gradually over the length of the sponge zone ( $l_{sp}$ ). Hence, damping coefficient at the beginning of the buffer zone is zero and it progressively increases and reaches to a full damping state. The incremental change the sponge strength over  $l_{sp}$  plays a key role in the design of the sponge layer. A sharp damping might result in the spurious wave

production at the truncated boundary. In addition, a thick sponge zone adds additional computational effort.

The sponge coefficient in the current acoustic solver at the  $j^{\text{th}}$  cell is:

$$\sigma(x_j) = \sigma_{max} \left( \frac{x_j - x_{s0}}{x_{smax} - x_{s0}} \right)^n \quad (4-66)$$

where  $\sigma_{max}$  is a real number,  $n$  is a positive integer, and  $x_{s0}$  and  $x_{smax}$  are the initial and end location of the sponge zone. Acoustic perturbations at the far field are assumed to be small and  $\hat{p}_{ref}$ ,  $\hat{u}_{ref}$ , and  $\hat{p}_{ref}$  can be set to zero at the sponge layer of the modified LPCE.

#### 4.6.2 Perfectly Reflective Boundary Conditions

This section describes the sharp interface GFM implementation of the perfectly reflective boundary condition. The idea of the GFM is the extension of the solution variables into a series of ghost cells located outside of the solution domain such that the desired boundary condition is satisfied on the immersed boundary. Following Seo et al. [78] Cartesian grids outside the acoustic domain that have at least one acoustic neighbor cell are tagged as ghost cells (Figure 4-4). An interfacial interception point  $x_{int}$  is found for each ghost cells at the point where the normal from the ghost cell to the interface intercept the immersed boundary. A MLS cloud is established around the  $x_{int}$  which encompass its corresponding ghost cell and the grid points inside the solution domain. These cloud points are used to set up a weighted least square problem in the form of Equation (3-17). Once the shape function is known, it is simple to assign appropriate values to the ghost points based on the desired boundary condition.

A perfectly reflective boundary condition for the perturbed velocities is satisfied by imposing a slip boundary conditions at the immersed boundaries. The slip boundary condition is implemented by applying the Neumann condition on the tangential component of the velocity vectors and the no-penetration condition for the normal

component of the velocity vectors. Moreover, Neumann boundary condition is used for the perturbed density and pressure. The appropriate value of the ghost cell for Dirichlet boundary condition is formulated for an arbitrary field  $\varphi$  in the following form:

$$\varphi_g = \frac{(\varphi_w - \sum_{i=1, i \neq ig}^n N(1,i) \varphi(x_{rel}^{int}))}{N(1,ig)} \quad (4-67)$$

and for the Neumann boundary condition the value of the ghost  $\varphi_g$  is:

$$\varphi_g = \frac{(\frac{\partial \varphi_w}{\partial n} - \sum_{i=1, i \neq ig}^n \mathbf{n} \cdot (N(2,i)\mathbf{i} + N(3,i)\mathbf{j})) \varphi(x_{rel}^{int})}{n \cdot (N(2,ig)\mathbf{i} + N(3,ig)\mathbf{j})} \quad (4-68)$$

where  $ig$  is the index number of the ghost cell in the cloud, and  $\varphi_w$  and  $\frac{\partial \varphi_w}{\partial n}$  are known boundary conditions at  $x_{int}$ .

#### 4.7 Filtering

It is known that high order methods experience numerical instabilities near the boundaries and the regions with non-uniform mesh [71]. This issue has been reported for the simulations with high order Compact scheme [94] and dispersion-relation-preserving (DPR) scheme in IBM framework [95]. These instabilities can propagate into the solution domain and degrade the accuracy of the method. The same issue has been observed when the current FVMLS solver was used near the interfacial boundaries.

To address this problem, several choices arise. Sun et al. [95] extended their simulations into the solid field and solved the governing equations for a non-physical acoustic field at this region. Subsequently, the incoming waves into the solid field were completely absorbed using PML absorbing zone. Seo et al. [78] employed a low order spatial filter near the immersed boundaries to filter the high wave number modes.

MLS has an intrinsic low-pass filtering property that can be utilized to address this problem. The MLS filter for an arbitrary field  $\varphi$  can be constructed using the MLS shape functions:

$$\bar{\varphi}(\mathbf{x}) = \sum_{i=1}^n N_i(\mathbf{x}) \varphi_i(\mathbf{x}) \quad (4-69)$$

where  $\bar{\varphi}$  is the filtered field. The filter can be constructed using the same MLSFV kernel or a different kernel with more dissipative characteristics. Additionally, the effect of the MLS filter increases as the size of the compact support of the kernel increases. It should be noticed that the filtering must be performed progressively near the interfaces to avoid numerical instabilities that a sudden dissipation of a wide range of wavelengths can create.

If the grids are structured, a second option is to apply a low-order spatial compact filter near the boundaries. The spatial compact filter is a one dimensional filter; hence, for a multi-dimensional problem, the filter needs to be applied in all directions sequentially. Consider an eleven point stencil shown in Figure 4.5. The filter formula for the cell  $i$  away from the boundaries is:

$$\alpha_f \bar{\varphi}_{i-1} + \bar{\varphi}_i + \alpha_f \bar{\varphi}_{i+1} = \sum_{n=0}^5 \frac{a_n}{2} (\varphi_{i+n} + \varphi_{i-n}) \quad (4-70)$$

where  $\alpha_f$  is the free parameter of the filter that satisfies  $-0.5 < \alpha_f < 0.5$ . For the near boundary cells, the lower order spatial filter formula is given by:

$$\bar{\varphi}_1 + \alpha_f \bar{\varphi}_2 = \sum_{n=1}^{11} a_n \varphi_n, \quad i = 1 \quad (4-71)$$

$$\alpha_f \bar{\varphi}_{i-1} + \bar{\varphi}_i + \alpha_f \bar{\varphi}_{i+1} = \sum_{n=1}^{11} a_n \varphi_n, \quad i \in \{2, \dots, 5\} \quad (4-72)$$

$$\alpha_f \bar{\varphi}_{i-1} + \bar{\varphi}_i + \alpha_f \bar{\varphi}_{i+1} = \sum_{n=0}^{10} a_{N-n} \varphi_{N-n}, \quad i \in \{N-4, \dots, N-1\} \quad (4-73)$$

$$\alpha_f \bar{\varphi}_{N-1} + \bar{\varphi}_N = \sum_{n=0}^{10} a_{N-n} \varphi_{N-n}, \quad i = N \quad (4-74)$$

The coefficients of the filter  $a_n$  are presented in Table 4- and Table 4-2 for the interior and boundary cells respectively. Solution of the spatial filter is obtained by solving a system of linear equations:

$$\mathbf{Ax} = \mathbf{b} \quad (4-75)$$

where  $\mathbf{A}$  is the matrix of the coefficients,  $\mathbf{x}$  is the solution vector of  $\bar{\varphi}$  components, and  $\mathbf{b}$  is the vector of the right hand side spatial filter.

#### 4.8 Validation of the FVMLS Solver

In this section computational capability of the FVMLS acoustic solver is examined through simulations of several bench-mark problems. The simulations are dimensionless. The length scale, velocity scale, time scale, density scale, and pressure scale for these simulations are  $\Delta x, c, \Delta x/c, \rho_0,$  and  $\rho_0 c^2$ .

##### 4.8.1 Propagation of a Gaussian Pressure Pulse

The first bench mark problem is the propagation of a Gaussian pressure pulse. The simulation is performed in a circular domain with its center placed at  $(x,y) = (100,100)$  and a radius of 90. A sponge zone is activated after the solution domain to damp the outgoing waves. The simulations starts with an initial Gaussian pressure pulse located at the center of the computational domain. The initial pressure pulse is given by Equation (4-76):

$$\dot{p} = \exp\left(-\ln(2) \frac{(x-100)^2 + (y-100)^2}{25}\right) \quad (4-76)$$

while the initial perturbed velocities and density are set to zero. The incompressible velocities are zero,  $\rho_0 = 1,$  and  $p_0 = 1/\gamma$ . The computational domain is discretized with a uniform Cartesian grid with  $\Delta x = \Delta y = 0.5$  and the time step size is  $\Delta t = 0.2$ . A third order FVMLS method is used for the simulation.

Figure 4.6 illustrate contours of the dimensionless perturbed pressure at  $t = 25, 50, 75,$  and  $100$ . Moreover, the dimensionless perturbed velocities at  $t = 25,$  and  $t = 50$  are depicted in Figure 4-7. The initial perturbed pressure propagates toward the truncated boundary at the edge of the region of the interest (the circular zone). When the outgoing solution passes the circular zone, the sponge layer is activated and progressively damps the solution toward the zero reference state. In Figure 4.6 it can be seen that small spurious waves are still created at the end of the sponge zone. However, they are completely dissipated in the sponge layer as they are passing the sponge zone back toward the initial side of the sponge layer.

Analytical solution of this problem is given in Ref. [96]. The computational perturbed pressure and analytical solution are compared on the line  $y = 100$  in Figure 4-8 at  $t = 25$  and  $t = 50$ . It is observed that the computational results and analytical solution are in good agreement.

#### 4.8.2 Radiation of a Pulsatile Monopole in a Uniform Mean Flow

In the previous test case, the incompressible flow field was assumed to be quiescent and acoustic source was imposed as an initial condition. In many applications such as the human larynx, acoustic propagation occurs in the presence of an incompressible flow. Moreover, the acoustic source might change with time. In this section a pulsatile monopole is modeled in a uniform incompressible flow with  $M_x = 0.5$ . The simulation is performed in a circular solution domain with a radius of 100. The center of the circular domain is placed at  $(x,y) = (120,120)$  and a sponge layer is designed outside the solution domain. The pulsatile source term, which is located at  $(x,y) = (120,120)$ , is given by:

$$\dot{p} = \frac{1}{2} \exp\left(-\ln(2) \frac{(x-120)^2 + (y-120)^2}{2}\right) \sin(\omega t) \quad (4-77)$$

where  $\omega = 2\pi/30$ , and  $t$  is the dimensionless time. The  $\dot{p}$ ,  $\dot{u}$ , and  $\dot{v}$  are initially zero. Moreover,  $\rho_0 = 1.0$ ,  $u_0 = 0.5$ , and  $v_0 = 0.0$ . The computational domain is discretized with a uniform Cartesian grid  $\Delta x = \Delta y = 0.25$ . The time step size of the simulation is  $\Delta t = 0.1$ . A third order FVMLS method is used for the simulation.

Figure 4-9 shows the dimensionless perturbed pressure contours at  $t = 90, 150, 210,$  and  $270$ . The results show that the acoustic waves are traveling with different velocities in the upstream and downstream of the solution domain. The pressure contours are in good agreement with previous simulations reported in the literature with other high order methods [85, 89, 97]. The analytical solution of this problem is given in Ref. [97]. Figure 4-10 compares the resolution of the current FVMLS against the

analytical solution on  $y = 120$  and  $t = 270$ . As can be seen, the FVMLS is able to accurately predict the propagation of acoustic waves. It is observed in Figure 4-9 that the outgoing waves, especially on the right hand side of the solution domain, were exposed to the truncated boundaries for a long period of the simulation. However, the sponge layer efficiently absorbed the outgoing solution. The efficiency of the sponge layer is more evident in Figure 4-10 when the excellent agreement is observed between the analytical and FVMLS solver results at the edge of the solution domain.

#### 4.8.3 Propagation of a Wall-Bounded Acoustic Pulse in a Uniform Mean Flow

Many engineering applications of computational aeroacoustic deal with wall bounded problems. A perfectly reflective boundary condition is required for correct simulation of the acoustic field near the wall boundaries. In this section the effectiveness of the perfectly reflective boundary condition of the current FVMLS solver is examined.

This test case is taken from [85, 89, 98] and includes propagation of a Gaussian pressure pulse in a duct with a uniform mean flow of  $u_0 = 0.5$  and  $v_0 = 0.0$ . The pressure pulse is:

$$\dot{p} = \exp\left(-\ln(2)\frac{(x+50)^2+y^2}{36}\right), \quad (4-78)$$

and the perturbed density and velocities have zero initial condition. Moreover,  $\rho_0 = 1.0$  and Mach number is 0.5. The computational domain is rectangular with  $-120 < x < 120$  and  $-50 < y < 50$  and is discretized with a uniform Cartesian grid with  $\Delta x = \Delta y = 0.5$ . The non-dimensional time step size for this simulation is  $\Delta t = 0.2$ . The duct walls in this test case are immersed in the Cartesian grids and represented by two level set fields. On wall boundaries, a perfectly reflective boundary condition is imposed which satisfies the slip boundary condition for the perturbed velocities and Neumann boundary condition for the perturbed pressure. Furthermore, a sponge layer is designed at the inlet and out let of the duct to damp the outgoing acoustic waves. The initial location of the sponge zone

is shown in the figures with a black line. A third order FVMLS method is used for the simulation.

Figure 4-11 compares the dimensionless perturbed pressure field obtained with the current solver and the simulation results provided in Ref. [89]. The results in Ref [89] were obtained using an implicit solver based on a sixth-order centered compact scheme for spatial discretization and a fourth-order Runge-Kutta method for the temporal integration. The pressure pulse propagates in all direction with different speed due to the presence of the mean incompressible velocity. After the pulse reached the wall boundaries, it reflects to the center of the duct. The results in Figure 4-11(a) match very well with the result of [85, 89] in Figure 4-11(b) with same contour levels.

#### 4.8.4 Acoustic Wave Propagation from a Circular Cylinder

In many practical applications geometries are not flat. Moreover, the spurious waves generated due to imposing the perfectly reflecting boundary condition at the immersed interfaces are stronger near the curved boundaries. Therefore, adequate filtering near curved boundaries is required. In this section the perfectly reflecting boundary condition will be tested for a circular immersed boundary. The test case is taken from [99]. This test case has also been modeled in the literature as the validation [78, 95, 100].

The test case includes the propagation of a Gaussian pressure pulse in a quiescent incompressible flow field. A circular cylinder with the radius 0.5 is located at  $(x,y) = (0,0)$ . The Gaussian pressure pulse is given by:

$$\dot{p} = \exp\left(-\ln(2)\frac{(x-4)^2+y^2}{0.04}\right), \quad (4-78)$$

and is placed at  $(x,y) = (4,0)$ . The initial perturbed density and velocities are zero. Moreover,  $\rho_0 = 1.0$ , and  $p_0 = 1/\gamma$ . The simulation is performed in a circular domain with a radius of 14. The center of the circular domain is placed at  $(x,y) = (0, 0)$  and a sponge layer is designed outside the solution domain. The computational domain is

discretized with  $\Delta x = \Delta y = 0.015$ . The time step size for this simulation is  $\Delta t = 0.02$ . A third order FVMLS method is used for the simulation. A schematic view of the current test-case is shown in figure Figure 4-12.

Contours of the dimensionless perturbed pressure at  $t = 2, 4, 6$ , and  $8$  are shown in Figure 4-13. As the initial pressure pulse reaches the circular cylinder, the perturbed pressure wave is reflected from the cylinder and moves in the opposite direction of the propagation of the initial pressure pulse. The perturbed pressure contours are in good agreement with the previous literature [78, 95]. Analytical solution of this benchmark problem is available at [99]. Time history of the perturbed pressure at four points of a, b, c, and d (Figure 4-12) are compared with the analytical solution in Figure 4-14. The simulation results obtained with the current acoustic solver are in good agreement with the exact solution.

Table 4-1 Spatial compact filter coefficients for the interior cells.

$a_0$	$a_1$	$a_2$	$a_3$	$a_4$	$a_5$
$\frac{193 + 126\alpha_f}{256}$	$\frac{105 + 302\alpha_f}{256}$	$\frac{-15 + 30\alpha_f}{64}$	$\frac{45 - 90\alpha_f}{512}$	$\frac{-5 + 10\alpha_f}{256}$	$\frac{1 - 2\alpha_f}{512}$

Table 4-2 Spatial compact filter coefficients for boundary cells.

	$a_1$	$a_2$	$a_3$	$a_4$	$a_5$	$a_6$	$a_7$	$a_8$	$a_9$	$a_{10}$	$a_{11}$
Point 1	$\frac{3+\alpha_f}{4}$	$\frac{1+\alpha_f}{2}$	$\frac{-1+\alpha_f}{4}$	0	0	0	0	0	0	0	0
Point 2	$\frac{1+14\alpha_f}{16}$	$\frac{3+2\alpha_f}{4}$	$\frac{3+2\alpha_f}{8}$	$\frac{-1+2\alpha_f}{4}$	$\frac{1-2\alpha_f}{16}$	0	0	0	0	0	0
Point 3	$\frac{-1+2\alpha_f}{64}$	$\frac{3+26\alpha_f}{32}$	$\frac{49+30\alpha_f}{64}$	$\frac{5+6\alpha_f}{16}$	$\frac{-15+30\alpha_f}{64}$	$\frac{3-6\alpha_f}{32}$	$\frac{-1+2\alpha_f}{64}$	0	0	0	0
Point 4	$\frac{1-2\alpha_f}{256}$	$\frac{-1+2\alpha_f}{32}$	$\frac{7+50\alpha_f}{64}$	$\frac{25+14\alpha_f}{32}$	$\frac{35+58\alpha_f}{128}$	$\frac{-7+14\alpha_f}{32}$	$\frac{7-14\alpha_f}{64}$	$\frac{-1+2\alpha_f}{32}$	$\frac{1-2\alpha_f}{256}$	0	0
Point 5	$\frac{-1+2\alpha_f}{1024}$	$\frac{5-10\alpha_f}{512}$	$\frac{-45+90\alpha_f}{1024}$	$\frac{15+98\alpha_f}{128}$	$\frac{407+210\alpha_f}{512}$	$\frac{63+130\alpha_f}{256}$	$\frac{-105+210\alpha_f}{512}$	$\frac{15-30\alpha_f}{128}$	$\frac{-45+90\alpha_f}{1024}$	$\frac{5-10\alpha_f}{512}$	$\frac{-1+2\alpha_f}{1024}$

Note: For the cells N to N-4 the coefficients are  $a_N = a_1$ ,  $a_{N-1} = a_2$ ,  $a_{N-2} = a_3$ ,  $a_{N-3} = a_4$ ,  $a_{N-4} = a_5$ ,  $a_{N-5} = a_6$ ,  $a_{N-6} = a_7$ ,  $a_{N-7} = a_8$ ,  $a_{N-8} = a_9$ ,  $a_{N-9} = a_{10}$ , and  $a_{N-10} = a_{11}$ .

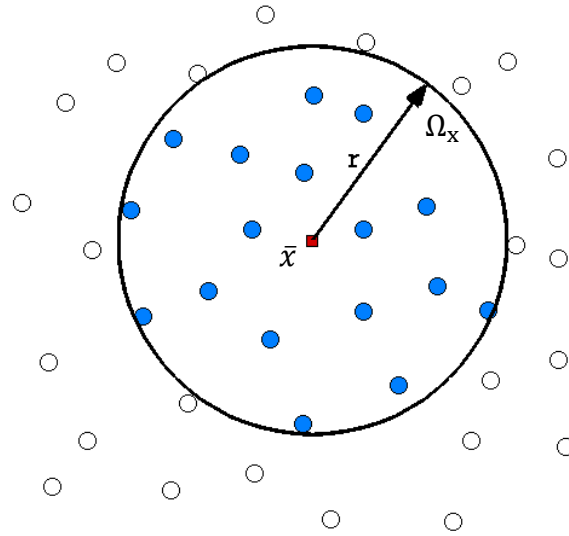


Figure 4-1 A schematic view of the MLS cloud for non-uniform data points.

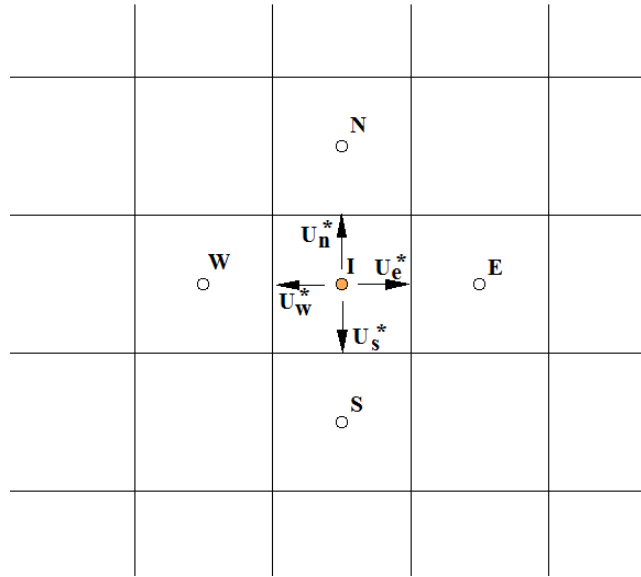


Figure 4-2 A finite-volume Cartesian cell and the cell face fluxes.

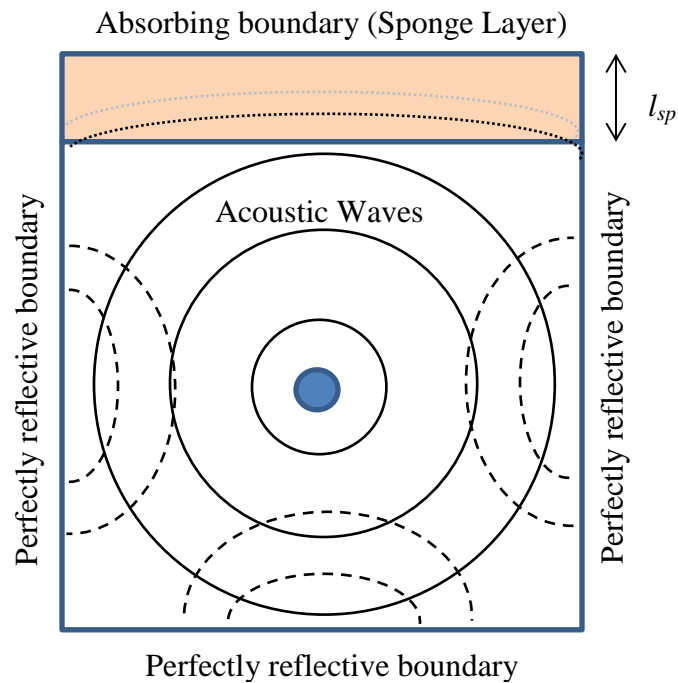


Figure 4.3 A schematic view of the boundary conditions in an acoustic problem. Non-reflective boundaries absorb and damp the outgoing waves and reflective boundaries reflect the acoustic waves back into the solution domain.

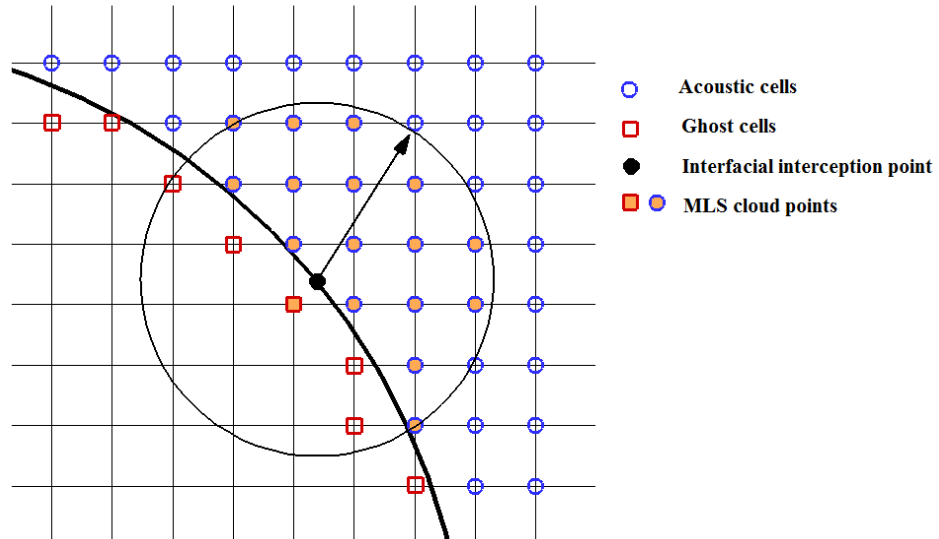


Figure 4-4 A representation of GFM and MLS cloud for an arbitrary ghost cell used in the FVMLS acoustic solver on the Cartesian grids.

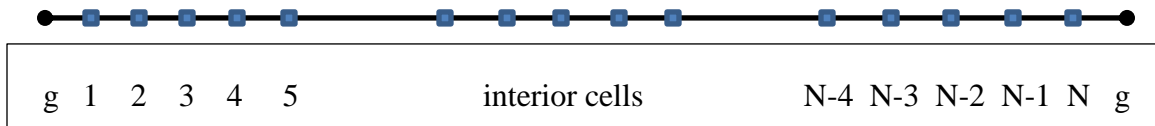


Figure 4.5 Notation of a one-dimensional spatial filter

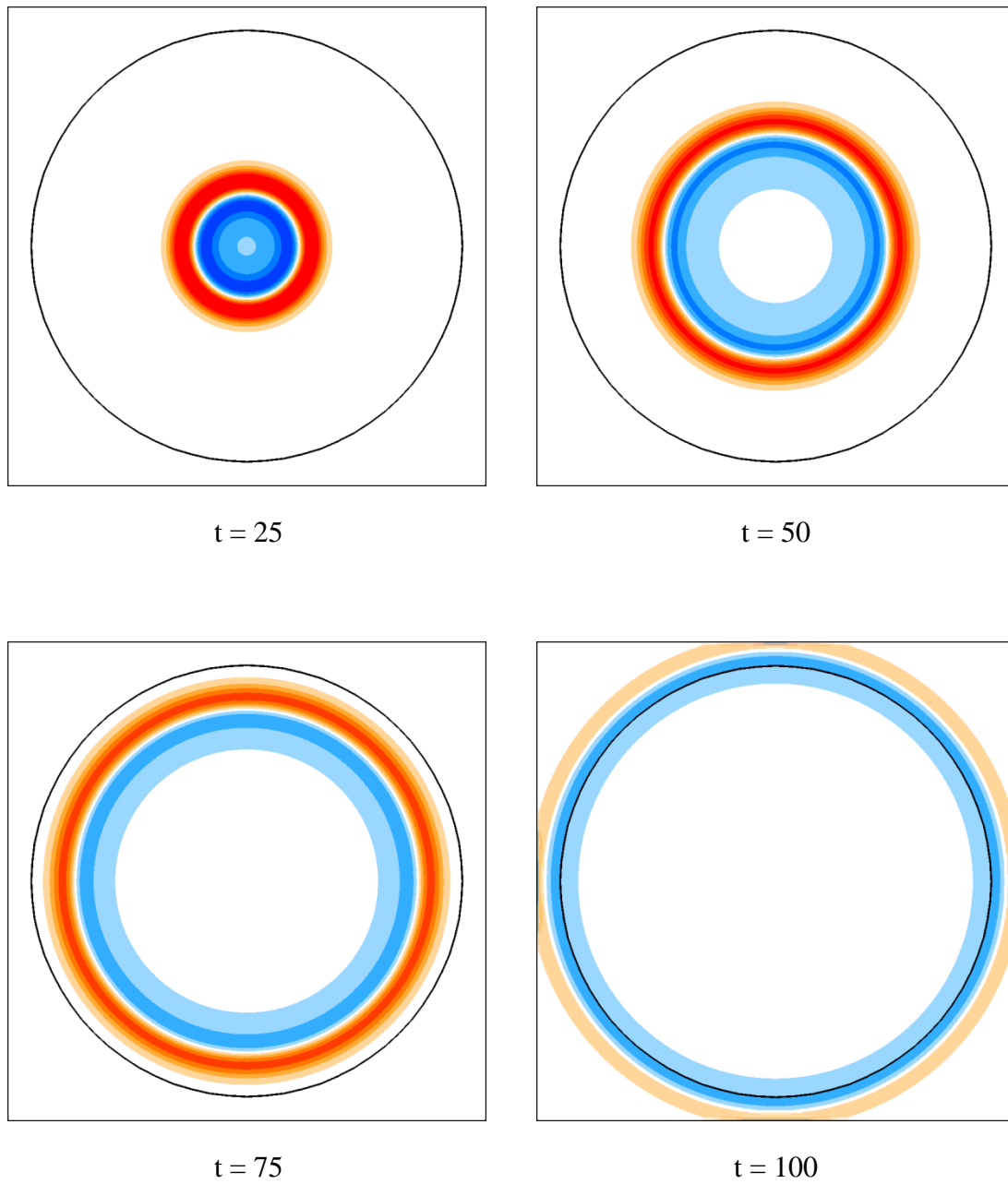


Figure 4.6 Contours of non-dimensional perturbed pressure at  $t = 25, 50, 75,$  and  $100$ . The contours have 10 levels between  $-0.1$  and  $0.1$ . The sponge layer is located outside of the circle. The black circle shows the beginning of the sponge zone.

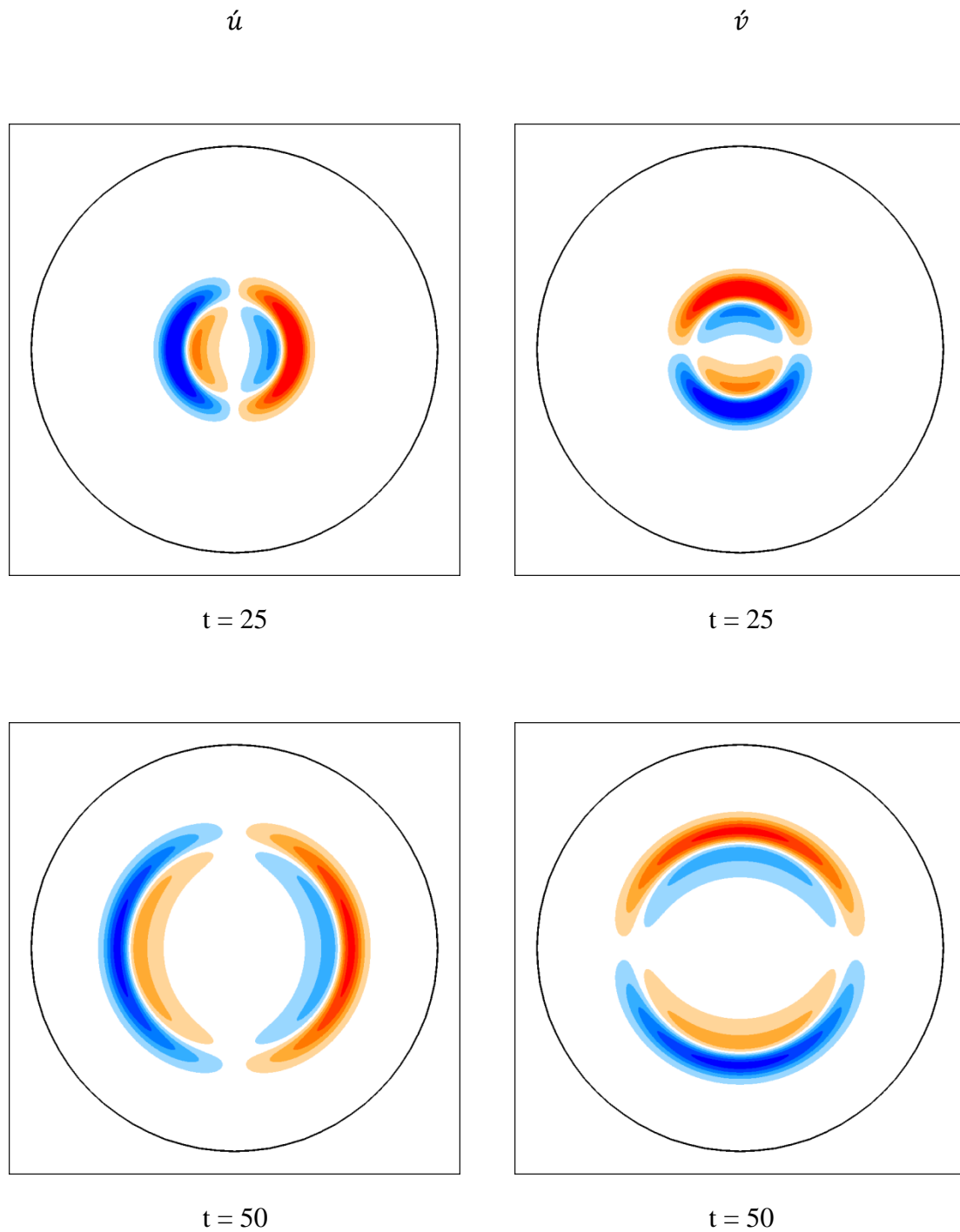


Figure 4-7 Contours of non-dimensional perturbed velocities at  $t = 25$ , and  $50$ . The contours have 10 levels between  $-0.1$  and  $0.1$ . The sponge layer is located outside of the circular zone. The black circle shows the beginning of the sponge zone.

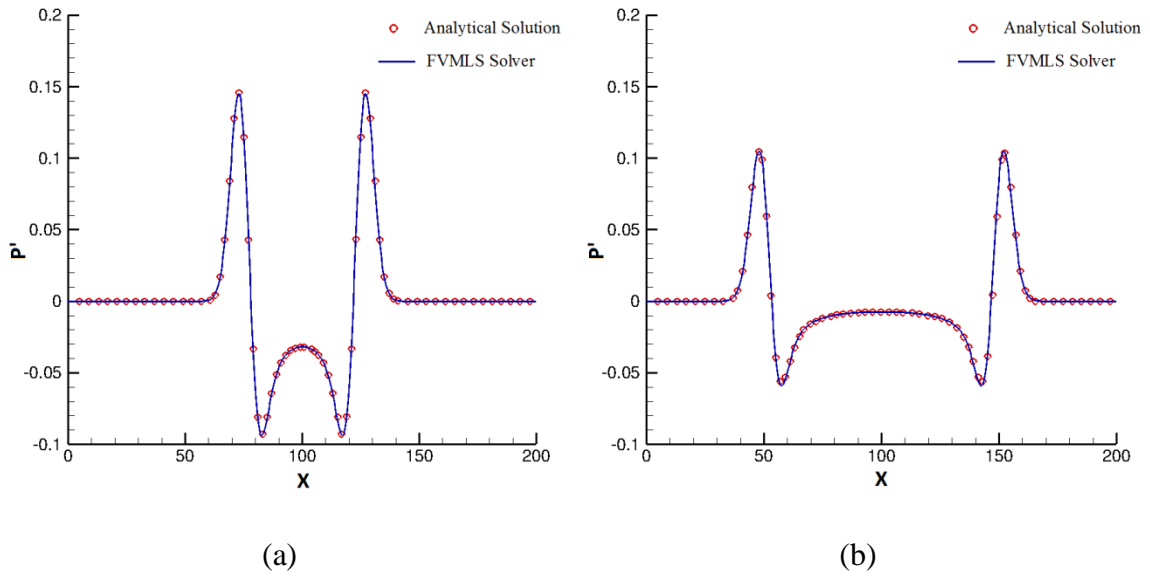


Figure 4-8 Comparison between the non-dimensional computational perturbed pressure using the current FVMLS solver and analytical solutions of the Gaussian pressure pulse on the line  $y = 100$  at (a)  $t = 25$  and (b)  $t = 50$ .

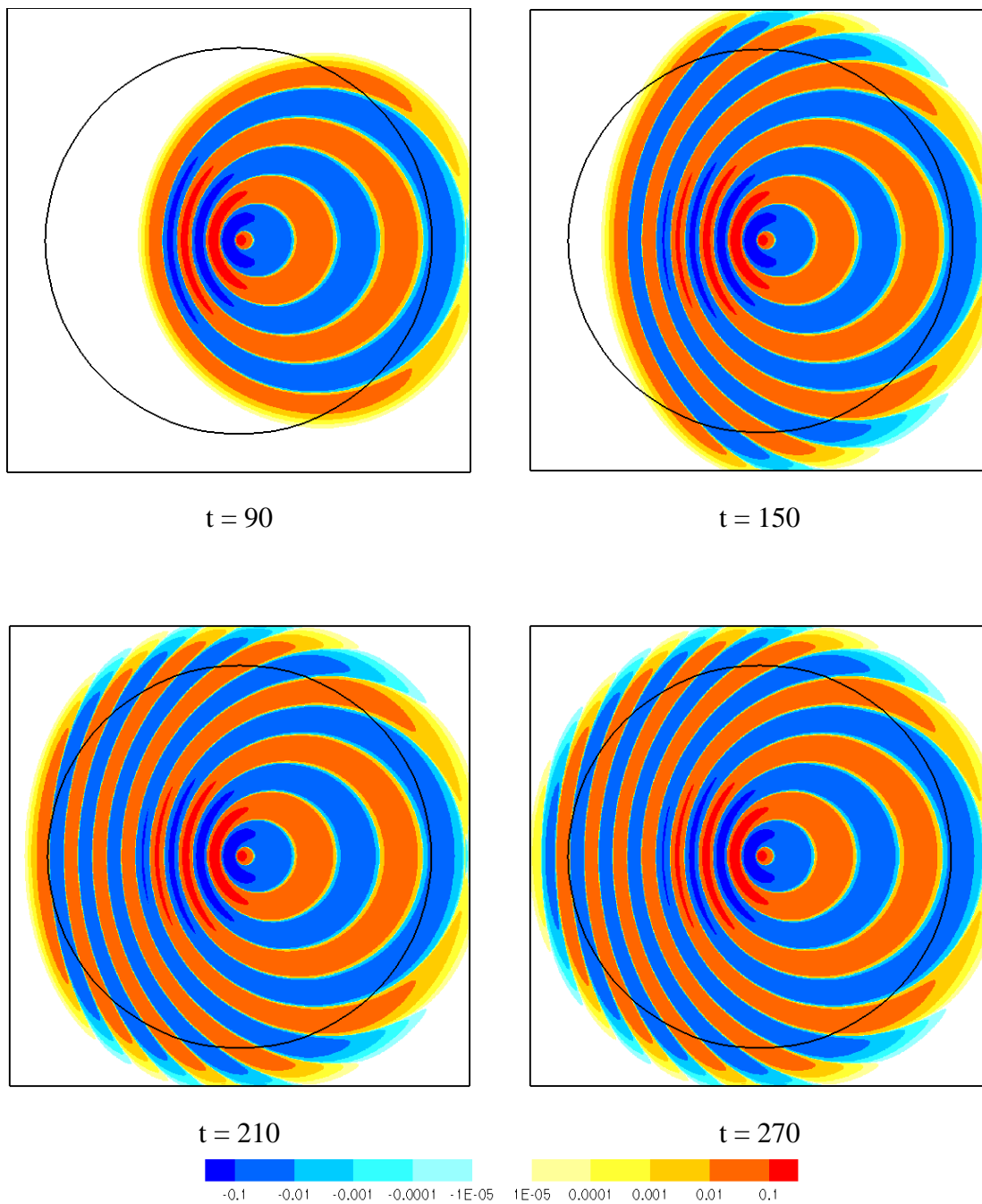


Figure 4-9 Contours of the perturbed pressure of a pulsatile monopole at  $t = 90, 150, 210,$  and  $270$ . The sponge layer is located outside of the circular zone. The black circle shows the beginning of the sponge zone.

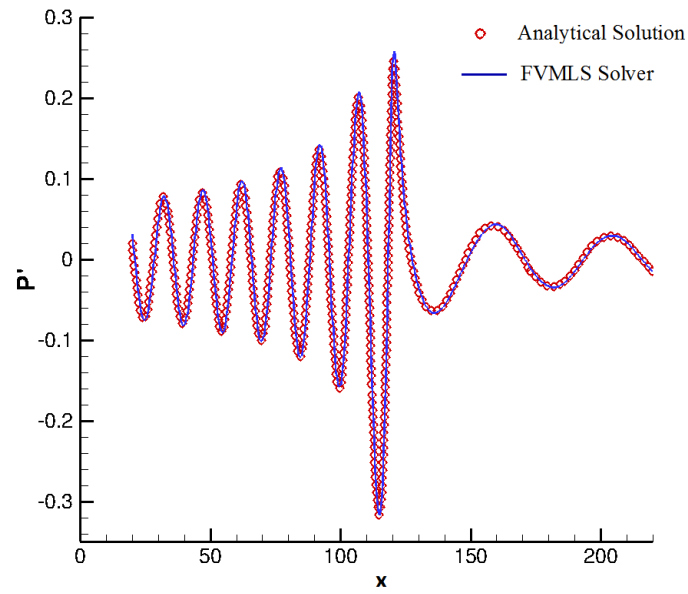


Figure 4-10 Comparison between the non-dimensional computational perturbed pressure calculated using the current FVMLS solver and the analytical solutions of the pulsatile monopole ( $M=0.5$ ) on the line  $y = 120$  and  $t = 270$ .

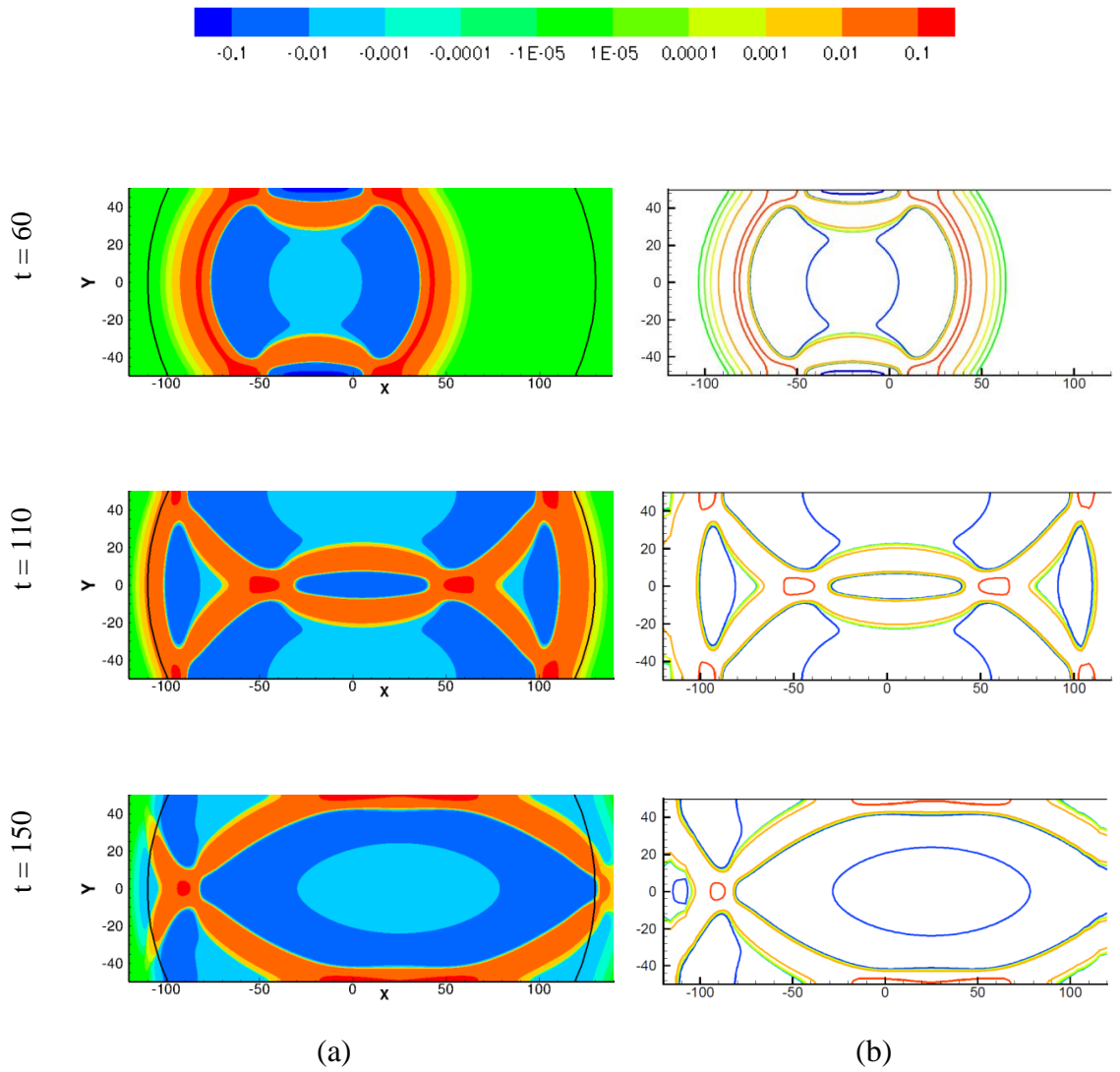


Figure 4-11 Contours of the non-dimensional perturbed pressure of a wall-bounded Gaussian pressure pulse in a uniform mean flow ( $M=0.5$ ). MLSFV solver (right), 6<sup>th</sup> order finite difference compact method [89] (left) The black circle shows the beginning of the sponge zone.

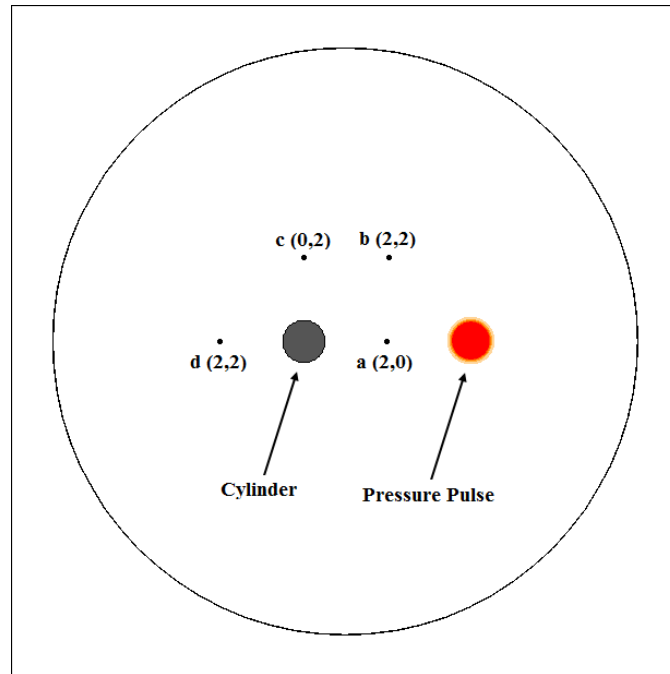


Figure 4-12 A schematic view of the test case problem: acoustic wave propagation from a circular cylinder.

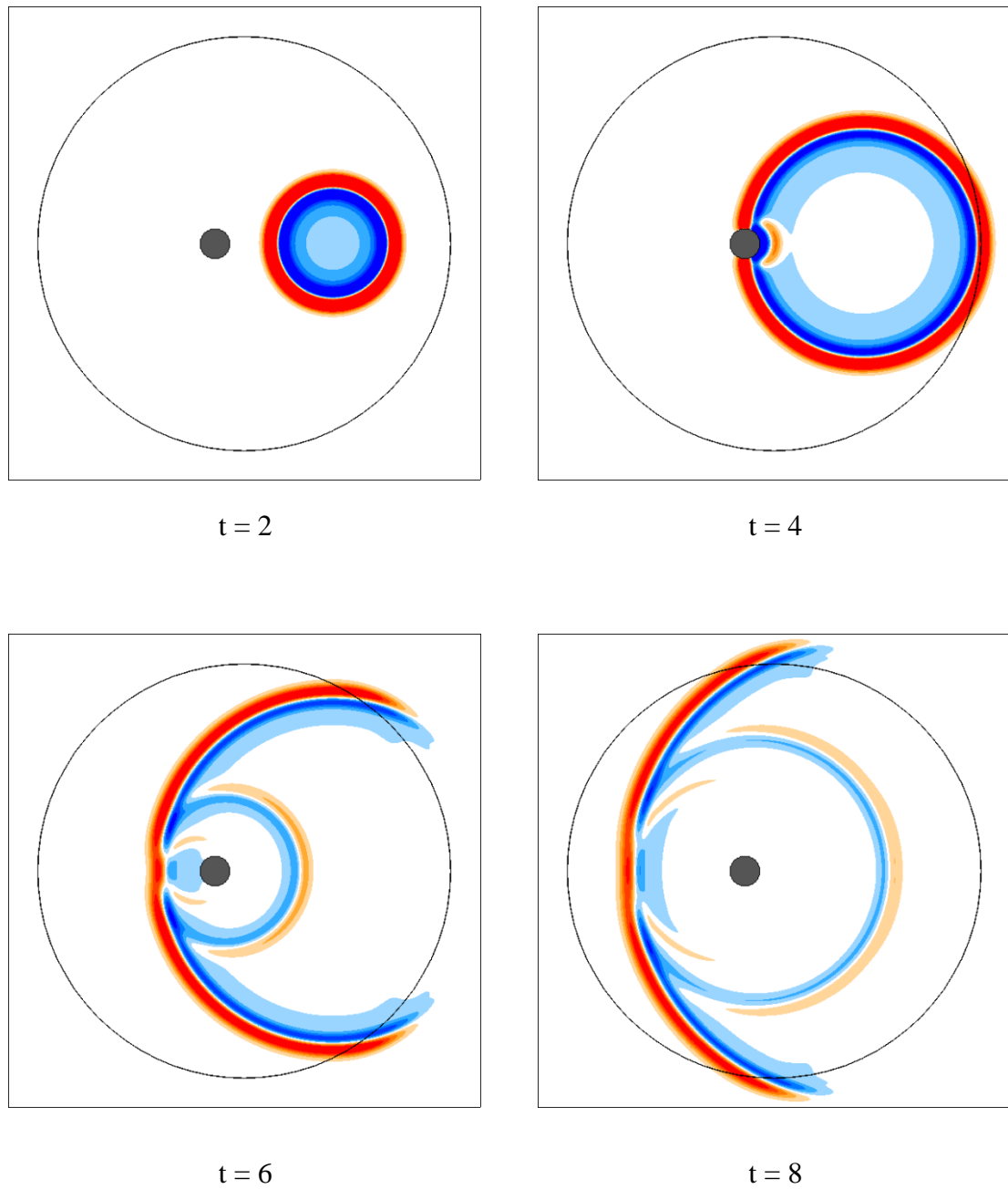


Figure 4-13 Contours on non-dimensional perturbed pressure at  $t = 2, 4, 6,$  and  $8$ . The contours have 10 levels between  $-0.1$  and  $0.1$ . The black circle shows the beginning of the sponge zone.

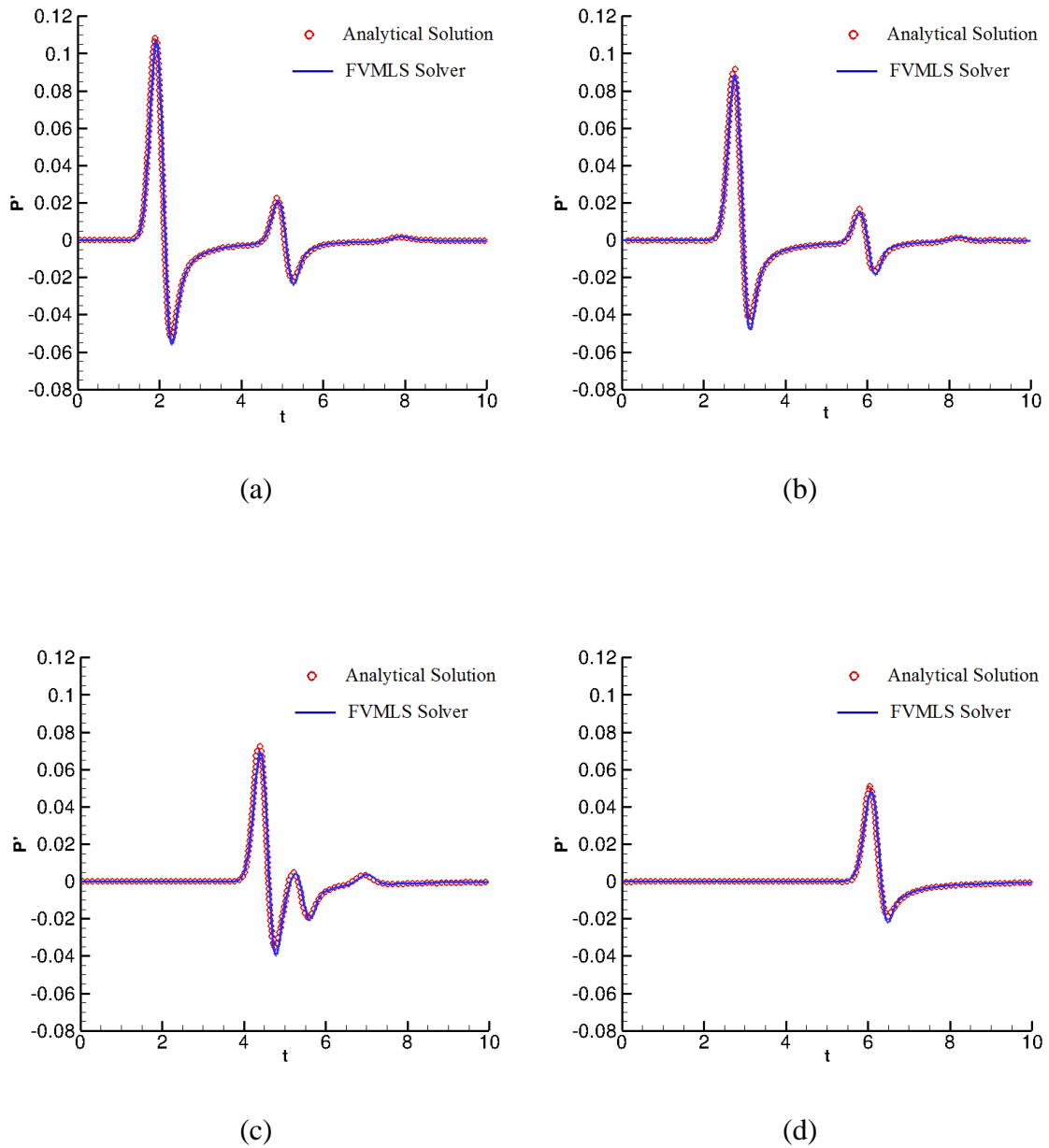


Figure 4-14 Comparison between the time history of the dimensionless computational perturbed pressure calculated using the current FVMLS solver and the analytical solutions of acoustic wave propagation from a circular cylinder at points a, b, c, and d.

## CHAPTER 5

### THE EFFECT OF FALSE VOCAL FOLDS GEOMETRY ON GLOTTAL FLOW

#### 5.1 Introduction

In each cycle of phonation an unsteady glottal jet flow is created. This jet flow and acoustic waves move through the supraglottic region and are modified in the upper respiratory tract. The FVFs are the first obstructions located above the glottis. It is hypothesized that this pair of tissue can affect the glottal flow and/or the acoustic output of the larynx during phonation. This hypothesis is tested both computationally and experimentally in this chapter. The experiments were performed in the low speed wind tunnel introduced in chapter 2 and the computations were obtained using the incompressible solver discussed in chapter 3.

Three geometrical parameters that are investigated in this chapter are: the size of the false vocal fold gap ( $G_{fvf}$ ), the height between the true and false vocal folds ( $H_{fvf}$ ), and the width of the laryngeal ventricle ( $W_{lv}$ ). The main focus is to understand the effects of variation of these parameters on dynamics of the glottal flow and pressure distribution on the surface of the larynx. The pressure distribution is studied both computationally and experimentally. Moreover, computational simulations are used to investigate glottal flow structures. The link between pressure distribution on the surface of the larynx and variation of the FVFs geometry is discussed in the context of vortex evolution in the supraglottal region.

#### 5.2 Classification of the Laryngeal Models

Seven static and rigid laryngeal models were used for the experimental investigations. The computational simulations were performed on the same laryngeal geometries plus two additional laryngeal models which were also designed using the laryngeal equations of Nomura et al. [53]. The TVFs of these models were parallel and

the glottis was  $1\text{mm}$  wide. The sizes of the  $G_{\text{fvf}}$ ,  $H_{\text{fvf}}$ , and  $W_{\text{lv}}$  for the models used in the current study are reported in Table 5-1.

In Table 5-1, C1 is the control model which was designed according to the mean values of the measurements of the human larynx [20]. The rest of the laryngeal models were organized into three groups. In each group only one geometrical parameter were changed in the physiological range reported by Agarwal et al. [20]. The first category is the “G” group in which the laryngeal models have different  $G_{\text{fvf}}$  compared to the control model. The second category is the “H” group for which the size of  $H_{\text{fvf}}$  is different. The third category is the “L” group where the laryngeal models have different  $W_{\text{lv}}$ .

### 5.3 Grid Independent Study

Efficient mesh resolution in regions with vorticity and velocity gradients is of great importance for correct prediction of complex fluid dynamics phenomena including shear layer instabilities, growing boundary layers, and sophisticated vortex structures. In a recent study [15], the effect of near-wall grid refinement at the boundaries of the glottis on correct prediction of the characteristics of the glottal jet was highlighted in a series of three-dimensional simulations. They observed that their results with a fine (5,000,000 grid points) and a coarse (1,000,000 grid points) mesh, including near wall refinement were more consistent with the experimental measurements; whereas, the computational results with 3,000,000 grid points without near wall refinement demonstrated poor agreements with the experiments.

In order to achieve a highly accurate glottal flow simulation, it is also necessary to consider unsteady characteristics of the glottal jet. The flow unsteadiness and instabilities affect jet flapping in the downstream of the glottis. Therefore, adaptive grid refinement is also required at the shear layer of the glottal jet, and a uniform or stretched mesh at these regions is insufficient for a precise simulation of the glottal flow. This requirement was fulfilled in the simulations of this dissertation with the possibility of six levels of LMR.

A grid independence study was performed on C1 laryngeal model. For this purpose, two base Cartesian grid sizes of  $dx^* = 0.05$ , and  $dx^* = 0.0125$  were selected. A linear ramp was used to impose the inlet boundary condition whereby the velocity grew gradually for  $t^* = 0.108$  and then remained constant for the rest of the simulation. The maximum Reynolds number, based on the input diameter at the subglottal region and the maximum velocity after the velocity ramp, was 1000. A no-slip boundary condition was imposed on the larynx walls and the outlet boundary was treated with a convective outflow condition. The simulations were performed for a time of  $t^* = 0.304$ .

The simulation with a coarse grid began with approximately 112,000 grid points after the initial refinement. As the flow structures were developing, the number of the grid points continuously increased due to the adaptive refinement. The simulation terminated with about 900,000 grid points. The simulation with a fine grid initiated with 479,000 grid points and terminated with 6,432,500 grid points. These simulations were performed in parallel using 60 cores of the Helium high performance computing cluster at the University of Iowa. Figure 5-1 compares these two grids at a region near the FVF at  $t^* = 0.104$ .

The vorticity contours for the fine and coarse simulations are depicted in Figure 5-2. The overall vorticity pattern is nearly identical for the two cases before  $t^* = 0.176$ . After this time, jet flapping was observed in similar location for both simulations and vortices moved toward the same side of the vocal tract. Moreover, the behavior of the vorticity structures remained the same in the laryngeal ventricle during the whole period of the simulation. Since the focus of the current work is on the glottal flow in the laryngeal ventricle, the fact that the coarse and fine mesh predicts the same aerodynamics characteristics at this region justified the use of a grid size similar to the coarse grid for the rest of the simulations in this work.

#### 5.4 Comparison with previous investigation of the glottal flow

The glottal flow is pulsatile and its laminar core at the subglottal region can transition to turbulence and create a complex three-dimensional flow structures [11, 13, 101, 102]. The main characteristics of the glottal flow are:

1. Formation of a starting vortex (two counter-rotating vortices also known as a vortex dipole),
2. Creation of a trailing jet that follows the starting vortex,
3. Growth of shear layer instabilities
4. Flapping of the glottal jet flow at the supraglottal region,
5. Transition of laminar core of the glottal jet to turbulence [1, 16].

Although, the flow structures described in Section 5.3 were obtained using two-dimensional rigid models in the presence of a non-pulsatile inlet flow condition, the flow structures in the simulations exhibit the key features of the glottal flow.

The simulations in Figure 5-2 start with formation of a starting vortex. This vortex structure results from a shear layer roll-up charged by the jet flow from the glottis. The starting vortex then detaches from the surface of the TVFs and passes through the gap between the FVFs while being followed by a trailing jet. Formation of the starting vortex and its trailing jet were reported in other flow visualizations with rigid and flexible TVFs [11, 16, 18, 37]. The formation of this vortex structure (vortex rings in three-dimensions) has been reported in many other physiological fluid flows [19]. According to Gharib et al. [19] a limit exists for which the starting vortex acquires the maximum circulation and pinches-off from its trailing jet. This limit is defined by a universal non-dimensional number known as the formation number

$$F = \bar{U}T_d/d \quad (5-1)$$

where  $T_d$ , and  $d$  are the discharge time, and orifice diameter. For the laryngeal simulations,  $d$  is the  $G_{\text{ivf}}$  and  $\bar{U}$  is the mean value of the inlet velocity

$$\bar{U} = \left(1/T_d \int_0^{T_d} u_{\text{inlet}}(t) dt\right). \quad (5-2)$$

where  $u_{\text{inlet}}(t)$  is the linear velocity ramp. Formation number has been examined for a wide range of fluid flows and is commonly accepted that its value lies in the range between 3.6 and 4.5. The formation number of the starting vortex observed in the current simulations is approximately 3.8. Therefore, the simulation results are consistent with the known physical behavior of starting vortices [19].

Figure 5-2 shows that the interaction between the starting vortex and the FVFs, while it is passing through the gap between the FVFs, results in formation of a set of rebound vortex structures in the laryngeal ventricle. PIV measurements of the glottal flow using flexible and static models of the TVFs also demonstrated that the FVFs could interfere with the starting vortex and create vortices in this region [16, 18]. Impingement of the glottal jet on the FVFs was also observed in the computational simulations when the laryngeal flow was assumed symmetric [103]. The rebound vortices in Figure 5-2 detach the surface of the FVFs and move in the laryngeal ventricle toward the TVFs; however, they do not reach the TVFs during the simulation.

The trailing jet of the glottal flow in the supraglottal region beyond the FVFs in the computational simulations experiences a flapping motion consistent with previous studies on the glottal flow [11, 16]. This phenomenon occurs due to the growth of the Kelvin–Helmholtz instability in the shear layer of the jet flow [11, 104].

While several consecutive vibrations of the TVFs are required for human phonation, the goal of the current study is to examine the effect of the FVF geometry on vortical structures important to human phonation, with a focus on the starting vortex and its sensitivity to the FVF geometry. In spite of these simplifications, the flow structures observed in this section (formation of the starting vortex, creation of shear layer

instabilities in the trailing jet, and formation of the rebound vortices) are consistent with the vorticity patterns observed in each cycle of the phonation of the oscillatory models of the TVFs [11, 16]. Therefore, simplifications of the current study enable the performance of a parametric study of the effect of the FVF geometry on key features of the glottal flow.

### 5.5 The effect of the FVF gap on the glottal flow aerodynamics

In order to study the effect of  $G_{\text{FVF}}$  on the glottal flow, five laryngeal models (namely G1, G2, C1, G3, and G4) were investigated computationally for which  $G_{\text{FVF}}$  were 2.3, 3.3, 5.1, 6.3, and 7.5mm respectively. The Reynolds number of the simulations was 1000 and the boundary conditions applied to these simulations were similar to those described for performing the grid independent study.

The vorticity contours of these laryngeal models are compared in Figure 5-3. Moreover, streamline contour of G1, C1, and G4 are shown in Figure 5.4. In all cases, a starting vortex forms and convects toward the supraglottic region. Moreover, jet flapping occurs at the supraglottic region after the FVFs. The rebound vortices in G3 and G4 laryngeal models are weak and remain in the vicinity of the FVFs walls. The rebound vortices detach from the surface of the FVFs and convect toward the TVFs for the control model; however, they do not reach the TVFs during the simulation. The G1, G2 laryngeal models for which  $G_{\text{FVF}}$  were smaller than the  $G_{\text{FVF}}$  of the control model reveal a strong interaction between the starting vortex and the FVFs. Following the impingement of the starting vortex with the surface of the FVFs in these models, the resulting rebound vortices move toward the TVFs. The structure of each rebound vortex is also composed of two counter-rotating vortices followed by a trailing jet. These vortices collide with the shear layer of the glottal jet in the laryngeal ventricle. One of the counter-rotating vortices moves toward the TVFs and collides with its surface while the other counter-

rotating vortex filters into the FVF gap and creates a second set of rebound vortex structures. For G2 laryngeal model, these second rebound vortices move into the flow circulation at the laryngeal ventricle whereas these rebound vortices for G1 again collide with the shear layer of the trailing jet of the glottal flow and then reach the surface of the TVFs.

In order to investigate the oscillatory pattern of the vortex shedding from the surface of the TVFs, the Strouhal number ( $St = \frac{fd}{V}$ ) is provided for all cases (where  $f$ ,  $d$ , and  $V$  are the vortex shedding frequency,  $G_{\text{fvf}}$ , and average velocity at the glottis). The shedding frequency is calculated based on the time interval when the first two subsequent vortices in the trailing jet flow pass the same location just after the FVFs gap. The highest value of the Strouhal number is approximately 0.174 and is found for G1 and G2 models with small  $G_{\text{fvf}}$ . As the size of  $G_{\text{fvf}}$  increases, the value of the Strouhal number drops to 0.151, 0.157, and 0.156 for C1, G3, and G4 respectively. This trend indicates that the small size of the  $G_{\text{fvf}}$  would increase the ratio of the local flow velocity of the vortex shedding to the average flow of the glottal jet.

Kucinski et al. [37] also studied the relationship between the Strouhal number and the size of the FVF gap by comparing two  $G_{\text{fvf}}$  using experimental models in a wind tunnel. Their findings indicated that the Strouhal number was larger in the model with the wider  $G_{\text{fvf}}$ . However, their flow oscillations were measured in the ventricle region, resulting from vortex shedding from the separation of the glottal flow from a divergent glottis. Moreover, they did not report any vortical structures in the laryngeal ventricle. In our simulation, the TVFs are parallel, and the jet remains more intact up to the FVFs. The vortex shedding is more pronounced distal to the FVFs.

The balance between the viscoelastic force of the TVF tissues and the aerodynamic forces of the air flow creates the vibration of the TVFs. Successful lumped-element models such as the two-mass model of Steinecke et al. [65] employ the air pressure as the dominant aerodynamic force to capture self-sustained oscillation of the

vocal folds. Although the TVFs were rigid and stationary in our simulations, the non-dimensional differential pressure history ( $\Delta p^*$ ) on the surface of the TVFs, laryngeal ventricle, and FVFs is plotted in Figure 5-5 for G1, C1, and G4 (Plots of the non-dimensional differential pressure history for G2 and G3 models are omitted to provide better clarity, but show similar trends). The differential pressure in the current work is defined as the pressure difference between a point on the surface of the larynx and the subglottal pressure. The location of the points for which  $\Delta p^*$  was reported is shown on the top of each plot. The plots reveal a primary transitional region in which the non-dimensional differential pressure drops continuously. This happens concurrently with the linear velocity ramp rising from zero to its maximum value while a starting vortex also forms and moves toward the FVFs. The maximum pressure drop on the TVFs and laryngeal ventricle occurs when the starting vortex reaches the FVF gap (Figure 5-5(a) and Figure 5-5(b)). As the starting vortex passes through this gap, the non-dimensional differential pressure recovers partially; however, it remains nearly unchanged for the rest of the simulation. The non-dimensional differential pressure on the surface of the TVFs and laryngeal ventricle after the transitional region is higher for the models with narrow FVF gap; however, it is almost similar for the control model and the laryngeal models with wide FVF gap.

The non-dimensional differential pressure history on the surface of the FVFs (Figure 5-5 (c)) for the control model and the laryngeal models with wide FVF gap also shows the initial pressure drop followed by a partial pressure recovery; however, its value is lower at the FVFs compared to its values on the surface of the TVFs and the laryngeal ventricle. Moreover, some pressure fluctuations are observed after the pressure recovery which die out with time. These fluctuations for the laryngeal models with narrow FVF gap are stronger and occur sooner. The first pressure fluctuation for these models occurs as the starting vortex collides with the surface of the FVFs. It is followed by strong pressure fluctuations as a series of vortex structures formed at the jet flow pass the FVF

gap. These small vortex structures are produced by the shear layer stabilities and as mentioned raise the Strouhal number in the models with small  $G_{fvf}$ . The level of pressure fluctuation for G1 is higher than G2 (Plots of the non-dimensional differential pressure for G2 are omitted in the figure). These high pressure fluctuations are replaced by high frequency and low amplitude fluctuation during the rest of the simulation for G1 and G2

The translaryngeal resistance is often used to study the laryngeal functionality. The non-dimensional translaryngeal resistance in this work is defined as the ratio of the average non-dimensional translaryngeal pressure to the mean non-dimensional glottal flow rate. The values of the non-dimensional translaryngeal resistance for G1, G2, C1, G3, and G4 are 257, 267, 286, 289, and 290 respectively, and indicate that the non-dimensional translaryngeal resistance increases for the wider gaps of the FVFs. Moreover, the rate of change of non-dimensional translaryngeal resistance decreases for the wider FVFs gaps suggesting that the glottal flow is less affected with the presence of the FVFs. This observation is consistent with the experiments of Agarwal et al. [20] for the intermediate range of the  $G_{fvf}$ . They show that for a given glottal gap a critical ratio of the  $G_{fvf}$  to glottal gap exists for which the flow resistance exhibit a minimum. Although Agarwal et al. [20] did not plot the laryngeal resistance against the ratio of the  $G_{fvf}$  to the glottal gap for the uniform glottis, their plots for divergent glottis show that the minimum laryngeal resistance for the wider glottis shifts toward 1 on the axis indicating the ratio of the  $G_{fvf}$  to the glottal gap. This ratio for our laryngeal models ranges from 2.3 to 7.5 and is in the range reported for people without voice abnormalities.

Although a smaller translaryngeal resistance may suggest a more efficient phonation, the non-dimensional differential pressure plots in Figure 5-5 suggest that the narrower FVF gap will exhibit pressure fluctuations on the surface of the FVFs. These pressure fluctuations for the narrower FVF gap may be the main source of the aerodynamic force which results in involuntary or irregular FVFs oscillation in presence of voice abnormalities (e.g. ventricular dysphonia [105]).

In addition to computational simulations, wind-tunnel experiments are performed on G2, C1, and G4 laryngeal geometries to collect pressure data under the same flow conditions. It should be noted that the laryngeal models employed in this work are rigid with parallel TVFs. Therefore, the effect of the TVFs' oscillation is not examined in this study, and the rigid wall simplification allowed us to experimentally investigate the pressure distribution on the surface of the laryngeal models within a wind tunnel.

For each pressure tap on the experimental model, the non-dimensional differential pressure is collected and averaged over a window of 10 seconds. Similar to the computational simulations, the differential pressure in the experiments is measured with respect to upstream air pressure in the wind tunnel. The Reynolds number in the experiments is calculated based on the hydraulic diameter of the wind tunnel and the average velocity of air flow. In order to compare the experimental data with the computational differential pressure, these steady-state pressure data for the Reynolds number of 1000 have been non-dimensionalized using the mean upstream inlet velocity  $U_{ave}$ .

$$\Delta P^* = \frac{\Delta P}{\rho_{air} U_{ave}^2} \quad (5-3)$$

The value of  $\Delta P^*$  for G2, C1, and G4 models is presented in Table 5-2. It should be observed that most literature reports experimental results in the form of a pressure coefficient:

$$C_p = \frac{P}{0.5 \rho_{air} V_{ave}^2} \quad (5-4)$$

which is based on the average velocity at the glottis ( $V_{ave}$ ). Since the average velocity at the glottis is one order of magnitude larger than the inlet velocities investigated in this work, it is concluded that the current results are consistent with previous results from the literature [106, 107].

It is observed in Table 5-2 that the pressure decreases on the surface of the TVFs. This is expected due to the acceleration of the air flow in this region. The non-

dimensional differential pressures on the surface of the laryngeal ventricle are slightly lower than the TVFs, and are followed by partial pressure recovery at the FVF gap. This pattern of the pressure distribution is consistent with the experiments of Li et al. [35]. Furthermore, the pressure drop on the surface of the TVFs and laryngeal ventricle is smaller for the laryngeal model with small  $G_{\text{fvf}}$ .

In the experiments, the pressure data is collected after a steady-state flow is established in the wind tunnel. Therefore, it is not possible to measure pressure in the initial transient phase of the flow when the starting vortex is being created. Hence, the effect of the starting vortex is not measured experimentally. In order to compare the experimental and computational results, the computational pressure data after the pressure recovery are averaged on the TVFs, laryngeal ventricle, and FVFs (identical to “P2”, “P3”, and “P4” in the experiments, respectively) and tabulated in Table 5.3. The experimental non-dimensional differential pressure drop (Table 5-2) is slightly higher than the computational values, which can be due to three dimensional effects that could not be captured in our 2D simulations. The numerical and experimental pressure shows that the pressure drop on the surface of the larynx is approximately similar for C1 and G4 models, whereas it drops less on the laryngeal model with the smaller  $G_{\text{fvf}}$ . Moreover, in each model, the differential pressure is higher on the surface of the TVFs (P2) compared to the laryngeal ventricle (P3). It is observed that the widely-used assumptions of the Bernoulli equation within the speech society, which predicts full pressure recovery in the laryngeal ventricle, are inadequate to describe the pressure field within this region. The computational and experimental results are in good agreement, which again validate the fidelity of the computational solver.

The experiments were repeated for other Reynolds numbers and the pressure distributions are plotted for G2, C1 and G4 models in Figure 5-6. It is observed that the non-dimensional differential pressure drop is smaller for higher Reynolds numbers. This trend is consistent with the trend of transglottal pressure coefficients in Ref. [106].

### 5.6 The Effect of the Height between TVF and FVF.

Three laryngeal models were employed to study the effect of the size of the  $H_{\text{FVF}}$  on the glottal flow. These models will be referred as H1, C1, and H2 for which  $H_{\text{FVF}}$  is 5.3, 6.2, and 7.5 mm respectively. The Reynolds number and the boundary conditions of the computational simulations were similar to those described for performing the grid independent study.

The vorticity contours for these models are depicted in Figure 5-7. The coherent structures of the glottal jet flow including formation of the starting vortex followed by a trailing jet as well as flapping of this jet flow at the supraglottal region are observed in all models. Moreover, rebound vortices are formed at the laryngeal ventricle of these models; although, they do not reach the TVFs during the simulation.

The Strouhal was calculated for these models. The results show that the Strouhal number increases in the simulations as  $H_{\text{FVF}}$  decreases. The lowest value of the Strouhal number is for H2 ( $St=0.134$ ), while it is higher and nearly equal for the C1 and H1 models (0.151, and 0.152 respectively). A similar pattern was reported by Kucinski et al. [37] for the models with a small size  $G_{\text{FVF}}$  but with different  $H_{\text{FVF}}$ , although their Strouhal number values were smaller.

The non-dimensional differential pressure history on the surface of the TVFs and FVFs for these models is plotted Figure 5-8. The pressure initially drops for all models and then partially recovers and reaches a plateau. The values of the differential pressure are slightly higher on the surface of the TVFs compared to the FVFs. Moreover, some pressure fluctuations are observed on the surface of the FVFs (Figure 5-8 (c)) while the pressure is recovering. The magnitude of these pressure fluctuations is higher for the H2 model. The plot of the non-dimensional differential pressure on the surface of the laryngeal ventricle shows no pressure fluctuation and its trend is similar to pressure variation on the surface of the TVFs. However, the value of the non-dimensional differential pressure at this region is close to its values on the surface of the FVFs.

The results also show that the variation of the height between the TVFs and FVFs has minor effect on the non-dimensional translaryngeal resistance. The value of this parameter for H1, C1, and H2 are 288, 286, and 287 respectively.

The experiments were carried out for different Reynolds numbers and the pressure distribution is plotted for H1 and H2 models in Figure 5-9. The experimental non-dimensional differential pressure drop is in the same range of the computational results. It is observed that for the higher Reynolds numbers the non-dimensional differential pressure drop is smaller.

### 5.7 The Effect of the Width of the Laryngeal Ventricle

Three laryngeal models (hereafter L1, C1, and L2) were designed for which  $W_{lv}$  was 10.3, 15, and 19.7mm, respectively. The Reynolds number and the boundary conditions applied for computational simulations were similar to those described for performing the grid independent study.

Vertical structures in the laryngeal models with different  $W_{lv}$  are depicted in Figure 5-10. The main coherent structures of the glottal flow including formation of a starting vortex followed by a trailing jet and also flapping of the glottal jet are observed in all the models. The rebound vortex structures are also formed in these models due to interaction between starting vortex and the FVFs. The strength of these rebound vortices is similar and they move similar distances in the laryngeal ventricle toward the TVFs; although they do not reach the TVFs during the simulation. Furthermore, the influence of the size of  $W_{lv}$  on the Strouhal number for these laryngeal models is negligible (this value for L1, C1, and L2 is 0.152, 0.151, and 0.155 respectively).

The non-dimensional differential pressure history on the surface of the TVFs is plotted in Figure 5-11(a). The differential pressure drops while the starting vortex is forming and moving at the laryngeal ventricle. This pressure then recovers partially and reaches a plateau during the rest of the simulations. The greatest pressure drop is

observed for the control model, while the pressure for smaller and larger  $W_{IV}$  are approximately similar. A similar pattern is observed for the non-dimensional differential pressure on the surface of the laryngeal ventricle (Figure 5-11(b)). Moreover, the value of the differential pressure at the laryngeal ventricle is slightly more negative compared to its values on the TVFs.

The variations of the non-dimensional differential pressure with time on the surface of the FVFs are illustrated in Figure 5-11(b). The highest pressure drop at this region is also observed in the control model. Moreover, variation of the differential pressure is almost identical for the models. Some pressure fluctuations are observed at this region. These fluctuations occur as small vortices at the glottal jet flow are passing the FVFs gap. The scale and pattern of these fluctuations is approximately identical for the laryngeal models which is consistent with the similar Strouhal numbers found for these models.

The results also show that the non-dimensional translaryngeal resistance is highest in the control model compared to other laryngeal models of this group. This value for L1, C1, and L2 is 271, 286, and 273 respectively.

The experiments were carried out for other Reynolds numbers and the pressure distributions are plotted for L1 and L2 models in Figure 5-12. The experimental non-dimensional differential pressure drop is in the same range of the computational results. It is observed that the non-dimensional differential pressure drop is smaller on the same pressure taps at the higher Reynolds numbers. Additionally, at low Reynolds numbers the non-dimensional differential pressure drop is approximately similar for the laryngeal ventricle and the FVFs. However, the non-dimensional differential pressure drop for L2 is smaller on the FVFs compared to the laryngeal ventricle when the Reynolds number is equal or greater than 1968.

### 5.8 Oscillation of the Vocal Folds

In this section, the computational capability of the current solver to simulate the oscillation of the vocal folds is examined. The width of the laryngeal ventricle, the height between the TVFs and FVFs, and sizes of the FVF gap for the laryngeal model are similar to C1 model. A no-slip boundary condition was imposed on the larynx walls and the outlet boundary was treated with a convective outflow condition. The pulsatile velocity boundary condition implemented at the inlet was the following non-dimensional form:

$$u_{inlet}^* = 0.5 \left( 1 - \cos \left( \frac{\pi t^*}{0.15} \right) \right) \quad (5-5)$$

The oscillation of the TVFs was modeled using a two-mass model of the vocal folds (section 3-7). To maintain the stability of the computations the TVFs were not allowed to approach each other beyond 0.025 *mm*. The simulations were performed in parallel with 96 cores of Helium high performance computing center at the University of Iowa.

Each cycle of phonation starts with opening of the TVFs and ends with their closure. At the beginning of the opening phase, the air flow from the inlet increases the air pressure of the subglottal region which results in the separation of the inferior part (the first mass) of the TVFs from each other. The phase shift between the masses of the lumped element model results in the formation of the convergent glottis (Figure 5-13(b)). Simultaneously, the air flow from the glottis forms the starting vortices and the jet flow. These flow structures are affected by the residual vortical structures from the previous cycle in the laryngeal ventricle and the jet flow is deflected toward the walls of the vocal tract (Coanda effect). The velocity of the glottal jet increases concurrently with opening of the TVFs. This large velocity creates a low pressure zone at the glottis. Since the FSI coupling is established through the balance between the aerodynamics forces of the air and the vocal folds tissues, the pressure drop at the glottis and concurrent elevation of the

elastic force of the TVFs tissue decelerate the opening of the TVFs. At the mid-phase of the phonation, the glottis has a parallel configuration (Figure 5-13(c)). The closure phase starts when the inferior part of the TVFs start approaching each other. This creates a divergent glottis and the jet flow separates from the surface of the TVFs (Figure 5-13(d)). The location of the separation point changes as the divergent orientation of the vocal folds varies. The closure phase is terminated with a parallel configuration of the vocal folds when they reach the minimum allowed glottal gap (Figure 5-13(a)).

### 5.9 Conclusion

In this chapter the effect of the size of the FVF gap, the height between the TVFs and FVFs, and the width of the laryngeal ventricle was studied computationally and experimentally using rigid laryngeal models. The results show that the size of FVFs gap was the main geometrical parameters affecting the glottal flow dynamics.

The coherent structures of the glottal flow observed in the computational simulations, including the formation of the starting vortex, the trailing jet flow, and its flapping was in good agreement with previous experimental flow visualizations. Formation of the starting vortex created a pressure drop on the surface of the TVFs, laryngeal ventricle, and FVFs and as this vortex structure passed the FVF gap, pressure recovered partially. Moreover the interaction between the starting vortex and the FVFs created rebound vortices in the laryngeal ventricle. These vortices moved in the laryngeal ventricle toward the TVFs and it was shown that they could collide with the glottal jet flow in the laryngeal ventricle and reach the surface of the TVFs in models with narrow FVF gap in a time period comparable with one cycle of phonation.

The numerical experiments indicate that a smaller FVF gap size (smaller than the ratio of 0.65 for the simulations in this study) has the potential to destabilize the glottal jet as a result of a strong interaction between the starting vortex and the FVFs, as well as creation of complex vortical structures in the laryngeal ventricle. The vortex shedding from the TVFs created pressure fluctuations on the surface of the larynx and it was shown that the small size of the FVF gap can considerably amplify this pressure oscillation.

The non-dimensional differential pressure was higher in the models with narrow FVF gap; however, it remained unchanged for the control model and the models with wider FVF gap. The results also suggest that the non-dimensional differential pressure was smaller in the control model compared to the models with smaller and larger width of the laryngeal ventricle. Moreover, the effect of the height between TVFs and FVFs on the differential pressure was negligible.

Finally, a two mass-model was incorporated into the fluid solver to model the oscillation of the TVFs. It was shown that the model is able to capture the main physiological features of the vocal folds oscillation including the convergent, parallel, and divergent orientation of the TVFs in a cycle of phonation.

Table 5-1 Summary of geometrical parameters used to design the laryngeal models.

	C1	G1	G2	G3	G4	H1	H2	L1	L2
$G_{fvf}$	5.1	2.3	3.3	6.3	7.5	5.1	5.1	5.1	5.1
$H_{fvf}$	6.2	6.2	6.2	6.2	6.2	5.3	7.5	6.2	6.2
$W_{lv}$	15.0	15.0	15.0	15.0	15.0	15.0	15.0	10.3	19.7

Note: C1 is the control model which is approximately designed based on average laryngeal geometries of the human larynx. All the parameters are defined in millimeters.

Table 5-2 Non-dimensional differential pressures collected in the experiments on the surface of the models with different FVF gap.

	P1	P2	P3	P4	P5	P6
G2	-64.9605	-289.538	-324.802	-313.666	-315.522	-309.954
C1	-59.3556	-278.713	-293.746	-283.713	-293.746	-297.326
G4	-63.9408	-291.087	-315.99	-316.339	-316.339	-318.625

Table 5.3 Non-dimensional differential pressures on the surface of the larynx in the computational simulations.

	TVF	LV	FVF
G2	-283.864	-295.555	-295.907
C1	-266.681	-278.557	-280.432
G4	-284.239	-296.133	-296.441

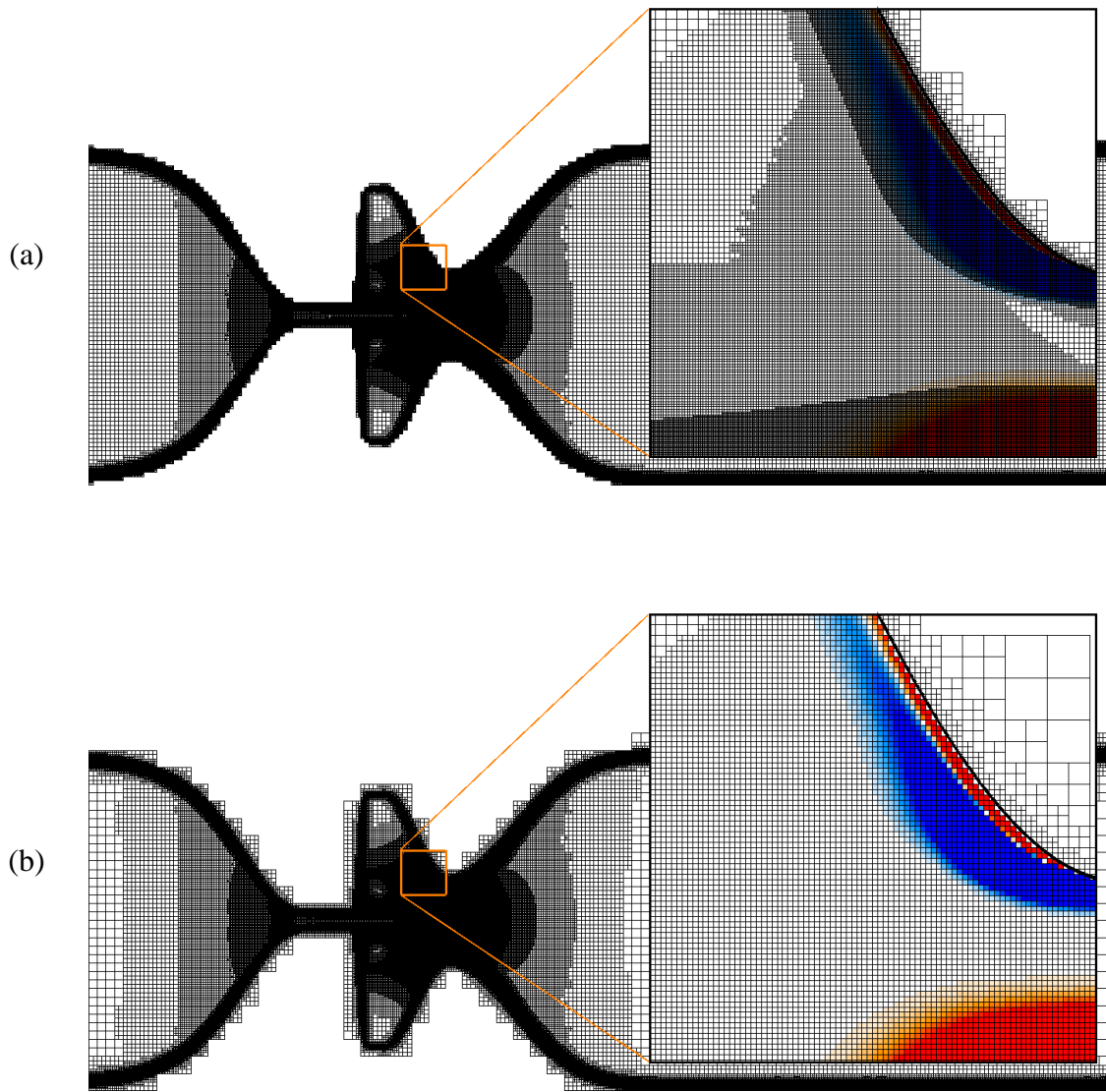


Figure 5-1 Grid refinement study: Comparison between the fine (a) and coarse (b) mesh. The Cartesian mesh interior to the solid that is not required for the ghost fluid treatment is pruned during the simulation for improved memory performance.

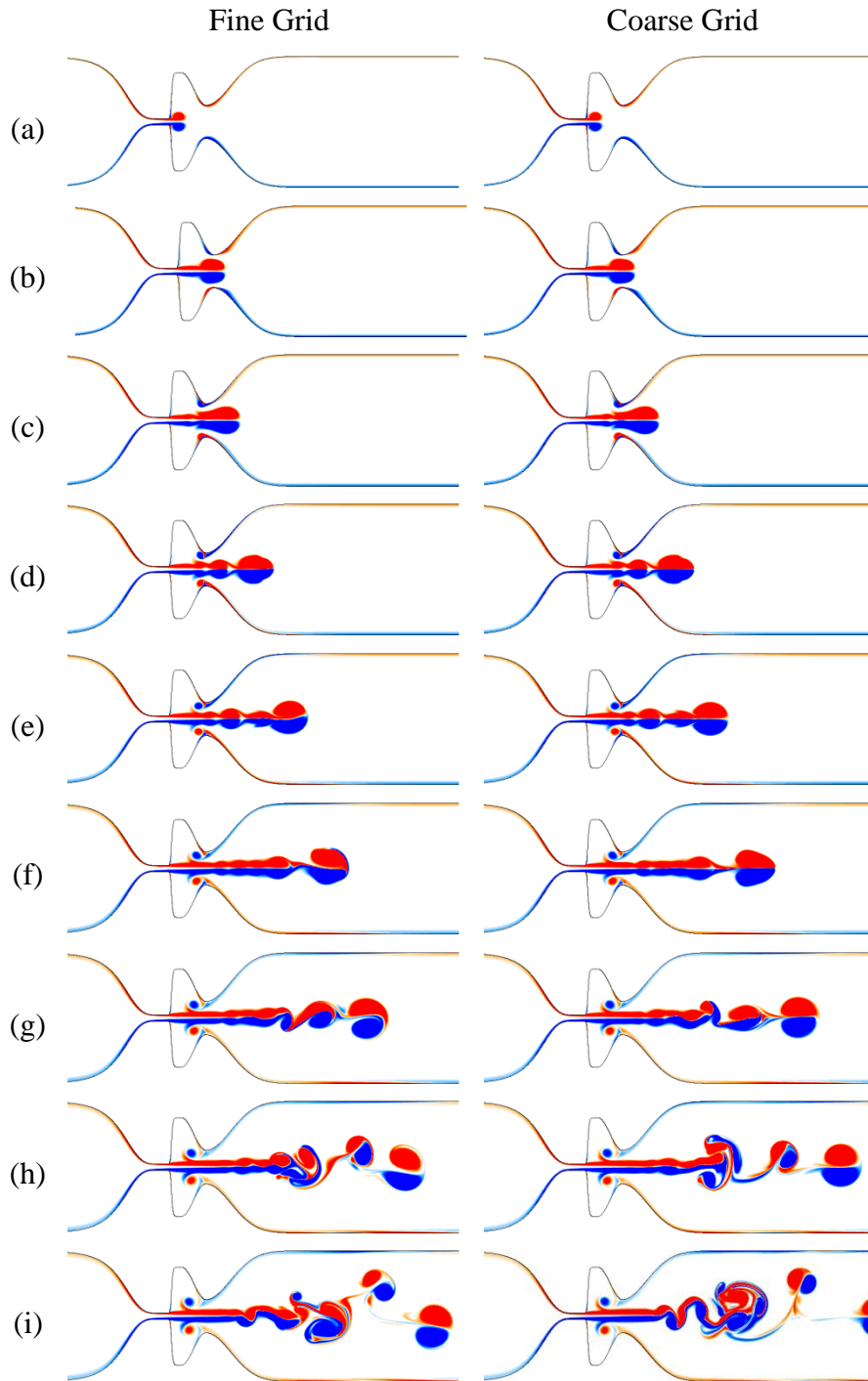


Figure 5-2 Comparison between the vorticity contours of the coarse and fine grid at  $t^* = 0.064, 0.104, 0.128, 0.152, 0.176, 0.208, 0.24, 0.272, \text{ and } 0.304$  respectively.

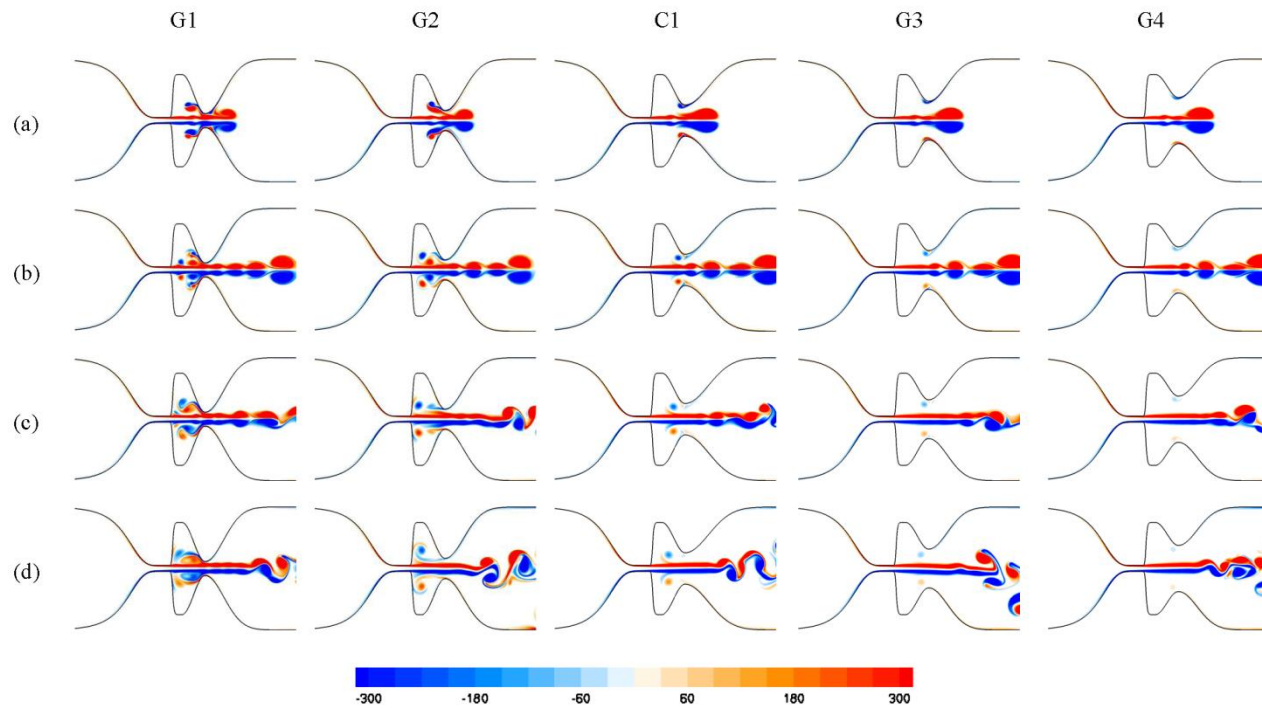


Figure 5-3 Non-dimensional vorticity contours for the laryngeal models with different size of the  $G_{fvf}$  at non-dimensional time ( $t^*$ ) of (a) 0.128, (b) 0.176, (c) 0.24, and (d) 0.304. The interaction between the starting vortex and the FVFs increases as the  $G_{fvf}$  decreases; hence, rebound vortices in the laryngeal ventricle of the models with narrow  $G_{fvf}$  are stronger

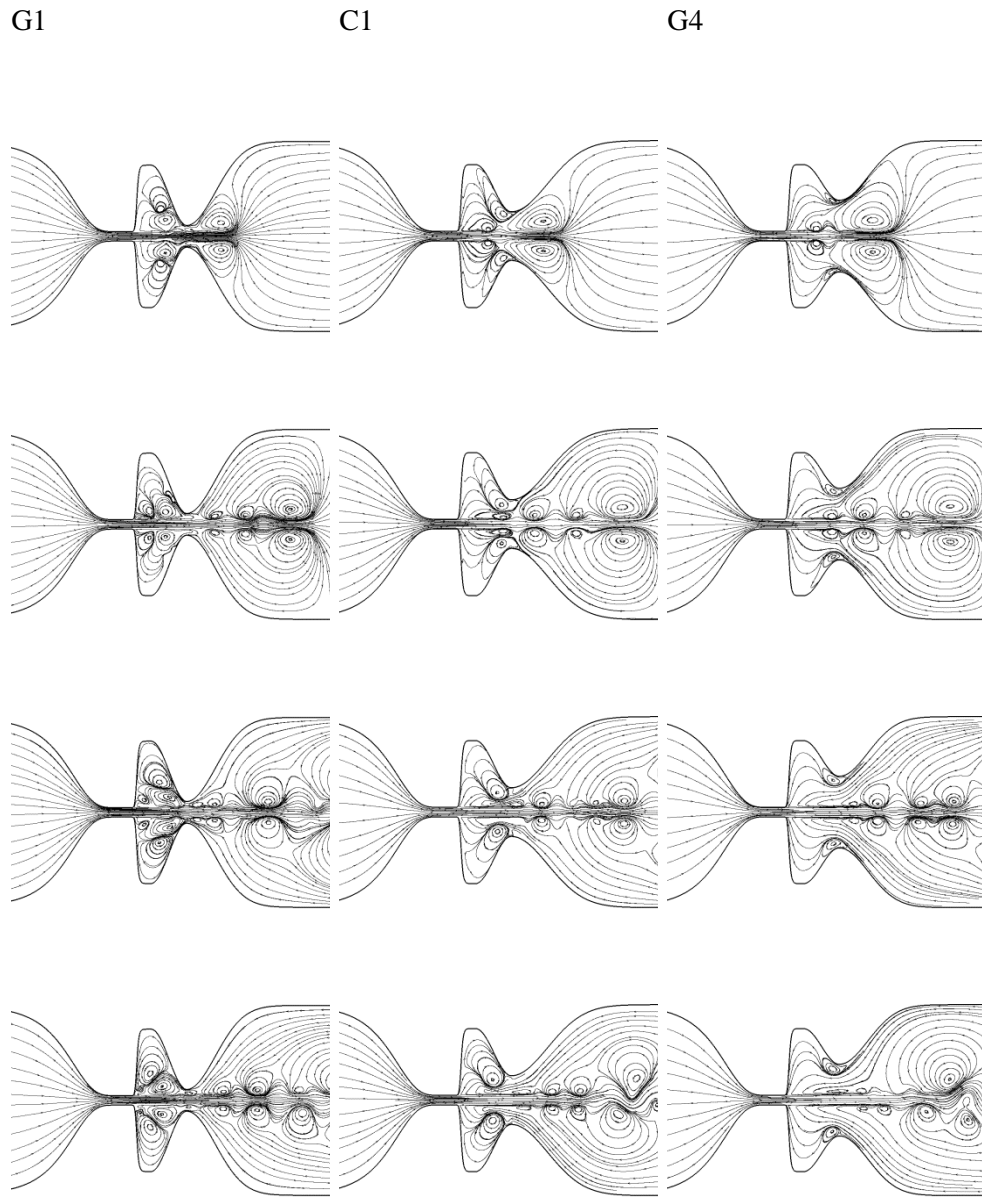


Figure 5.4 Streamline contour of the glottal flow for the G4 laryngeal model at at non-dimensional time ( $t^*$ ) of (a) 0.128, (b) 0.176, (c) 0.24, and (d) 0.3.

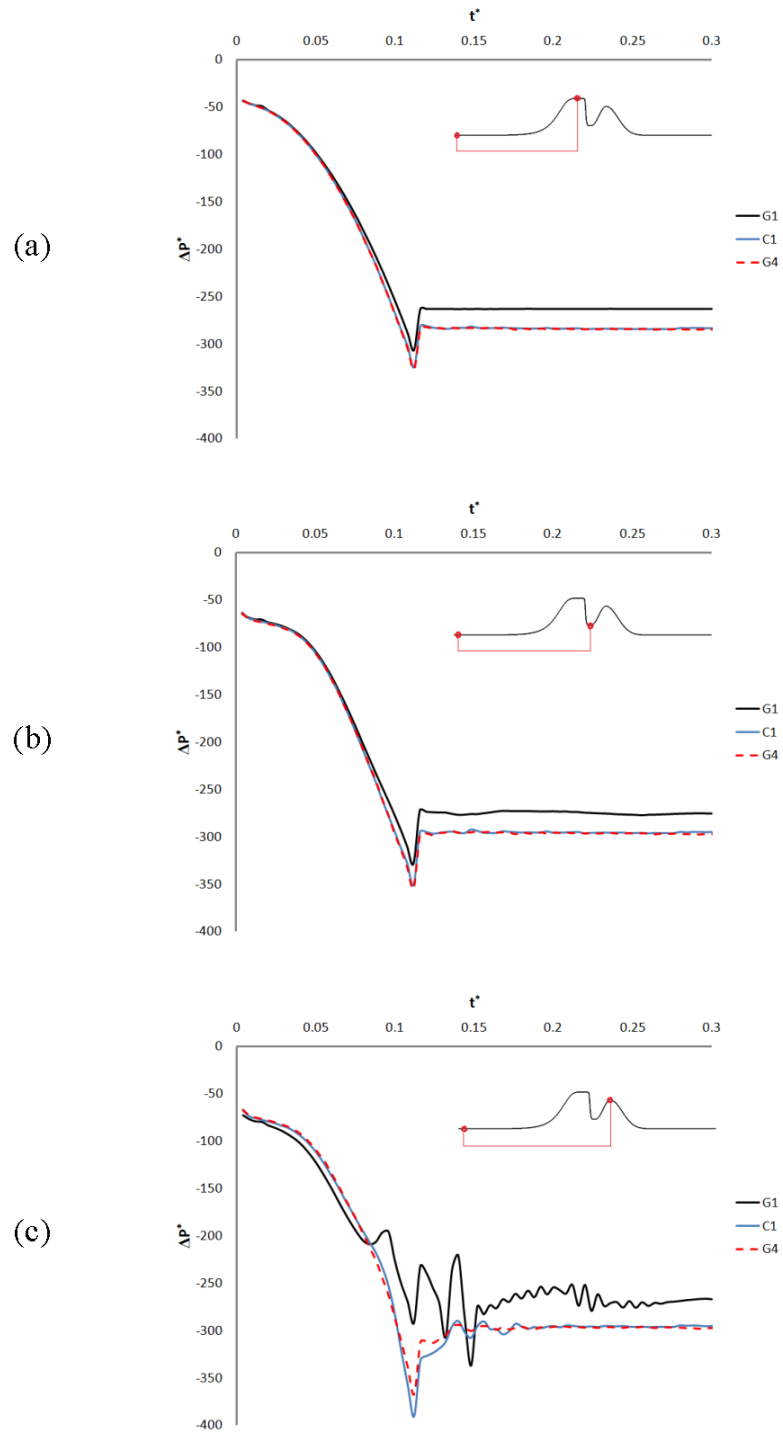


Figure 5-5 Non-dimensional differential pressure ( $\Delta P^*$ ) history on the surface of the TVFs (a), laryngeal ventricle (b), and FVFs (c) for models with different size of FVF gap.  $t^*$  is the non-dimensional time. The pressure initially drops as the starting vortex is created and convected in the laryngeal ventricle, and then recovers partially for the rest of the simulation. Moreover, pressure data on the surface of the FVF fluctuate for the models with narrow  $G_{fvf}$ .

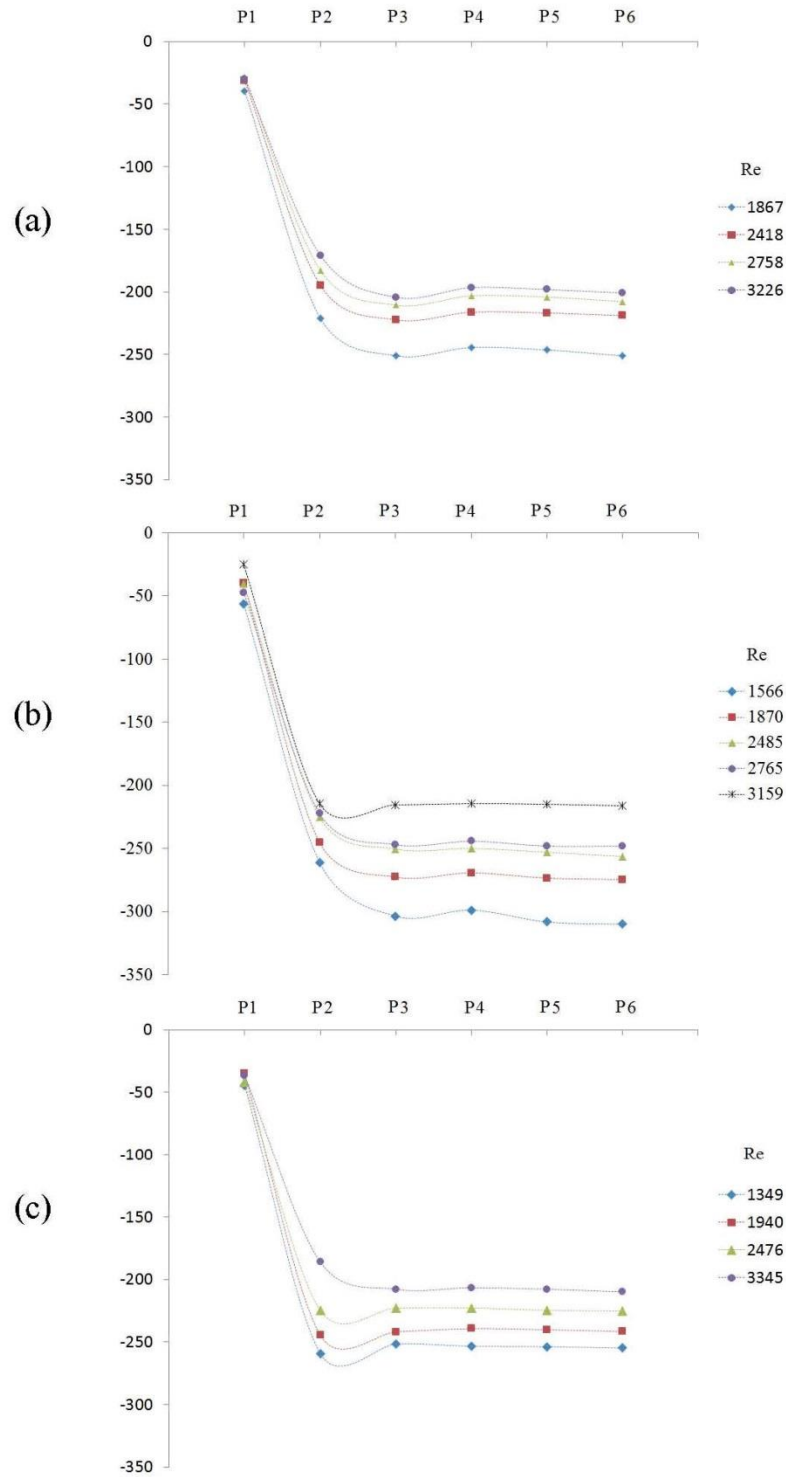


Figure 5-6 Plots of non-dimensional differential pressure ( $\Delta P^*$ ) for (a) G2 model, (b) C1, and (c) G4 laryngeal models.

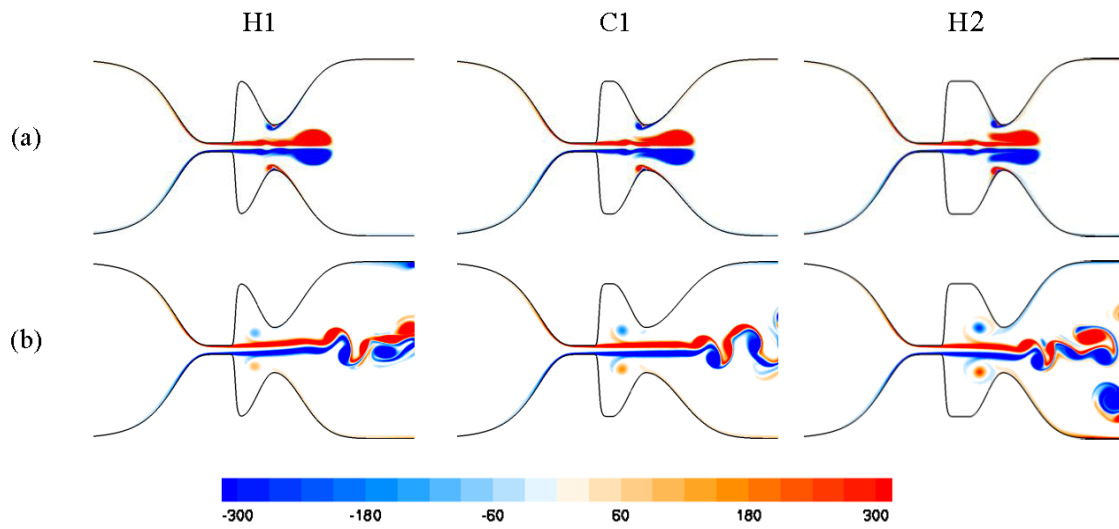


Figure 5-7 Non-dimensional vorticity contours for the laryngeal models with different size of  $H_{fvf}$  at non-dimensional time ( $t^*$ ) of (a) 0.128, and (b) 0.304 respectively.

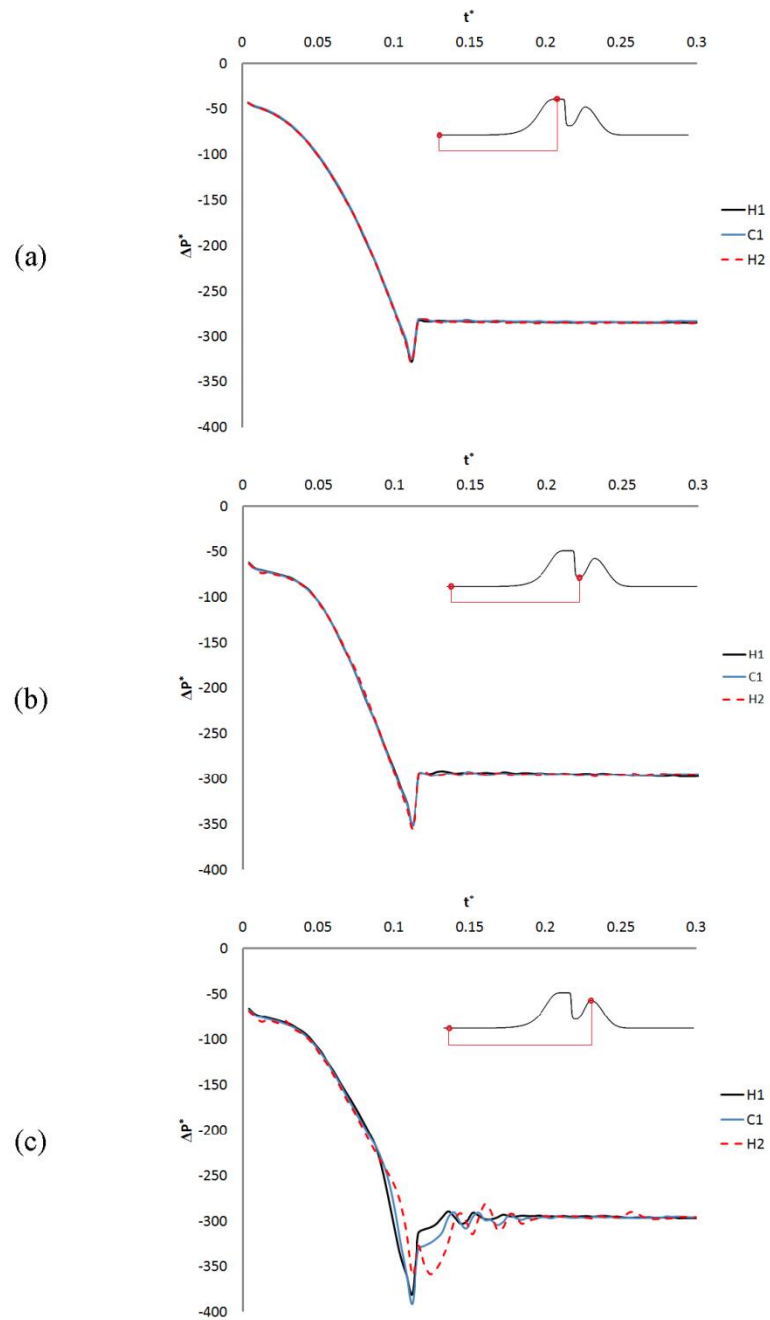


Figure 5-8 Non-dimensional differential pressure ( $\Delta P^*$ ) history on the surface of (a) TVFs, and (b) laryngeal ventricle, and (c) FVFs for models with different size of  $H_{IVF}$ .  $t^*$  is the non-dimensional time.

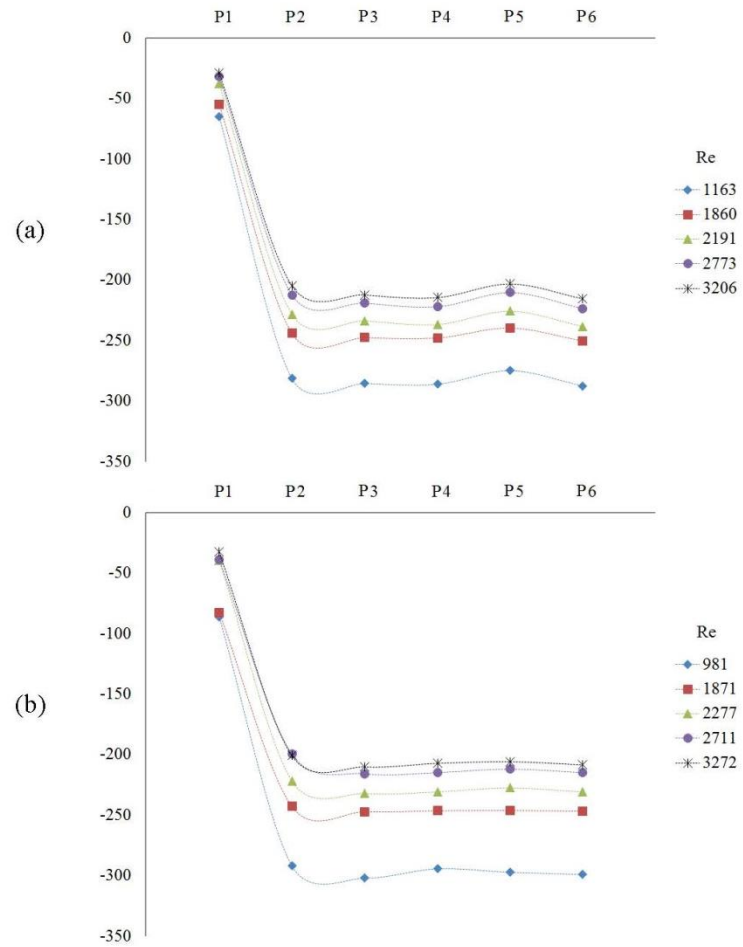


Figure 5-9 Plots of non-dimensional differential pressure ( $\Delta P^*$ ) for (a) H1 model, (b) H2, laryngeal models.

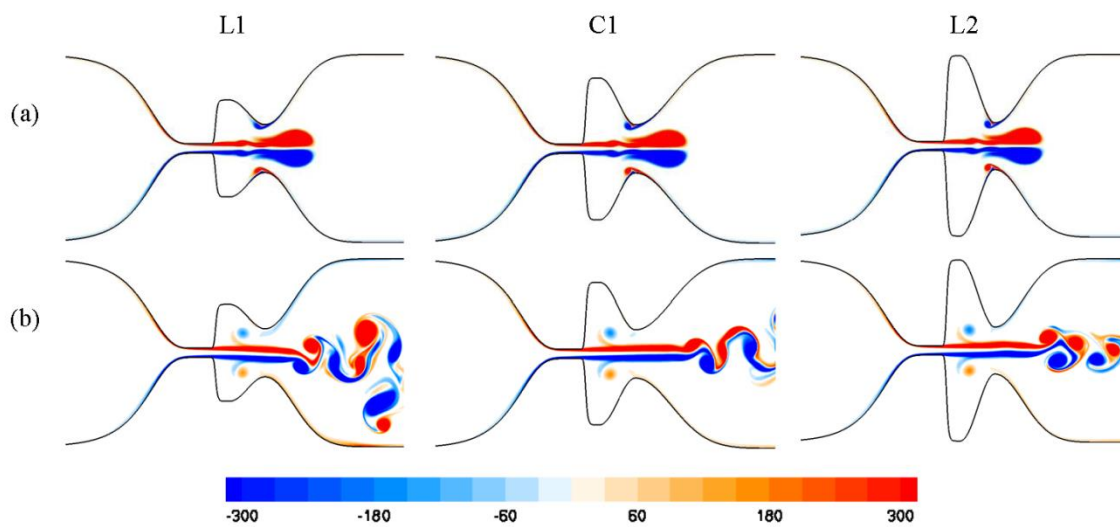


Figure 5-10 Non-dimensional vorticity contours for the laryngeal models with different size of at non-dimensional time ( $t^*$ ) of (a) 0.128, and (b) 0.304.

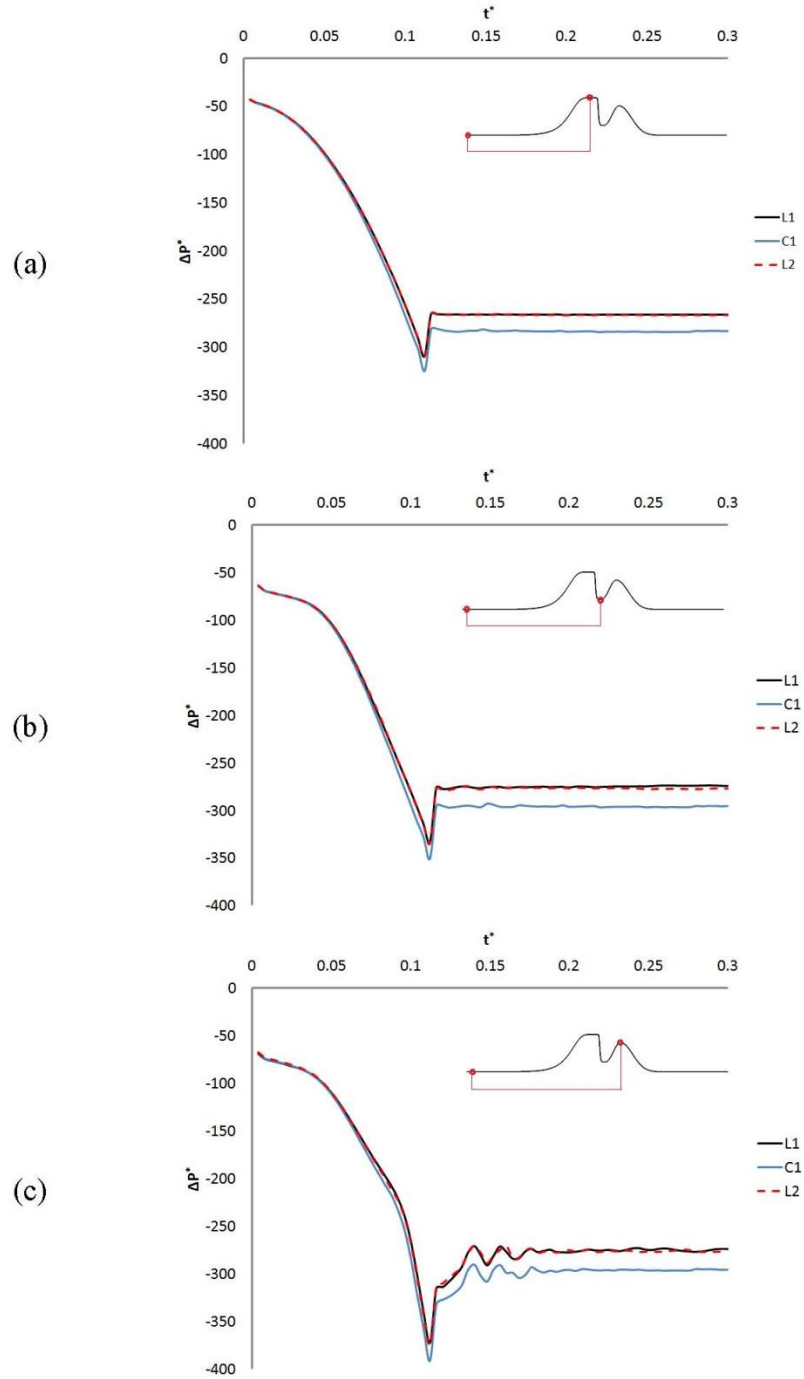


Figure 5-11 Non-dimensional differential pressure history on the surface of TVFs, laryngeal ventricle, and FVFs for models with different size of  $W_{IV}$ .

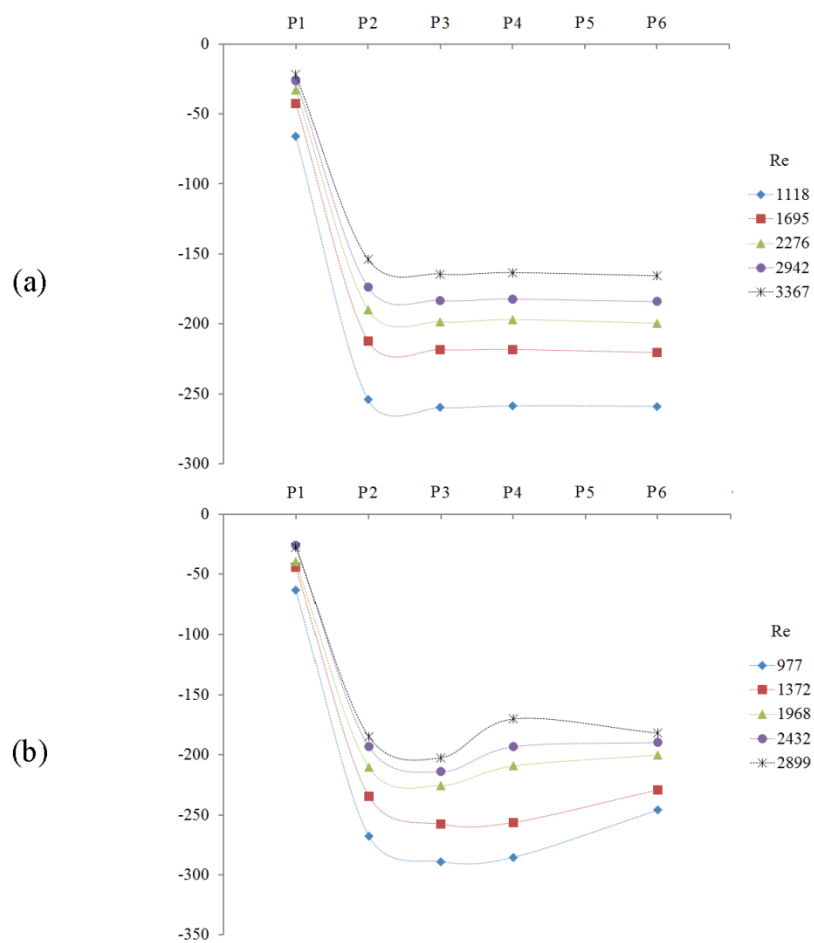


Figure 5-12 Plots of non-dimensional differential pressure ( $\Delta P^*$ ) for (a) L1 model, (b) L2, laryngeal models.

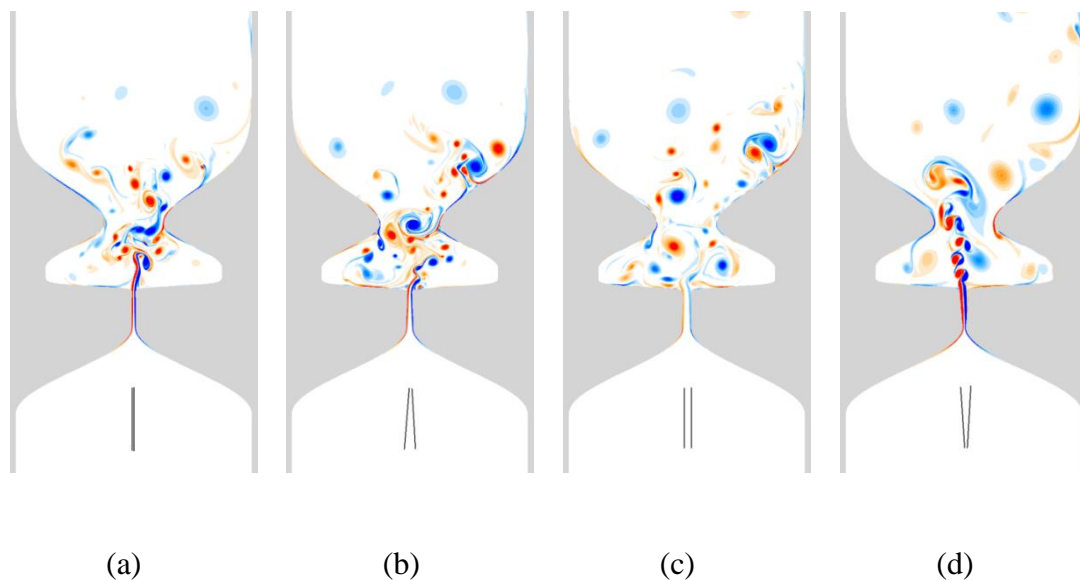


Figure 5-13 Vorticity contours during the self-sustained oscillation of the vocal fold, (a)  $t^*/T = 0.01$ , (b)  $t^*/T = 0.25$ , (c)  $t^*/T = 0.5$ , (d)  $t^*/T = 0.75$ .  $T$  is the time period of the oscillation. The orientation of TVFs surfaces is shown at the bottom of each figure to provide better clarity.

CHAPTER 6  
TOWARD PATIENT SPECIFIC SIMULATION OF THE AIR FLOW IN  
THE LARYNX

6.1 Introduction

In Chapter 5 the effects of the FVF geometry on the flow structures of the glottal jet were investigated using two-dimensional simulations in idealized laryngeal geometries. It was shown that the current parallel solver is capable of providing fully-resolved flow simulations in the region immediately after the glottis. Hence, we were able to capture flow structures like the rebound vortices in the laryngeal ventricle that have been rarely reported in the literature. The review of Section (1.3.3) indicates that simulations of flow through realistic larynx geometries are still lacking in the literature. Furthermore, the flow field in majority of the three dimensional simulations of the larynx is under-resolved. In order to adequately resolve flow structures, some researchers have reduced the Reynolds number to below the physiologic range to decrease the computational effort of conducting DNS [49]. Alternatively, the Reynolds number was modeled as being higher than the normal physiological range in order to exploit a turbulent model [15].

Indeed, it is desirable to extend our computational capabilities to three-dimensional simulation of glottal flow in physiologically realistic larynx geometries. To achieve this milestone, a framework to extract the geometry of the larynx from medical images is presented in this chapter. These realistic geometries are utilized to conduct fully-resolved three-dimensional simulations in a direct numerical simulation (DNS) fashion. Most notably, as opposed to current state-of-the-art DNS simulations of laryngeal flow, our fully-resolved simulations are performed at physiologically accurate Reynolds numbers.

## 6.2 Image Segmentation of the Larynx

This section describes the method employed for segmentation of the larynx. In order to provide a better insight into the procedure, the results of each step are depicted for CT scan images of a 45-year-old human female excised larynx. The CT scan images were acquired at UIHC with a Siemens scanner. The data set consisted of 295 image slices, each  $512 \times 512$  pixels in size with a pixel dimension of  $\Delta x = \Delta y = 0.127$  mm. The larynx geometry was isolated by cropping the image to a  $128 \times 128 \times 57$ -voxel subregion (Figure 6-1) prior to segmentation.

Image segmentation is the process of locating object boundaries through partitioning of a digital image. The segmentation technique used in this chapter is based on intensity thresholding of the pixels/voxels. In this method a threshold  $C$  is subtracted from the gray scale intensity of the image voxels  $I_0$  and the voxels are simply partitioned smoothly into two subregions with negative and positive intensities  $I$ .

$$I = I_0 - C \quad (6-1)$$

The location of the boundaries is delineated using a bilinear interpolation between the neighboring intensity levels at the partition boundaries. Figure 6-2 shows the zero-level iso-surface in the intensity field resulting from thresholding the current CT scan images. To identify and extract objects of interest to be modeled from the segmented image domain an object-labeling scheme is adapted [108]. In this method a null tag is assigned to the all points in the image. The points are scanned in their natural order of numbering until a point is reached in which the sign of  $I$  changes from negative to positive. This point is tagged with an object number 1 (Figure 6-3(a)). The neighbors of the current point are then located, and those with positive  $I$  are also tagged with an object number 1 (Figure 6-4(b)). This procedure is continued for the neighbors of all the newly tagged neighbors until no neighbor with positive intensity is found. The scanning is resumed from the first point of the first object until a point with positive  $I$  and a null

object numbering tag is found. This point is tagged with object number 2 (Figure 6-4(b)). Similar to the first object, all the neighbors and their neighbors with positive  $I$  are tagged with an object number 2. This procedure is continued until all the points in the image domain are scanned and assigned an object number (Figure 6-4(d)). Applying this algorithm to the segmented images of the human larynx identified three primary objects, which are depicted in Figure 6-4. Once all the objects are tagged, the objects that are not required for the flow simulation can be removed.

In the flow solver, interfacial boundaries are represented using zero level set iso-contours embedded in a Cartesian grid. In order to convert the segmented image into an interface representation that is compatible with the flow solver, it is possible to construct a level set field for the image boundaries from the zero-level boundaries created during the segmentation process. This was accomplished by computing the distance of each interface voxel from the boundary using bilinear interpolation, then implementing a fast-marching technique for level set initialization using these interface distance values [54].

Once reconstructed, the segmented laryngeal boundaries and their resulting level set field have an irregular shape, as they are representative of a physiologically realistic geometry. Furthermore, since the current geometry is obtained from an excised larynx, it lacks the upper respiratory tract and part of the trachea. For computational accuracy purposes, input and output boundaries must be placed far enough from the region of computational interest to not interfere with the flow structures there. To address this issue, a seamless transition from the edges of the segmented larynx at the trachea and supraglottal region (source level set fields  $\psi_S$ ) to circular inlet and outlet boundaries (target level set fields  $\psi_T$ ) is established using an image morphing technique (Figure 6-5(a)). In this method, a smooth transition from the source (irregular) level set field to the target (circular) field is provided by constructing a series of smoothly-varying intermediate level set layers between the given source and target level sets. The

intermediate level set fields are modeled as having elastic properties, and the transition is enforced by modulation of a potential force. The maximum potential force is:

$$F_{max} = \mathcal{H}(\psi_T) - \mathcal{H}(\psi_S), \quad (6-2)$$

where  $\mathcal{H}$  is the Heaviside of the level set field

$$\mathcal{H}(\psi) = \frac{1}{2} \left( 1 + \frac{2}{\pi} \arctan \left( \frac{\psi}{\Delta} \right) \right), \quad (6-3)$$

and  $\Delta$  is the grid spacing. The target force in each intermediate layer  $k$  is a fraction of  $F_{max}$  and is defined as:

$$F(\psi_k) = (F_{max}) \cdot f \quad (6-4)$$

where  $f$  is a fraction of a pseudo time  $t$  between source and target configurations.

$$f = \frac{t}{T} \quad (6-5)$$

In Equation (6-5)  $T$  is the total pseudo time between source and target configurations, which is defined based on the total number of intermediate level set layers  $N_l$ . At the beginning of each time step the intermediate level set  $\psi_M$  is equal to  $\psi_S$ . Therefore an intermediate potential force can be defined for each layer as:

$$F(\psi_M) = \mathcal{H}(\psi_T) - \mathcal{H}(\psi_M). \quad (6-6)$$

The level set morphing evolves in time using Adams-Bashforth scheme such that it satisfies the following CFL criterion:

$$\frac{\Delta t \cdot \max(F_m)}{\max(\Delta x, \Delta y, \Delta z)} \leq \text{CFL} \quad (6-7)$$

Considering the following root mean square force in each layer with  $N$  cells

$$F_{rms} = \sqrt{\frac{\sum_{i=1}^N (F)_i^2}{N}}, \quad (6-8)$$

iterations are performed until  $(F_{rms}(\psi_k) - F_{rms}(\psi_m)) \leq \varepsilon$ . Here  $\varepsilon$  is a convergence criterion.

In this work the value of  $f$  for the  $k^{\text{th}}$  layer was defined using a sigmoid function for  $N_l$  total number of intermediate level set layers.

$$f = 1 - \frac{1}{1 + e^{(-12(1/2 - k/N_l))}} \quad (6-9)$$

Figure 6-5(b) shows the morphing process for the supraglottal region in more detail. The final level set field is mapped into the Cartesian grid of the incompressible solver. The same process was repeated for an excised Canine larynx. The geometries of the human and canine larynges are depicted in Figure 6-6.

### 6.3 Fully Resolved Simulation of the Glottal Flow in the Human and Canine Larynges with an Steady Inlet Flow

In this section the segmented human and canine laryngeal geometries are employed to conduct fully resolved fluid flow simulation. The Reynolds number of these simulations is 500, which is defined based on the inlet velocity and diameter. The inlet is modeled with a constant steady velocity and the outlet is treated using a convective outflow condition. The no-slip boundary condition is imposed in the laryngeal geometries' interfaces. Time stepping is adapted so that the simulations satisfy the CFL  $\leq$  1 condition. The simulation performed in parallel using 272 cores of the Helium high performance computing cluster at the University of Iowa.

The simulation for the canine larynx started with approximately 12,700,000 grid cells after the start up refinement, and terminated with 36,000,000 grid cells. The Cartesian grid cells outside of the flow simulation region (i.e. in the solid), and far enough from the interface to not be required for boundary condition implementation, were pruned during the simulation for improved memory performance. The contour of the x-vorticity is depicted in Figure 6-7 on a lateral planar slice that cuts through the TVFs and FVFs.  $\lambda - 2$  iso-surfaces colored by vorticity magnitude are shown in Figure 6-8 for the same time steps. Initially, a vortex ring was formed immediately after the TVFs ( $t^* = 0.1$ ). This vortical structure in the lateral surface of the Figure 6-7 is similar to the starting vortices captured in the two- dimensional simulations discussed in Chapter 5. The vortex ring was squeezed into the FVFs gap while small secondary vortices

(rebound vortices) were created in the laryngeal ventricle near the FVFs. At the same time ( $t^* = 0.3$ ), another vortex ring detached from the surface of the FVFs, similar to phenomena observed in the experiments of Chisari et al. [18]. The  $\lambda - 2$  iso-surfaces of Figure 6-8 illustrate that a strong jet flow is created at the posterior side of the glottis and moves toward the anterior side of the larynx. The flow field at the supraglottal region shows the evolution and interaction of these vortical structures and formation of a complex three dimensional flow pattern. It is observed that the vortical structures are deflected toward the anterior side of the larynx at the supraglottal region.

The simulation of laryngeal flow in the human larynx was performed using the same boundary conditions and Reynolds number used in the canine larynx simulation. This simulation started with a nearly 11,500,000 Cartesian grid cells after the startup refinement and terminated with about 26,000,000 grid cells. The y-vorticity contour on a lateral planar slice at the middle of the glottis is depicted in Figure 6-9. The  $\lambda - 2$  iso-contour surfaces colored by vorticity magnitude are also illustrated in Figure 6-10. Similar to the glottal flow in the canine larynx, a vortex ring was created after the glottis ( $t^* = 0.1$ ). This vortex ring passed the FVFs gap while interacting with the FVFs tissue ( $t^* = 0.3$ ). This flow-tissue interaction results in the formation of rebound vortices in the laryngeal ventricle ( $t^* = 0.4$ ). At this time, a vortex ring was detached from the surface of the FVFs and moved to the downstream of the glottis. Finally, the vortical structures of the trailing jet interacted with the leading starting vortex, resulting in a highly three-dimensional flow field.

It is observed that, as opposed to the glottal flow in the canine larynx, the vortical structures in the human larynx did not deflect at the downstream of the glottis. The human larynx used in the current work had a wider glottis compared to the canine larynx; hence, the magnitude of the vortices was smaller in the human larynx.

The fully resolved flow field at the ventricular fold for both the canine and human larynx revealed the formation of the rebound vortices in a realistic three-dimensional

geometry of the larynx. This fact supports the observations of Chapter 5, including the formation and evolution of these vortical structures in the two-dimensional simulations.

#### 6.4 A Fully Resolved Simulation of the Glottal Flow in a Human Larynx with a Pulsatile Inlet Flow

In this section glottal flow is simulated in the human larynx geometry with a more physiologically accurate Reynolds number and inlet boundary condition. Here, the inlet boundary is modeled using a pulsatile velocity:

$$u_{inlet}^* = 0.5 \left( 1 - \cos \left( \frac{\pi t^*}{T} \right) \right) \quad (6-10)$$

where  $T$  is the time period of each cycle of the velocity pulse at the inlet boundary. The simulation is performed at a peak Reynolds number of 1000 for 10 velocity cycles. The simulation was performed in parallel using 272 cores of the Helium high performance computing cluster at the University of Iowa. The contours of  $x$ ,  $y$ , and  $z$  components of the vorticity on a planar slice in the lateral direction is depicted for the last velocity pulse in Figure 6-11, Figure 6-12, and Figure 6-13 respectively. At the beginning of the tenth cycle, the inlet velocity was zero. A residual vortex ring from the previous cycle was located at the upstream of the FVF gap, and the supraglottal region after the FVFs was occupied by a highly three dimensional flow field ( $t^* = 9.0 T$ ). This vortex ring squeezed into the FVF gap and gave rise into the formation of new rebound vortices in the laryngeal ventricle ( $t^* = 9.25 T$  and  $t^* = 9.5 T$ ). At the same time a new shear layer started to roll up at the glottis. These phenomena are more obvious in Figure 6-12 where the planar slice is perpendicular to the  $y$  component of the starting vortex. Finally, a new vortex ring was created and moved toward the FVF gap.

An obvious difference between the flow simulations with steady and pulsatile inlet flow conditions occurs in the dynamics of the flow structures at the laryngeal ventricle. In the simulation with the steady inlet, the interaction between the initial vortex

ring and the FVFs created rebound vortices in the laryngeal ventricle. Following this, the flow field in the laryngeal ventricle was similar to a cavity flow and the vortices in the laryngeal ventricle were driven in the presence of the shear layer of the glottal jet. In the simulation with a pulsatile flow, vortex rings are created sequentially and the interaction between these vortex rings and the FVFs creates new rebound vortices in the laryngeal ventricle during each pulse.

### 6.5 Conclusion

In this chapter a framework was discussed to extract physiologically realistic three-dimensional laryngeal geometries from CT scan images. These geometries were used to conduct fully resolved computational simulations of laryngeal flow. The simulations illustrated that the glottal flow is highly three-dimensional. The glottal flow was initially created in the form of a vortex ring at the glottis. The vortex ring squeezed into the FVF gap and created rebound vortices in the laryngeal ventricle. Additionally, a second rebound vortex detached from the FVFs in the simulations with steady inlet velocity, similar to the observation of Chisari et al. [18]. The formation of the second vortex ring did not occur in the simulation with a pulsatile subglottal flow due to presence of residual vortical structures after the FVFs.

The formation of the rebound vortices in the three-dimensional realistic geometries of the larynx supports the observations of Chapter 5, including the formation of these vortical structures and their evolution in the laryngeal ventricle.

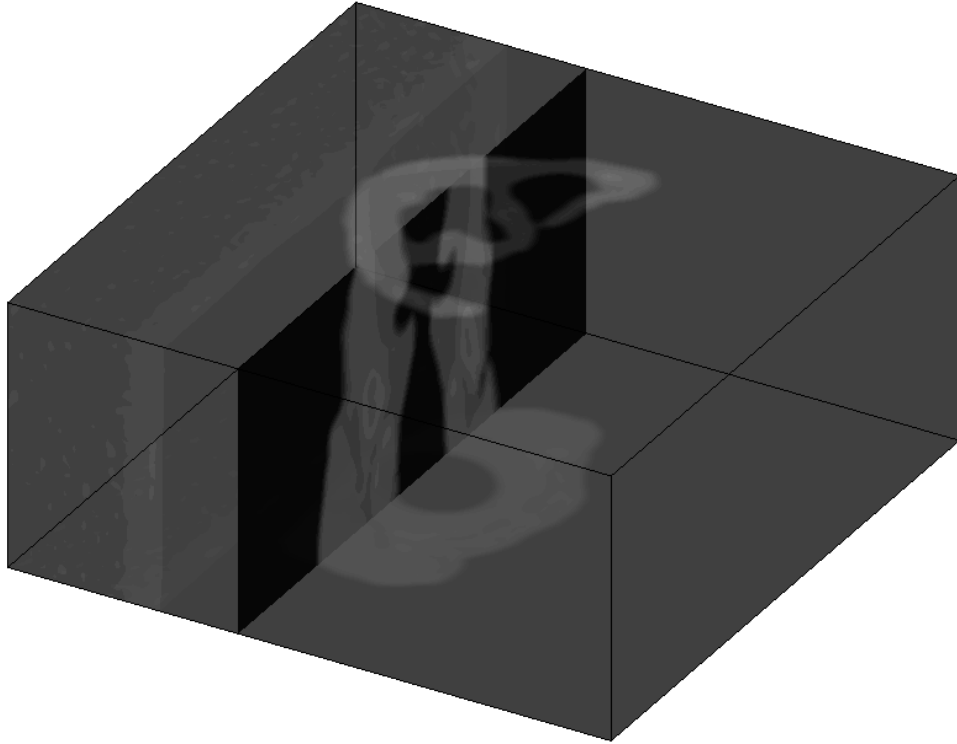


Figure 6-1 The cropped image of the human larynx obtained from CT scan images.

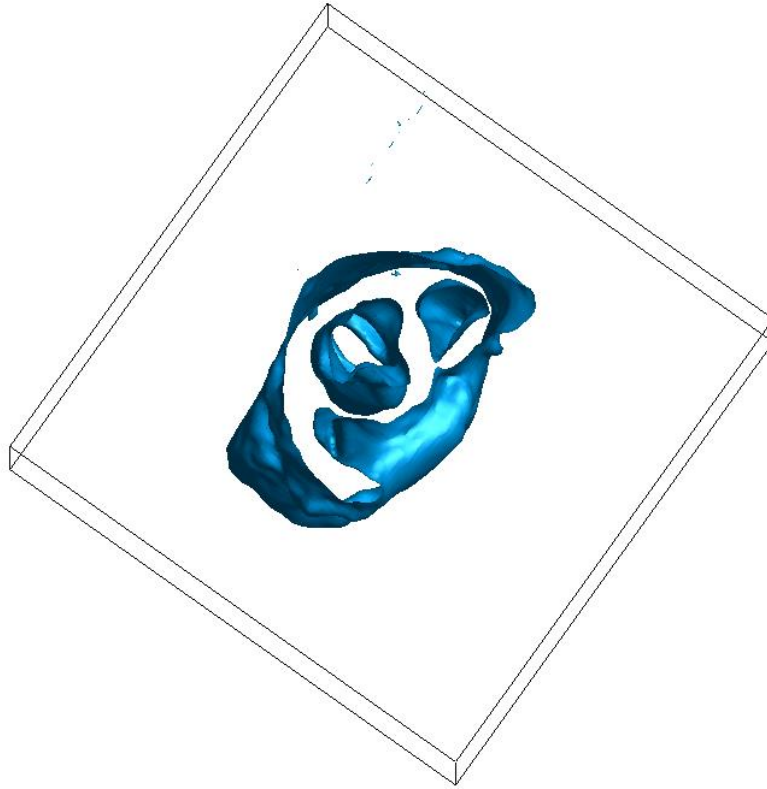


Figure 6-2 A top view of the interpolated boundaries after thresholding the voxels. The figure shows an outer boundary, the larynx at the middle, another boundary from some extra tissue on the right of the larynx, and some small closed boundaries.

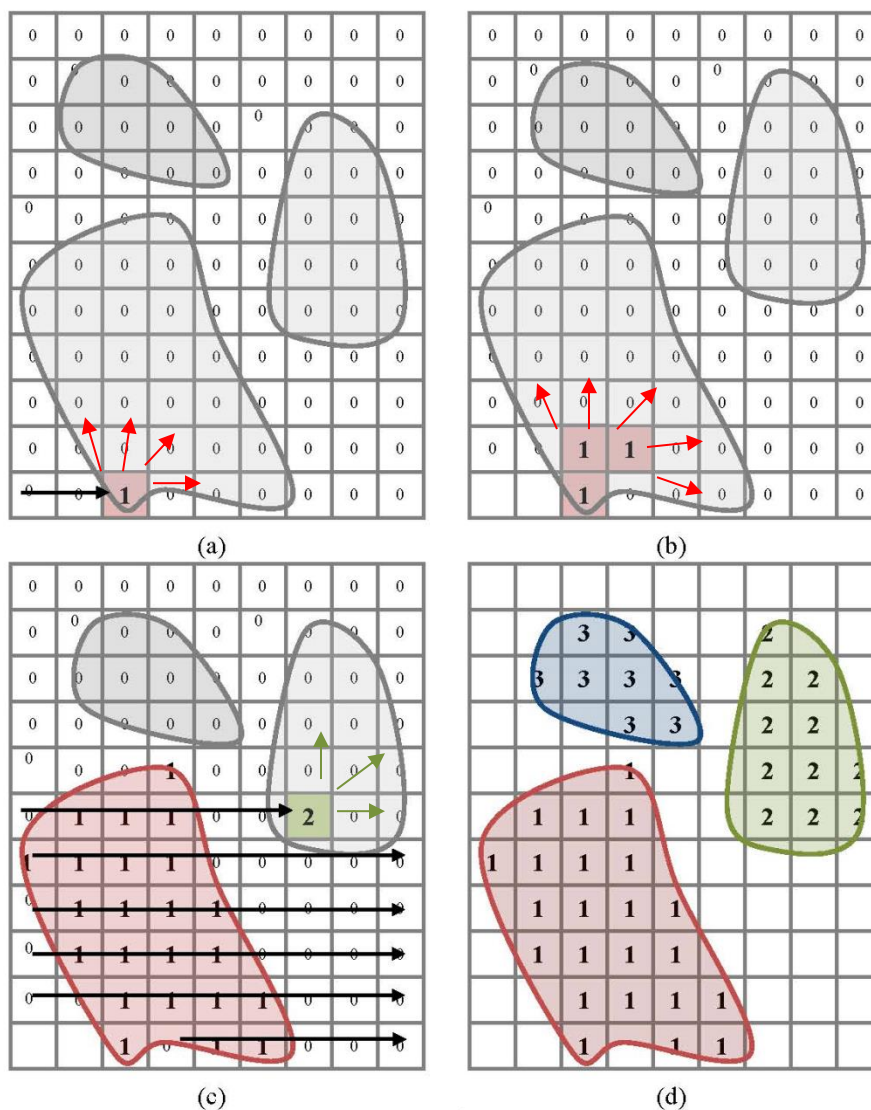


Figure 6-3 Illustration of object-labeling scheme [108]. Initially a null tag is assigned to all the voxels. The scanning process start in the natural numbering order of the voxels until the first voxel in the object 1 is found (a). All the neighbors of the tagged voxels that are in the object are tagged (b). The scanning resumes till a voxel in the second object is found (c). The all the neighbors in the object 2 are tagged. This process is continued until all the voxels in the objects are assigned are tagged (d).

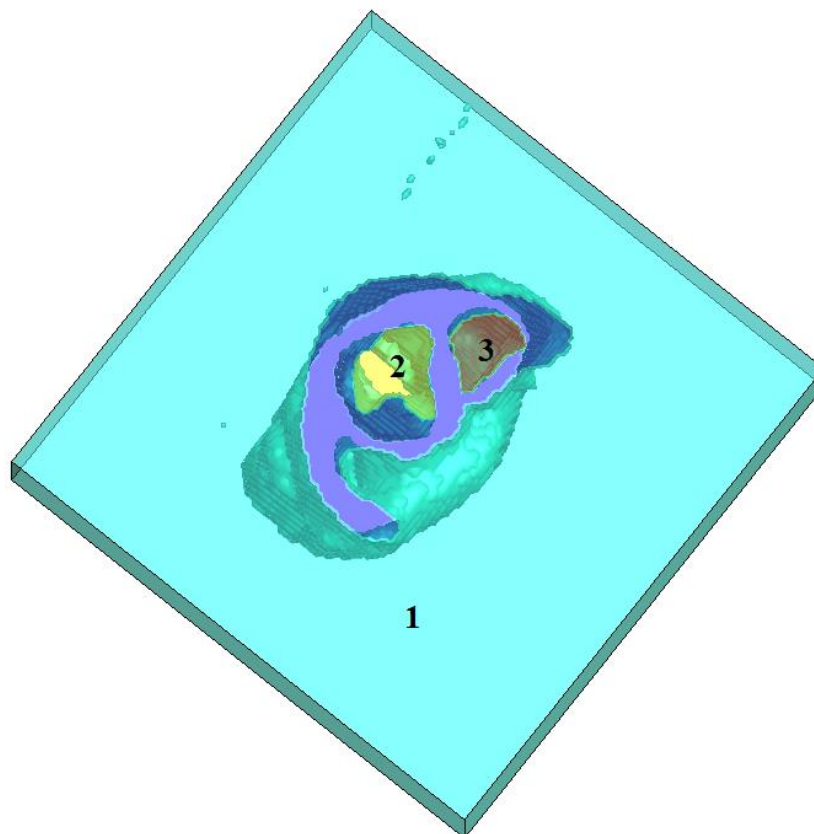


Figure 6-4 The segmented image after object numbering. Three identified are labeled with numbers 1, 2, and 3.

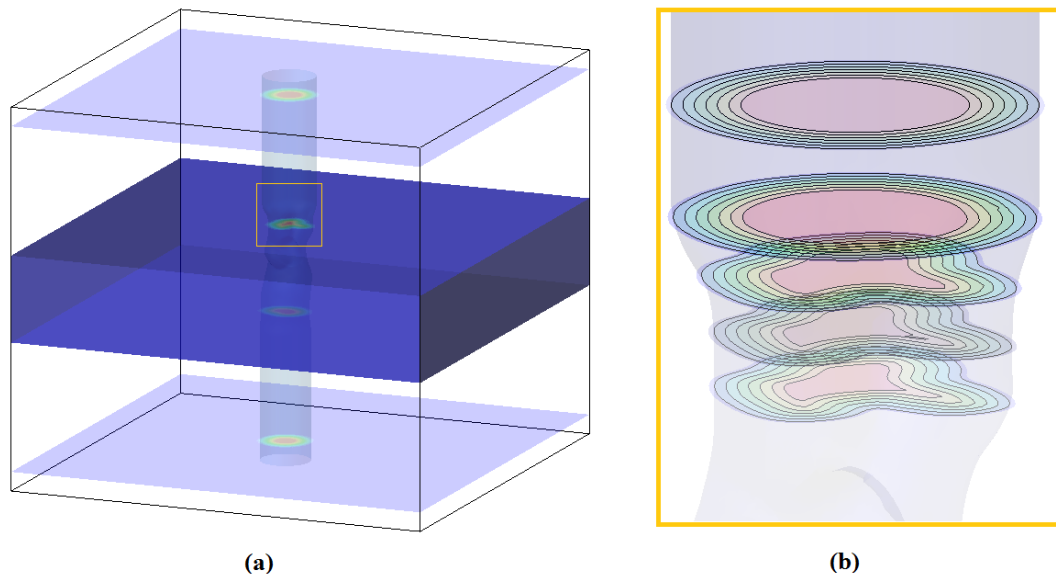


Figure 6-5 The source level set field planes are located on the top and bottom of the segmented image (solid blue box) and their target fields are positioned above the top and below the bottom slices, respectively (a). The morphing process is shown in a close-up figure on the left (b).

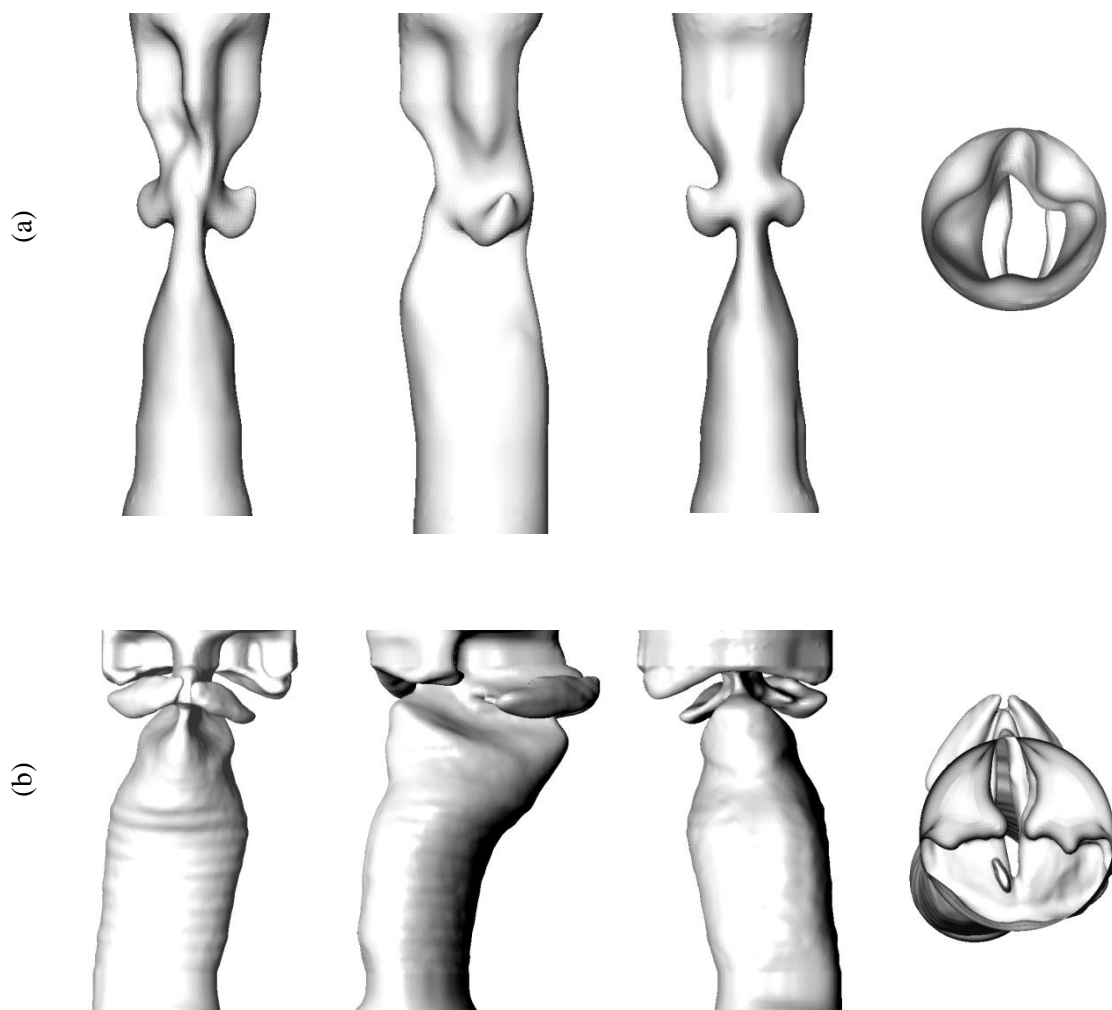


Figure 6-6 The final geometry of the (a) human larynx, (b) canine larynx.

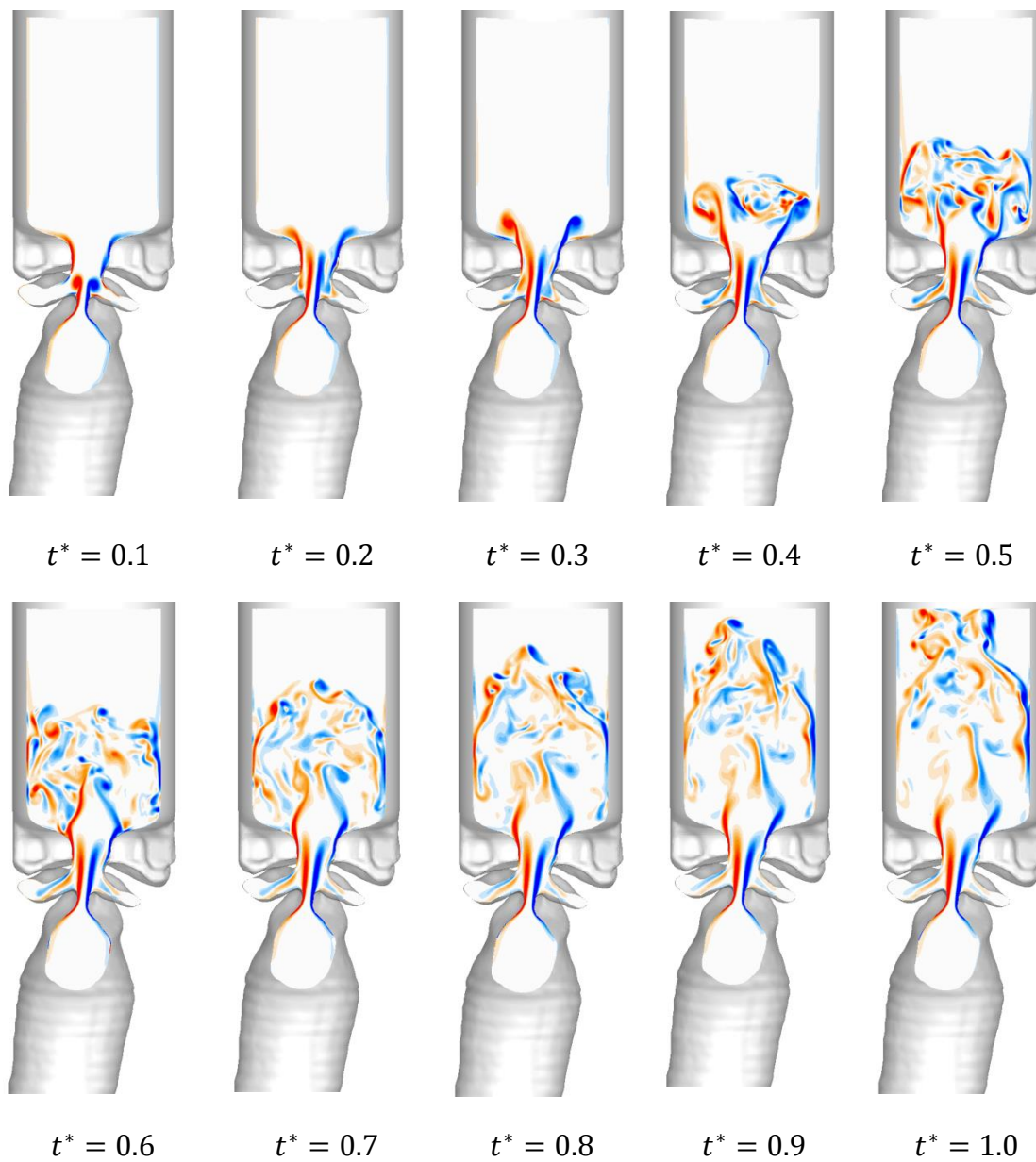


Figure 6-7 The x-vorticity contour of the glottal flow in a canine larynx geometry on a lateral slice ( $Re=500$ ).

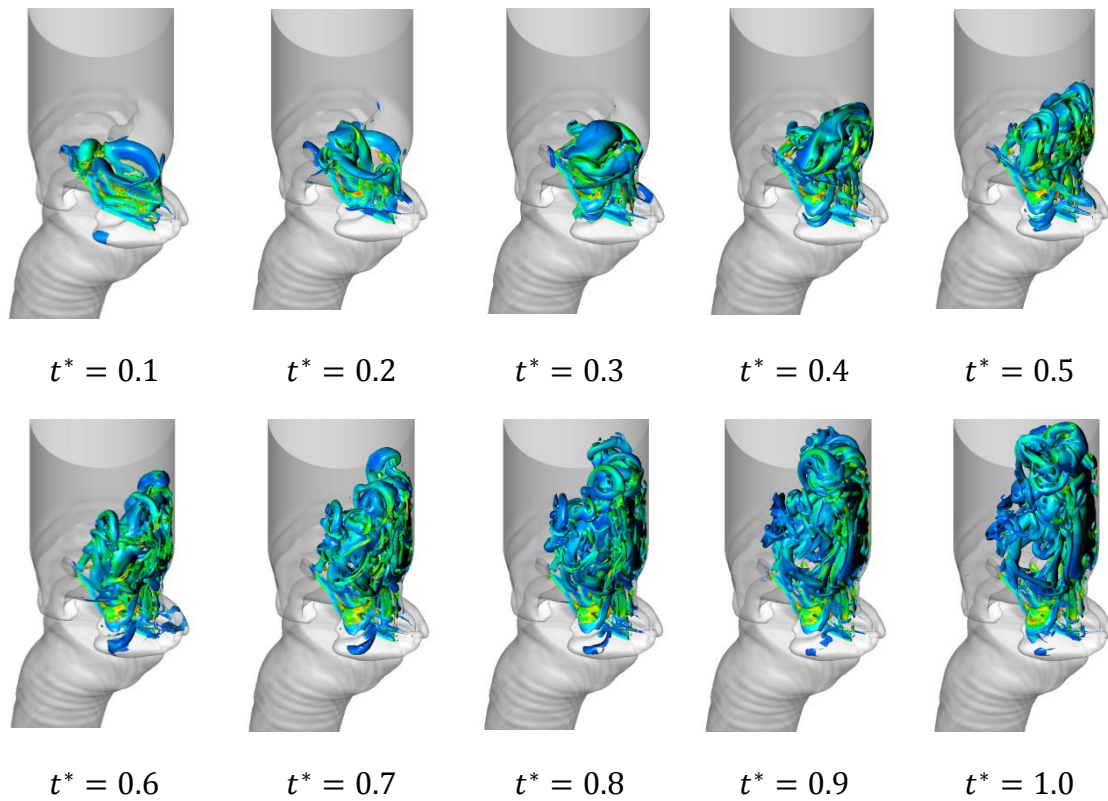


Figure 6-8 The glottal flow in a canine larynx geometry indicated with iso-surface of  $\lambda-2$  colored by vorticity magnitude ( $Re=500$ ). The contours have 20 levels between 0.0 and 150.

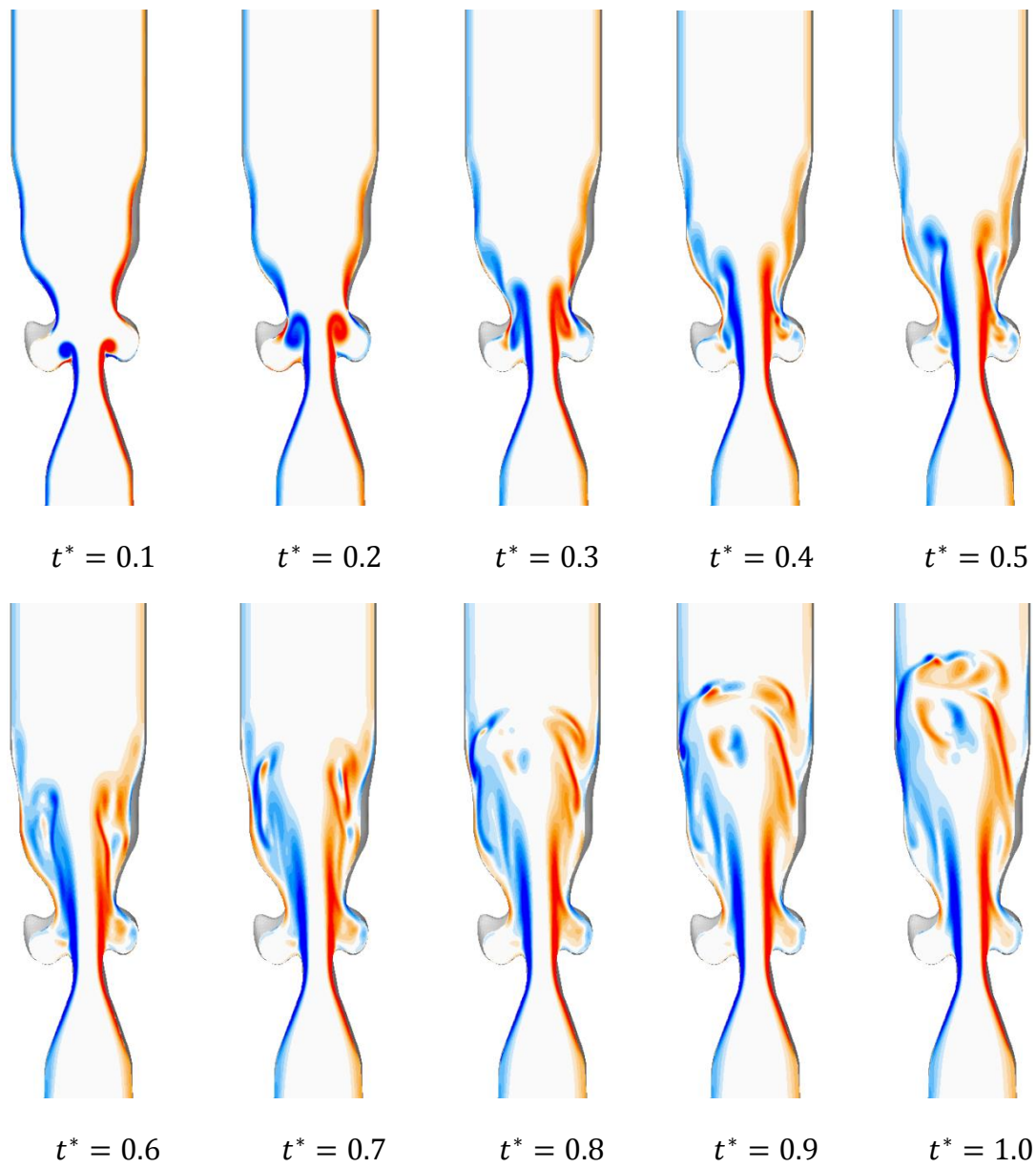


Figure 6-9 The y-vorticity contour of the glottal flow in a human larynx geometry on a lateral slice ( $Re=500$ ).

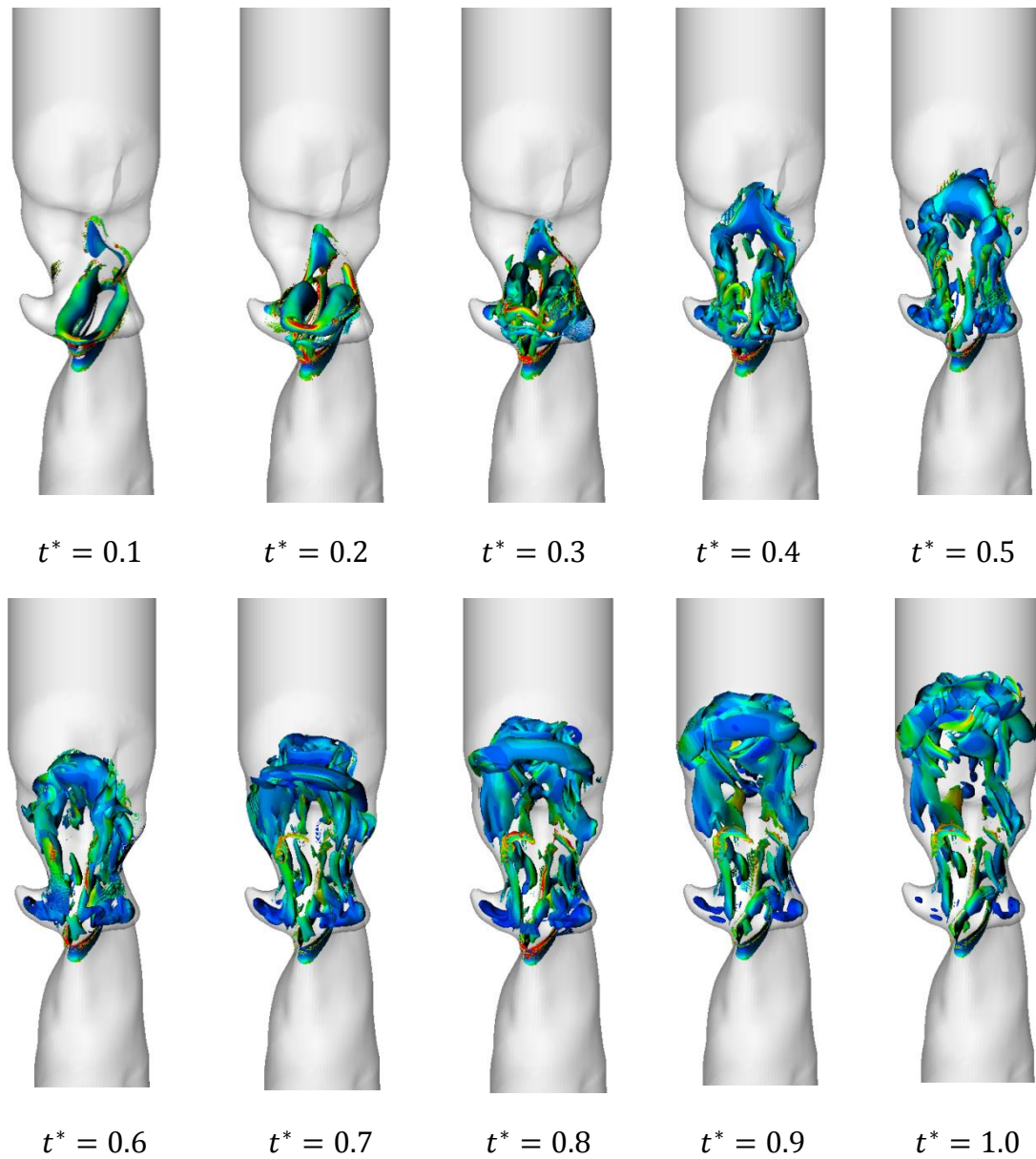


Figure 6-10 The glottal flow in a human larynx geometry indicated with iso-surface of  $\lambda_2$  colored by vorticity magnitude ( $Re=500$ ). The contours have 20 levels between 0.0 and 100.

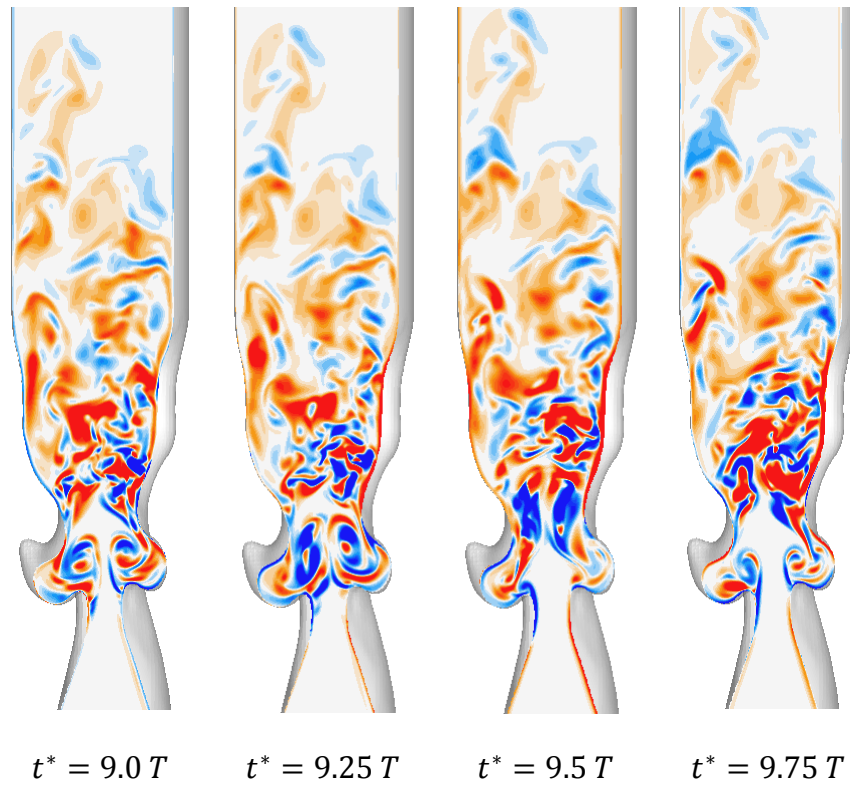


Figure 6-11 The x-vorticity contour of the glottal flow for a human larynx geometry on a lateral slice after 9 pulses of the input velocity. The pick Reynolds number is 1000 and  $T$  is the time period of each cycle of the pulse.

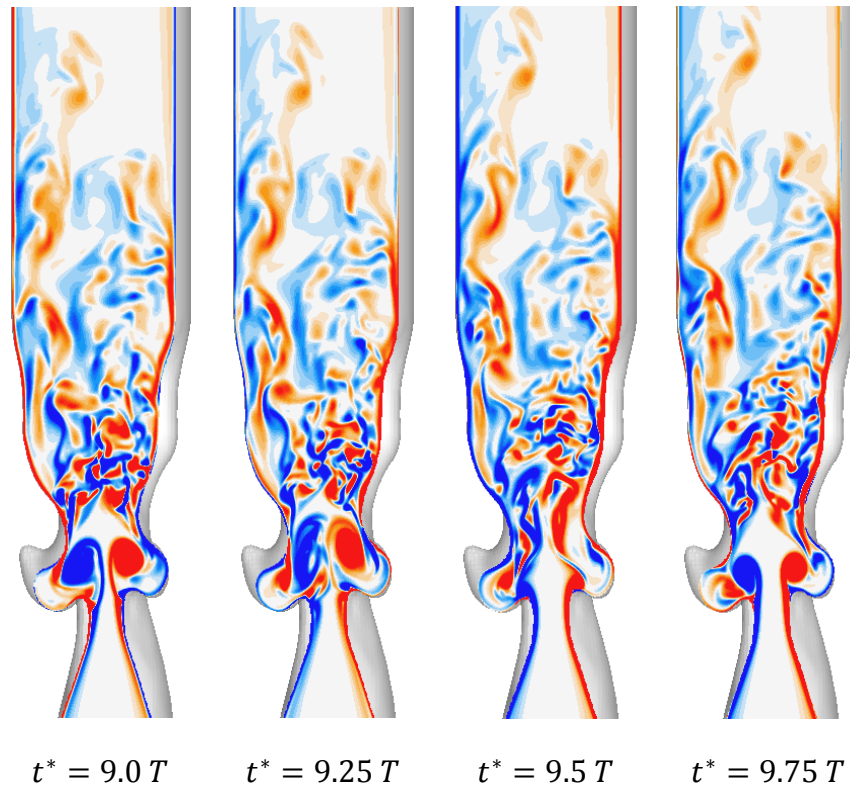


Figure 6-12 The y-vorticity contour of the glottal flow for a human larynx geometry on a lateral slice after 9 pulses of the input velocity. The pick Reynolds number is 1000 and  $T$  is the time period of each cycle of the pulse.

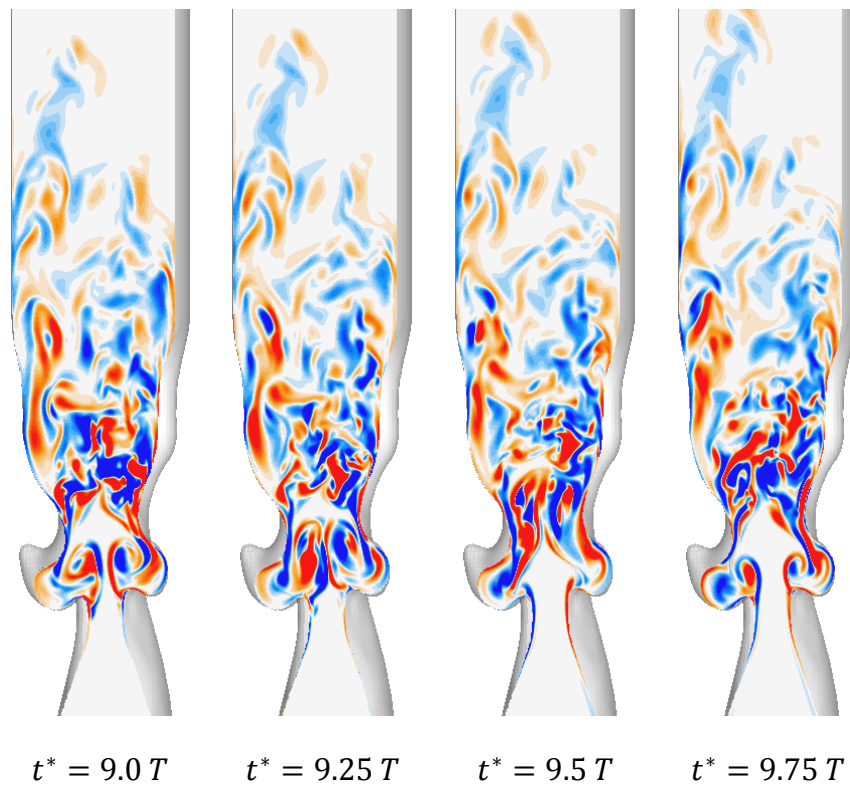


Figure 6-13 The z-vorticity contour of the glottal flow for a human larynx geometry on a lateral slice after 9 pulses of the input velocity. The pick Reynolds number is 1000 and  $T$  is the time period of each cycle of the pulse.

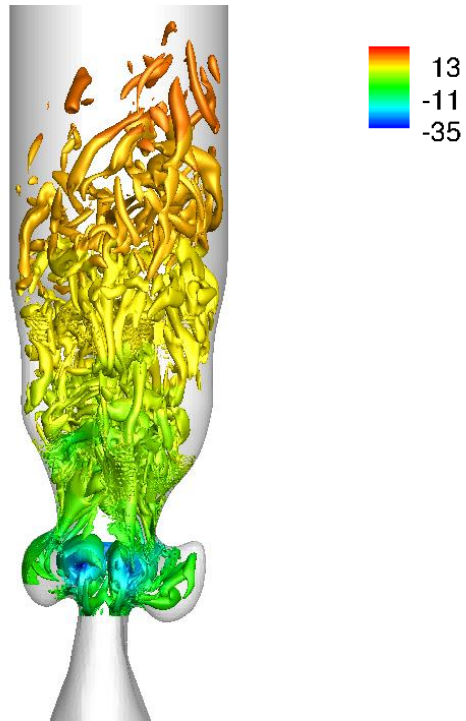


Figure 6-14 The glottal flow in a human larynx geometry indicated with iso-surface of  $\lambda_2$  colored by non-dimensional pressure ( $Re=1000$ ).

## CHAPTER 7

### CONCLUSION AND FUTURE WORK

#### 7.1 Contribution of the Current Thesis

In this dissertation, we have focused on the simulation of the glottal flow in different laryngeal geometries. A parametric study was performed on idealized models of the human larynx computationally and experimentally to investigate the effect of the FVFs on the glottal flow. Moreover, we extended our computational investigation into three dimensional simulations of the glottal flow in the physiologic Reynolds numbers and geometries of the larynx. Furthermore, a high order acoustic solver was developed for the acoustic prediction. In summary the contributions of the current work are:

1. The parametric study on the effect of the FVF geometry on the dynamics of the glottal flow show that the size of the FVF gap was the main geometrical parameter affecting the glottal flow; whereas, the width of the laryngeal ventricle and the height between the TVFs and the FVFs were of lesser importance.
2. The computational investigations confirmed the formation of the rarely reported rebound vortices in the laryngeal ventricle. It was found that these vortical structures are created as a result of the interaction between the starting vortex ring and the FVFs. In addition, it was found that the small size of the FVF gap can extremely affect the flow structures in the laryngeal flow via forming strong rebound vortices at this region.
3. A reduced-order model of the vocal folds oscillation was implemented in the fluid solver.
4. The three dimensional laryngeal geometries of the human larynx and canine larynx were extracted form CT scan images.

5. The fully-resolved flow simulation was performed in realistic geometries of the larynx with physiologic Reynolds numbers. The three dimensional simulations revealed that the glottal flow is highly three dimensional. Additionally, it provides the evidence that the rebound vortices are created in physiological geometries.
6. A novel Cartesian based moving least square finite volume acoustic solver was developed and validated against several bench mark problems.

### 7.2 Suggestions for Future Work

The mechanism of the phonation is extremely complicated and there are numerous opportunities to extent the current work. This section points to few interesting directions:

1. One of the main characteristics of the phonation is the oscillation of the vocal folds. Therefore, more promising results can be provided when the oscillation of the TVFs are taken into account. The two mass model implemented in this dissertation can be used as a starting point. More accurate investigations can be performed by coupling a finite element solver to model the nonlinear behavior of the vocal folds tissue.
2. The CT scan images used in the current study to extract the physiologic geometries of the larynges lack the upper airway tract. A better understanding about the biophysics of speech can be obtained with extracting the geometry of the vocal tract from the CT scan images and conducting computational simulations in such geometries.
3. Recent progress in the field of image to computation can be exploited to extract the oscillation of the vocal folds from high speed images. Therefore, it is possible to conduct patient-specific simulation of the human larynx in the framework of the current incompressible solver.

4. It is known that the Cartesian grid methods suffer from spurious pressure oscillations in the presence of moving boundaries. Recently, there have been several attempts to suppress these non-physical pressure oscillations. A hybridization scheme is being implemented in our incompressible flow solver to handle this problem. Upon implementation of this method, the developed acoustic solver can be coupled with the incompressible solver to model the acoustic output of the larynx.

## REFERENCES

- [1] Mittal, R., Erath, B. D., and Plesniak, M. W., 2013, "Fluid Dynamics of Human Phonation and Speech," *Annual Review of Fluid Mechanics*, 45(1), pp. 437-467.
- [2] NIDCD website, November 2013.
- [3] Aronson, A., and Bless, D., 2009, *Clinical Voice Disorders*, Book+ DVD, Thieme.
- [4] Verdolini, K., and Ramig, L. O., 2001, "Review: occupational risks for voice problems," *Logopedics Phoniatrics Vocology*, 26(1), pp. 37-46.
- [5] Van Houtte, E., Claeys, S., Wuyts, F., and Van Lierde, K., 2011, "The Impact of Voice Disorders Among Teachers: Vocal Complaints, Treatment-Seeking Behavior, Knowledge of Vocal Care, and Voice-Related Absenteeism," *Journal of Voice*, 25(5), pp. 570-575.
- [6] Stager, S., 2011, "The Role of the Supraglottic Area in Voice Production," *Otolaryngol S1*, 1, p. 2.
- [7] Simpson, C. B., and Rosen, C. A., 2008, *Operative techniques in laryngology*, Springer.
- [8] Titze, I. R., 1992, "Phonation threshold pressure: A missing link in glottal aerodynamics," *The Journal of the Acoustical Society of America*, 91(5), pp. 2926-2935.
- [9] Titze, I. R., 1988, "The physics of small-amplitude oscillation of the vocal folds," *The Journal of the Acoustical Society of America*, 83, p. 1536.
- [10] Krane, M., Barry, M., and Wei, T., 2007, "Unsteady behavior of flow in a scaled-up vocal folds model," *Journal of the Acoustical Society of America*, 122(6), pp. 3659-3670.
- [11] Neubauer, J., Zhang, Z., Miraghaie, R., and Berry, D. A., 2007, "Coherent structures of the near field flow in a self-oscillating physical model of the vocal folds," *The Journal of the Acoustical Society of America*, 121(2), pp. 1102-1118.
- [12] Erath, B. D., and Plesniak, M. W., 2010, "An investigation of asymmetric flow features in a scaled-up driven model of the human vocal folds," *Exp Fluids*, 49(1), pp. 131-146.
- [13] Triep, M., and Brücker, C., 2010, "Three-dimensional nature of the glottal jet," *The Journal of the Acoustical Society of America*, 127(3), pp. 1537-1547.
- [14] Krebs, F., Silva, F., Sciamarella, D., and Artana, G., 2012, "A three-dimensional study of the glottal jet," *Exp Fluids*, 52(5), pp. 1133-1147.
- [15] Schwarze, R., Mattheus, W., Klostermann, J., and Brücker, C., 2011, "Starting jet flows in a three-dimensional channel with larynx-shaped constriction," *Computers & Fluids*, 48(1), pp. 68-83.

- [16] Drechsel, J. S., and Thomson, S. L., 2008, "Influence of supraglottal structures on the glottal jet exiting a two-layer synthetic, self-oscillating vocal fold model," *The Journal of the Acoustical Society of America*, 123(6), pp. 4434-4445.
- [17] Erath, B. D., and Plesniak, M. W., 2006, "The occurrence of the Coanda effect in pulsatile flow through static models of the human vocal folds," *Journal of the Acoustical Society of America*, 120(2), pp. 1000-1011.
- [18] Chisari, N. E., Artana, G., and Sciamarella, D., 2011, "Vortex dipolar structures in a rigid model of the larynx at flow onset," *Exp Fluids*, 50(2), pp. 397-406.
- [19] Gharib, M., Rambod, E., and Shariff, K., 1998, "A universal time scale for vortex ring formation," *Journal of Fluid Mechanics*, 360(121-140), p. 394.
- [20] Agarwal, M., Scherer, R. C., and Hollien, H., 2003, "The False Vocal Folds: Shape and Size in Frontal View During Phonation Based on Laminagraphic Tracings," *Journal of Voice*, 17(2), pp. 97-113.
- [21] Chan, R. W., MIN, F., and Tirunagari, N., 2006, "Elasticity of the human false vocal fold," *The Annals of otology, rhinology & laryngology*, 115(5), pp. 370-381.
- [22] Haji, T., Mori, K., Omori, K., and Isshiki, N., 1992, "Mechanical properties of the vocal fold," *Acta oto-laryngologica*, 112(2), pp. 559-565.
- [23] Sakakibara, K.-I., Imagawa, H., Konishi, T., Kondo, K., Murano, E. Z., Kumada, M., and Niimi, S., 2001, "Vocal fold and false vocal fold vibrations in throat singing and synthesis of khöömei," *Proceedings of the international computer music conference*, Citeseer, pp. 135-138.
- [24] Henrich, N., Lortat-Jacob, B., Castellengo, M., Bailly, L., and Pelorson, X., 2006, "Period-doubling occurrences in singing: the 'bassu' case in traditional Sardinian 'A Tenore' singing," *International Conference on Voice Physiology and Biomechanics*, Tokyo.
- [25] Borch, D. Z., Sundberg, J., Lindestad, P.-Å., and Thalen, M., 2004, "Vocal fold vibration and voice source aperiodicity in 'dist' tones: a study of a timbral ornament in rock singing," *Logopedics Phoniatrics Vocology*, 29(4), pp. 147-153.
- [26] Lindestad, P.-Å., Blixt, V., Pahlberg-Olsson, J., and Hammarberg, B., 2004, "Ventricular fold vibration in voice production: a high-speed imaging study with kymographic, acoustic and perceptual analyses of a voice patient and a vocally healthy subject," *Logopedics Phoniatrics Vocology*, 29(4), pp. 162-170.
- [27] Nasri, S., Jasleen, J., Gerratt, B. R., Sercarz, J. A., Wenokur, R., and Berke, G. S., 1996, "Ventricular dysphonia: A case of false vocal fold mucosal traveling wave," *American Journal of Otolaryngology*, 17(6), pp. 427-431.
- [28] Maryn, Y., De Bodt, M. S., and Van Cauwenberge, P., 2003, "Ventricular dysphonia: Clinical aspects and therapeutic options," *Laryngoscope*, 113(5), pp. 859-866.

- [29] Stager, S. V., Bielamowicz, S. A., Regnell, J. R., Gupta, A., and Barkmeier, J. M., 2000, "Supraglottic activity: Evidence of vocal hyperfunction or laryngeal articulation?," *Journal of Speech Language and Hearing Research*, 43(1), pp. 229-238.
- [30] Brunelle, M., Duy Du'o'ng, N., and Khac Hung, N., 2010, "A Laryngographic and Laryngoscopic Study of Northern Vietnamese Tones," *Phonetica*, 67(3), pp. 147-169.
- [31] Kelchner, L. N., Weinrich, B., Brehm, S. B., Tabangin, M. E., and de Alarcon, A., 2010, "Characterization of Supraglottic Phonation in Children After Airway Reconstruction," *Annals of Otolaryngology and Laryngology*, 119(6), pp. 383-390.
- [32] Bielamowicz, S., Kapoor, R., Schwartz, J., and Stager, S. V., 2004, "Relationship among glottal area, static supraglottic compression, and laryngeal function studies in unilateral vocal fold paresis and paralysis," *Journal of Voice*, 18(1), pp. 138-145.
- [33] Drechsel, J. S., and Thomson, S. L., 2008, "Influence of supraglottal structures on the glottal jet exiting a two-layer synthetic, self-oscillating vocal fold model," *Journal of the Acoustical Society of America*, 123(6), pp. 4434-4445.
- [34] Kucinski, B. R., Scherer, R. C., DeWitt, K. J., and Ng, T. T. M., 2006, "Flow visualization and acoustic consequences of the air moving through a static model of the human larynx," *Journal of Biomechanical Engineering-Transactions of the Asme*, 128(3), pp. 380-390.
- [35] Li, S., Wan, M., and Wang, S., 2008, "The effects of the false vocal fold gaps on intralaryngeal pressure distributions and their effects on phonation," *Sci. China Ser. C-Life Sci.*, 51(11), pp. 1045-1051.
- [36] Zheng, X., Bielamowicz, S., Luo, H., and Mittal, R., 2009, "A Computational Study of the Effect of False Vocal Folds on Glottal Flow and Vocal Fold Vibration During Phonation," *Annals of Biomedical Engineering*, 37(3), pp. 625-642.
- [37] Kucinski, B. R., DeWitt, K. J., Ng, T. T., and Scherer, R. C., 2005, "Flow Visualization and Acoustic Consequences of the Air Moving Through a Static Model of the Human Larynx," *Journal of Biomechanical Engineering*, 128(3), pp. 380-390.
- [38] Alipour, F., Jaiswal, S., and Finnegan, E., 2007, "Aerodynamic and acoustic effects of false vocal folds and epiglottis in excised larynx models," *Annals of Otolaryngology and Laryngology*, 116(2), pp. 135-144.
- [39] Alipour, F., and Scherer, R. C., 2012, "Ventricular pressures in phonating excised larynges," *The Journal of the Acoustical Society of America*, 132(2), pp. 1017-1026.
- [40] Cattafesta, L. N., III, Song, Q., Williams, D. R., Rowley, C. W., and Alvi, F. S., 2008, "Active control of flow-induced cavity oscillations," *Progress in Aerospace Sciences*, 44(7-8), pp. 479-502.

- [41] Zhang, C., Zhao, W., Frankel, S. H., and Mongeau, L., 2002, "Computational aeroacoustics of phonation, Part II: Effects of flow parameters and ventricular folds," *Journal of the Acoustical Society of America*, 112(5), pp. 2147-2154.
- [42] McGowan, R. S., and Howe, M. S., 2010, "Influence of the ventricular folds on a voice source with specified vocal fold motion," *Journal of the Acoustical Society of America*, 127(3), pp. 1519-1527.
- [43] Faure, T. M., Adrianos, P., Lusseyran, F., and Pastur, L., 2007, "Visualizations of the flow inside an open cavity at medium range Reynolds numbers," *Exp Fluids*, 42(2), pp. 169-184.
- [44] Ozalp, C., Pinarbasi, A., and Sahin, B., 2010, "Experimental measurement of flow past cavities of different shapes," *Experimental Thermal and Fluid Science*, 34(5), pp. 505-515.
- [45] Triep, M., Brücker, C., and Schröder, W., 2005, "High-speed PIV measurements of the flow downstream of a dynamic mechanical model of the human vocal folds," *Exp Fluids*, 39(2), pp. 232-245.
- [46] de Oliveira Rosa, M., Pereira, J. C., Grellet, M., and Alwan, A., 2003, "A contribution to simulating a three-dimensional larynx model using the finite element method," *The Journal of the Acoustical Society of America*, 114, p. 2893.
- [47] Suh, J., and Frankel, S. H., 2007, "Numerical simulation of turbulence transition and sound radiation for flow through a rigid glottal model," *The Journal of the Acoustical Society of America*, 121, p. 3728.
- [48] Zheng, X., Beilamowicz, S., Xue, Q., and Mittal, R., 2010, "A Coupled Sharp-Interface Immersed Boundary-Finite-Element Method for Flow-Structure Interaction With Application to Human Phonation," *Journal of Biomechanical Engineering*, 132(11), pp. 111003-111003.
- [49] Zheng, X., Mittal, R., Xue, Q., and Bielamowicz, S., 2011, "Direct-numerical simulation of the glottal jet and vocal-fold dynamics in a three-dimensional laryngeal model," *The Journal of the Acoustical Society of America*, 130, p. 404.
- [50] Mattheus, W., and Brücker, C., 2011, "Asymmetric glottal jet deflection: Differences of two-and three-dimensional models," *The Journal of the Acoustical Society of America*, 130(6), pp. EL373-EL379.
- [51] Švancara, P., Horáček, J., and Švec, J., 2012, "Numerical Simulation of the Self-Oscillations of the Vocal Folds and of the Resulting Acoustic Phenomena in the Vocal Tract," *Advances in Mechanisms Design*, Springer, pp. 357-363.
- [52] Šidlof, P., Horáček, J., and Řídký, V., 2012, "Parallel CFD simulation of flow in a 3D model of vibrating human vocal folds," *Computers & Fluids*.
- [53] Nomura, H., and Funada, T., 2007, "Effects of the false vocal folds on sound generation by an unsteady glottal jet through rigid wall model of the larynx," *Acoustical science and technology*, 28(6), pp. 403-412.

- [54] Sethian, J. A., 1999, *Level set methods and fast marching methods: evolving interfaces in computational geometry, fluid mechanics, computer vision, and materials science*, Cambridge university press.
- [55] Yue, W., Lin, C. L., and Patel, V. C., 2003, "Numerical simulation of unsteady multidimensional free surface motions by level set method," *International Journal for Numerical Methods in Fluids*, 42(8), pp. 853-884.
- [56] Osher, S., and Fedkiw, R. P., 2001, "Level set methods: an overview and some recent results," *Journal of Computational physics*, 169(2), pp. 463-502.
- [57] Sambasivan, S. K., and UdayKumar, H., 2010, "Sharp interface simulations with Local Mesh Refinement for multi-material dynamics in strongly shocked flows," *Computers & Fluids*, 39(9), pp. 1456-1479.
- [58] Mousel, J. A., 2012, "A massively parallel adaptive sharp interface solver with application to mechanical heart valve simulations."
- [59] Kapahi, A., Mousel, J., Sambasivan, S., and Udaykumar, H. S., 2013, "Parallel, sharp interface Eulerian approach to high-speed multi-material flows," *Computers & Fluids*, 83(0), pp. 144-156.
- [60] Flanagan, J., and Landgraf, L., 1968, "Self-oscillating source for vocal-tract synthesizers," *Audio and Electroacoustics, IEEE Transactions on*, 16(1), pp. 57-64.
- [61] Howe, M., and McGowan, R., 2010, "On the single-mass model of the vocal folds," *Fluid dynamics research*, 42(1), p. 015001.
- [62] Flanagan, J. L., and Ishizaka, K., 1978, "Computer model to characterize the air volume displaced by the vibrating vocal cords," *The Journal of the Acoustical Society of America*, 63(5), pp. 1559-1565.
- [63] Erath, B. D., Zañartu, M., Stewart, K. C., Plesniak, M. W., Sommer, D. E., and Peterson, S. D., 2013, "A review of lumped-element models of voiced speech," *Speech Communication*, 55(5), pp. 667-690.
- [64] Cveticanin, L., 2012, "Review on Mathematical and Mechanical Models of the Vocal Cord," *Journal of Applied Mathematics*, 2012.
- [65] Steinecke, I., and Herzel, H., 1995, "Bifurcations in an asymmetric vocal-fold model," *The Journal of the Acoustical Society of America*, 97(3), pp. 1874-1884.
- [66] Jaiman, R., Geubelle, P., Loth, E., and Jiao, X., 2011, "Combined interface boundary condition method for unsteady fluid–structure interaction," *Computer Methods in Applied Mechanics and Engineering*, 200(1), pp. 27-39.
- [67] Orlandi, P., 1990, "Vortex dipole rebound from a wall," *Physics of Fluids A: Fluid Dynamics*, 2, p. 1429.
- [68] Chu, C. C., Wang, C. T., and Hsieh, C. S., 1993, "An experimental investigation of vortex motions near surfaces," *Physics of Fluids A: Fluid Dynamics*, 5, p. 662.

- [69] Seo, J.-H., and Moon, Y. J., 2005, "Perturbed Compressible Equations for Aeroacoustic Noise Prediction at Low Mach Numbers," *AIAA Journal*, 43(8), pp. 1716-1724.
- [70] Seo, J. H., and Moon, Y. J., 2006, "Linearized perturbed compressible equations for low Mach number aeroacoustics," *Journal of Computational Physics*, 218(2), pp. 702-719.
- [71] Colonius, T., and Lele, S. K., 2004, "Computational aeroacoustics: progress on nonlinear problems of sound generation," *Progress in Aerospace Sciences*, 40(6), pp. 345-416.
- [72] Lele, S. K., 1992, "Compact finite difference schemes with spectral-like resolution," *Journal of Computational Physics*, 103(1), pp. 16-42.
- [73] DONG, Z., TAM, C. K. W., and WEBB, J. C., 1993, "A STUDY OF THE SHORT WAVE COMPONENTS IN COMPUTATIONAL ACOUSTICS," *Journal of Computational Acoustics*, 01(01), pp. 1-30.
- [74] Cueto-Felgueroso, L., Colominas, I., Nogueira, X., Navarrina, F., and Casteleiro, M., 2007, "Finite volume solvers and Moving Least-Squares approximations for the compressible Navier–Stokes equations on unstructured grids," *Computer Methods in Applied Mechanics and Engineering*, 196(45–48), pp. 4712-4736.
- [75] Ollivier-Gooch, C., and Van Alena, M., 2002, "A High-Order-Accurate Unstructured Mesh Finite-Volume Scheme for the Advection–Diffusion Equation," *Journal of Computational Physics*, 181(2), pp. 729-752.
- [76] Nogueira, X., Khelladi, S., Colominas, I., Cueto-Felgueroso, L., París, J., and Gómez, H., 2011, "High-Resolution Finite Volume Methods on Unstructured Grids for Turbulence and Aeroacoustics," *Arch Computat Methods Eng*, 18(3), pp. 315-340.
- [77] Cueto-Felgueroso, L., and Colominas, I., 2008, "High-order Finite Volume Methods and Multiresolution Reproducing Kernels," *Arch Computat Methods Eng*, 15(2), pp. 185-228.
- [78] Seo, J. H., and Mittal, R., 2011, "A high-order immersed boundary method for acoustic wave scattering and low-Mach number flow-induced sound in complex geometries," *Journal of Computational Physics*, 230(4), pp. 1000-1019.
- [79] Munz, C.-D., Dumbser, M., and Roller, S., 2007, "Linearized acoustic perturbation equations for low Mach number flow with variable density and temperature," *Journal of Computational Physics*, 224(1), pp. 352-364.
- [80] Wang, M., Freund, J. B., and Lele, S. K., 2006, "Computational prediction of flow-generated sound," *Annu. Rev. Fluid Mech.*, 38, pp. 483-512.
- [81] Hardin, J. C., and Pope, D. S., 1994, "An acoustic/viscous splitting technique for computational aeroacoustics," *Theoret. Comput. Fluid Dynamics*, 6(5-6), pp. 323-340.

- [82] Shen, W. Z., N-oacute, J., S-oacute, r., and rensen, 1999, "Comment on the Aeroacoustic Formulation of Hardin and Pope," *AIAA Journal*, 37(1), pp. 141-143.
- [83] Shen, W. Z., and Sørensen, J. N., 1999, "Aeroacoustic Modelling of Low-Speed Flows," *Theoret. Comput. Fluid Dynamics*, 13(4), pp. 271-289.
- [84] Slimon, S. A., Soteriou, M. C., and Davis, D. W., 2000, "Development of Computational Aeroacoustics Equations for Subsonic Flows Using a Mach Number Expansion Approach," *Journal of Computational Physics*, 159(2), pp. 377-406.
- [85] Nogueira, X., Colominas, I., Cueto-Felgueroso, L., Khelladi, S., Navarrina, F., and Casteleiro, M., 2010, "Resolution of computational aeroacoustics problems on unstructured grids with a higher-order finite volume scheme," *Journal of Computational and Applied Mathematics*, 234(7), pp. 2089-2097.
- [86] Nogueira, X., Colominas, I., Cueto-Felgueroso, L., and Khelladi, S., 2010, "On the simulation of wave propagation with a higher-order finite volume scheme based on Reproducing Kernel Methods," *Computer Methods in Applied Mechanics and Engineering*, 199(23–24), pp. 1471-1490.
- [87] Thompson, K. W., 1987, "Time dependent boundary conditions for hyperbolic systems," *Journal of Computational Physics*, 68(1), pp. 1-24.
- [88] DONG, Z., and TAM, C. K. W., 1996, "RADIATION AND OUTFLOW BOUNDARY CONDITIONS FOR DIRECT COMPUTATION OF ACOUSTIC AND FLOW DISTURBANCES IN A NONUNIFORM MEAN FLOW," *Journal of Computational Acoustics*, 04(02), pp. 175-201.
- [89] Edgar, N. B., and Visbal, M. R., 2003, "A general buffer zone-type non-reflecting boundary condition for computational aeroacoustics," *AIAA paper*, 3300, p. 2003.
- [90] Colonius, T. I. M., Lele, S. K., and Moin, P., 1993, "Boundary conditions for direct computation of aerodynamic sound generation," *AIAA Journal*, 31(9), pp. 1574-1582.
- [91] Israeli, M., and Orszag, S. A., 1981, "Approximation of radiation boundary conditions," *Journal of Computational Physics*, 41(1), pp. 115-135.
- [92] Mani, A., 2012, "Analysis and optimization of numerical sponge layers as a nonreflective boundary treatment," *Journal of Computational Physics*, 231(2), pp. 704-716.
- [93] Hu, F. Q., 2008, "Development of PML absorbing boundary conditions for computational aeroacoustics: A progress review," *Computers & Fluids*, 37(4), pp. 336-348.
- [94] Gaitonde, D. V., and Visbal, M. R., 1998, "High-order schemes for Navier-Stokes equations: algorithm and implementation into FDL3DI," *DTIC Document*.
- [95] Sun, X., Jiang, Y., Liang, A., and Jing, X., 2012, "An immersed boundary computational model for acoustic scattering problems with complex geometries," *The Journal of the Acoustical Society of America*, 132(5), pp. 3190-3199.

- [96] Hardin, J., Ristorcelli, J., and Tam, C., 1995, "ICASE/LaRC workshop on benchmark problems in computational aeroacoustics," NASA conference publication.
- [97] Baily, C., and Juvé, D., 2000, "Numerical Solution of Acoustic Propagation Problems Using Linearized Euler Equations," *AIAA Journal*, 38(1), pp. 22-29.
- [98] Hu, F. Q., 2002, "On constructing stable perfectly matched layers as an absorbing boundary condition for Euler equations," *AIAA paper*, 227.
- [99] TAM, C. K., and Hardin, J., 1997, "Second Computational Aeroacoustics(CAA) Workshop on Benchmark Problems."
- [100] Liu, Q., and Vasilyev, O. V., 2007, "A Brinkman penalization method for compressible flows in complex geometries," *Journal of Computational Physics*, 227(2), pp. 946-966.
- [101] Zheng, X., Mittal, R., Xue, Q., and Bielamowicz, S., 2011, "Direct-numerical simulation of the glottal jet and vocal-fold dynamics in a three-dimensional laryngeal model," *The Journal of the Acoustical Society of America*, 130(1), pp. 404-415.
- [102] Xue, Q., Mittal, R., Zheng, X., and Bielamowicz, S., 2012, "Computational modeling of phonatory dynamics in a tubular three-dimensional model of the human larynx," *The Journal of the Acoustical Society of America*, 132(3), pp. 1602-1613.
- [103] Zhang, C., Zhao, W., Frankel, S. H., and Mongeau, L., 2002, "Computational aeroacoustics of phonation, Part II: Effects of flow parameters and ventricular folds," *The Journal of the Acoustical Society of America*, 112(5), pp. 2147-2154.
- [104] Link, G., Kaltenbacher, M., Breuer, M., and Döllinger, M., 2009, "A 2D finite-element scheme for fluid–solid–acoustic interactions and its application to human phonation," *Computer Methods in Applied Mechanics and Engineering*, 198(41–44), pp. 3321-3334.
- [105] Maryn, Y., De Bodt, M. S., and Van Cauwenberge, P., 2003, "Ventricular dysphonia: clinical aspects and therapeutic options," *The Laryngoscope*, 113(5), pp. 859-866.
- [106] Scherer, R. C., Shinwari, D., De Witt, K. J., Zhang, C., Kucinski, B. R., and Afjeh, A. A., 2001, "Intraglottal pressure profiles for a symmetric and oblique glottis with a divergence angle of 10 degrees," *The Journal of the Acoustical Society of America*, 109(4), pp. 1616-1630.
- [107] Alipour, F., and Scherer, R. C., 2001, "Effects of oscillation of a mechanical hemilarynx model on mean transglottal pressures and flows," *The Journal of the Acoustical Society of America*, 110(3), pp. 1562-1569.
- [108] Herrmann, M., 2010, "A parallel Eulerian interface tracking/Lagrangian point particle multi-scale coupling procedure," *Journal of Computational Physics*, 229(3), pp. 745-759.